Surface Properties of Hard Fluorinated Amorphous Carbon Films Deposited by Pulsed-DC Discharges

Miguel Rubio-Roy

Thesis: Surface Properties of Hard Fluorinated Amorphous Carbon Films Deposited by Pulsed-DC Discharges

Author: Miguel Rubio Roy

Submission date: January 18th, 2010

Defense date: February 26th, 2010

Defense panel:

Fausto Sanz Carrasco	Examiner, president
Carles Corbella Roca	Examiner
Agustín Rodríguez González-Elipe	Examiner
Joaquim Puigdollers González	Substitute examiner
Jordi Garcia Céspedes	Substitute examiner
Juan Pedro Espinos Manzorro	Substitute examiner
Enric Bertran Serra	PhD supervisor
Ricardo Molina Mansilla	PhD supervisor

doctoral thesis

SURFACE PROPERTIES OF HARD FLUORINATED AMORPHOUS CARBON FILMS DEPOSITED BY PULSED-DC DISCHARGES

Miguel Rubio Roy

Enric Bertran Serra
Ricardo Molina Mansilla
Thesis directors

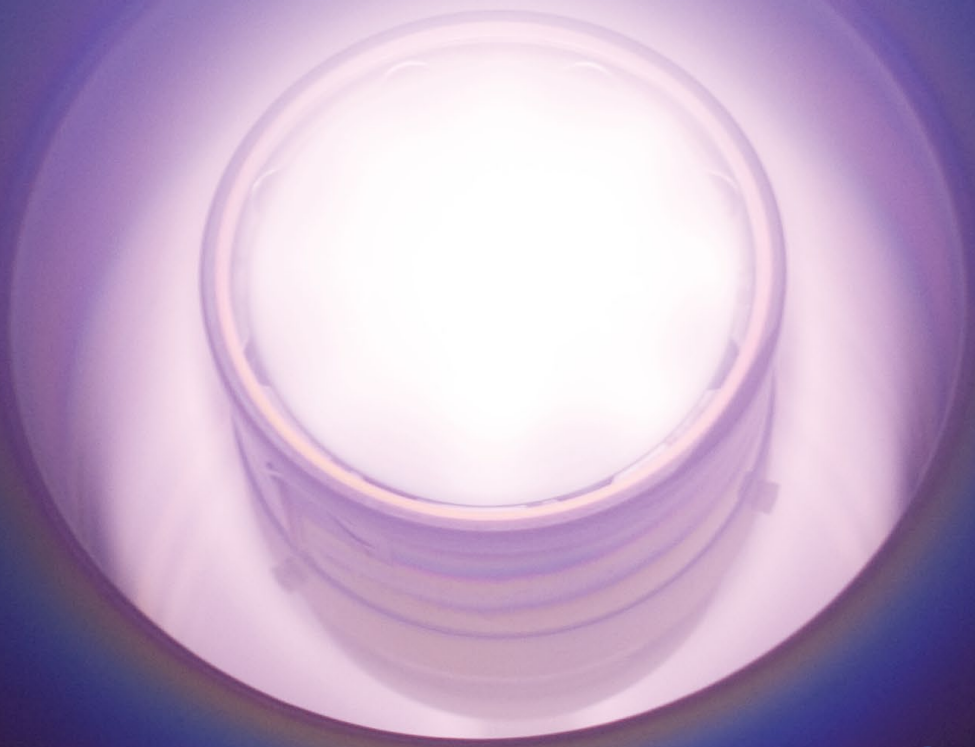

FEMAN Research Group
Departament de Física Aplicada i Òptica

UNIVERSITAT DE BARCELONA

Departament de Física Aplicada i Òptica
Universitat de Barcelona

Surface Properties of Hard Fluorinated Amorphous Carbon Films Deposited by Pulsed-DC Discharges

Miguel Rubio Roy

Directores: Enric Bertran Serra (UB) i Ricardo Molina Mansilla (CSIC)
Programa de doctorado: Técnicas Instrumentales de la Física y la Ciencia de Materiales, bienio 2004/2006

Memoria presentada para optar al grado de Doctor
Barcelona, 18 de enero de 2010

Acknowledgments

Esta tesis nunca hubiese llegado a empezar sin mi vocación por la ciencia, y ésta, sin duda, se la debo a mis padres, que me educaron para ver el mundo desde una perspectiva racional y científica. Cuestionarlo todo, preguntarme todo. Les agradezco que me hicieran ver así el mundo y también que, junto con mi hermana, me apoyaran cuando elegí dedicarme a la sufrida carrera de investigador.

Como también me ha apoyado y animado mi director de tesis, Enric. De él, y con él he aprendido la mayor parte de lo que sé sobre investigación: la actividad y el mundo científico, con una perspectiva amplia e integradora de sus diferentes aspectos. Le agradezco que me haya aguantado tanto tiempo, con lo tozudo que soy y que siempre me haya animado cuando yo veía las cosas complicadas. Gracias también a Ricardo, que me ha ayudado a darle a esta tesis el aire que hoy tiene, y a analizar correctamente XPS y energía superficial. Y a la doctora Pilar Erra Serrabasa, que siempre se ha preocupado por mi y me ayudó a conseguir la beca dentro de la Unidad Asociada CSIC-UB.

Gracias a todo el grupo FEMAN. Una casa grande, en la que todos hacemos cosas diferentes, pero sabiendo hacerlas casar y sobretodo con mucha camaradería. Somos y hemos sido muchos. Los titulares: Enric, José Luís, Mari Carmen, Esther y Adolf. Los postdocs: Sabine y en especial Carles, de quien no puedo cuantificar la ayuda que me ha prestado y además siempre con ese buen humor y optimismo que le caracteriza. Y por último, y por ello los más importantes, los becarios: Jordi, Oriol, Noemí, Maria José, Carles (antes de ser doctor) y muchos más. A Jordi quiero darle especiales gracias, por su apoyo sincero, por su amistad y por su contagiosa creatividad e imaginación.

Pero qué sería de FEMAN sin el departamento de Física Aplicada i Óptica. Os doy las gracias a todos por hacer la vida tan agradable en este departamento, y en especial a Joan por transmitir su intuitiva visión de la física, a Pere por sus consejos y buen rollo, y sobretodo, otra vez los becarios. Oriol, Carol, Paolo (que es postdoc, pero nos quiere más a nosotros), Paz, Eric, Martí, Jofre, Ruben y todos los demás. Gracias.

Y al grupillo de Ronda de la Via y allegados. Unos cachondos y cachondas mentales que me han hecho sentir siempre como en casa. Gracias Jordi, Oriol, Carol, Alberto, Álex, Ángela, Bárbara y Yucef.

A las y los secretarios, que después de mi fase de Paco Palomo, en algún momento llegaron a decir que se necesitaría una persona dedicada a atender todo el trabajo que les daba, y aun así me seguían sonriendo cuando nos veíamos. Gracias Jordi, Sandra, Dolors y Maite.

Y le llega el turno a los Serveis Cientifico Tècnics. Sin ellos no hubiese hecho nada. Creo que me atrevo a decir que es de lo mejor, sino lo mejor, de la UB y no solo por las decenas de técnicas de caracterización que tienen, sino también por la profesionalidad y la magnífica disposición a ayudar que tiene su personal. Gracias a todo el equipo de microsopía electrónica de barrido, que me aguantó durante meses cada día allí metido aprendiendo a usar el accesorio de EBL, y en especial a Ramón

Fontarnau, que aunque ya no esté entre nosotros, siempre recordaré por su afabilidad y su gran profesionalidad. Él me enseñó todos los trucos para conseguir la máxima estabilidad de un haz de electrones.

Gracias a Manel, Sunyol y los dos Javis. Os he dado mucha faena y os he apretado todo lo que he podido para que me la hicieseis para ayer. Cuando me veíais entrar ya os reíais. Siempre me habéis hecho estar a gusto en el taller, tanto el del sótano como Javi en el de planta 4.

Gracias a Joaquim Puigdollers, que es una excelente persona y que además de interesarse siempre por como me iba, me ha dado, regalado o crecido todas las capas de óxido térmico de silicio que he necesitado.

Gracias a toda la gente del ICMAB: Pep Fontcoberta, Florencio, Xavi, Ingrid, David. Me ha encantado trabajar y aprender con vosotros.

Gracias al doctor Jose Luís Prieto Martín, que me prestó una gran ayuda con el uso del EBL CRESTEC.

Gracias también a Darío Castello, que quizás nunca lea esto, pero que, sin quererlo, fue el culpable de que finalmente me animase a estudiar física.

Gracias a todos mis coleguitas: a Miki, Núria, Marc, Hector, Lorena, David, Moha, Lara, Borja y Jorge y muchos más, que en los momentos duros de estos últimos años habéis estado a la altura.

Y por último, gracias a Núria, que me ha aguantado de forma estoica estos últimos meses de escritura en los que he estado insoportable y me ha apoyado y escuchado y ayudado y querido.

Y en fin, que si me dejo a alguien, por favor no os enfadéis, porque todos los que me conocéis sabéis que tengo memoria de pez.

Preface

This thesis started in May 2005 after a period in which the author acquired mastery on the electron beam lithography technique and secondary electron microscopes operation.

The research carried out for the preparation of this thesis, started in the framework of the project "Preparation of multifunctional amorphous carbon thin films through bipolar pulsed plasma techniques" (MAT2003-02997), financed by education and science department of the Spanish government (MEC). This project finished in 2006, and the thesis continued within the project "Amorphous carbon molds for micro and nanoimprint of polymeric surfaces" (DPI2007-61349), started in January 2007 and financed by the science and innovation department (MICINN). All the research carried out by the author for these projects was done within the associate unit "FEMAN" between the Instituto de Química Avanzada de Cataluña (IQAC) of the Centro Superior de Investigaciones Científicas (CSIC) and the research group "FEMAN" of the Universitat de Barcelona (UB). The graduate grant that financed this thesis (UAC-2005-0021) was in special accordance with the DPI2007-61349 project and was financed both by CSIC and MEC.

After finishing most of the experimental part of this thesis, the author worked as researcher in the Georgia Institute of Technology, USA, from February 2009 to October the same year, on another form of carbon: "graphene". The author wrote an important part of this thesis during that time.

The scope of the DPI2007-61349 "SURFaC" project is the study of the properties conferred by amorphous carbon (a-C) coatings on nanoimprint molds with nanometric features and macroscopic dimensions, as well as the optimization of the mechanical and surface properties of the coating. Specifically, the use of alloying elements such as N, B, Si, F or metals is suggested as a way to reduce the sticking of polymers to molds during the imprint process, which introduced serious problems during the demolding step.

The work leading to this thesis, in the framework of the project SURFaC, has included a number of different tasks:

- The design and construction of a very high vacuum reactor suitable for both deposition and etching processes.

- The incorporation of fluorine to amorphous carbon films, and their characterization by different chemical, mechanical and tribological techniques, as well as characterization of the plasma used in the processes.

- The set up and optimization of a deep etching and an ion beam etching techniques adequate for mold production.

- The use of different lithographic techniques orientated toward large-area production of nanoscale features.

- The exploration of mold coating with a-C for durability and anti-sticking purposes in nanoimprint processes.

The thesis is divided in three main parts: State of the art, Experimental device and Results. The first part will justify the interest of the research carried out in this project and will present a summary of the present knowledge on its different aspects. The second part will describe the experimental setups used throughout the thesis and will briefly explain the fundamentals of each technique. Finally, in the third part, a review of the obtained results will be exposed.

As complementary information, the manuscript includes an Appendix with a method for solving overdetermined linear equations used in the surface energy calculations and a complete list of the produced films and samples.

Part of the experimental work in this thesis, specifically the large area lithography, was developed in the Central de Tecnología — Instituto de Sistemas Optoelectrónicos y Microtecnología of the Universidad Politécnica de Madrid. Also, in August 2007, a 1 month stay was done in the Fraunhofer Institute for Surface Engineering and Thin Films in Braunschweig, Germany.

In addition to the work specifically related to this thesis, the author has also participated in the project "Nanodevices for Spin Manipulation" (NAN2004-09094-C03), coordinated by the Instituto de Ciencia de Materiales de Barcelona (ICMAB) of the CSIC and financed by the education and science department of the Spanish government. The work within this project spanned from March 2006 to February 2009, representing an important part of the author's scientific activities. The task consisted on the growth and characterization of Permalloy ($Ni_{80+x}Fe_{20-x}$) films with the goal of achieving the minimum possible coercive field and zero exchange bias, for its use as an electrode in spin manipulation devices. To achieve this, a new magnetron sputtering head was designed and build by the author, with low construction cost and enabled for ultra high vacuum operation. The resulting design is being considered for patentability.

The scientific results produced during the duration of this thesis have been published by means of a number of publications in international specialized journals and oral contributions in conferences and meetings. A list of the published papers is shown in page 117.

Summary in Spanish

Desde que en 1947 científicos de Texas Instruments desarrollaran el primer transistor, y en 1958 el primer circuito integrado, la carrera por la miniaturización de estos dispositivos no se ha parado.

Las cada vez más importantes limitaciones de la largamente usada litografía de luz ultravioleta (UV) y la dificultad de extender su uso a los cada vez más estrictos requisitos de resolución, llevaron desde hace ya un par de décadas, a plantearse la necesidad de buscar técnicas litográficas llamadas de "Nueva Generación" (NGL) que superasen dichas limitaciones. Son diversas las técnicas se han ido proponiendo durante estos años, pero la mejora de la litografía UV las ha ido relegando siempre a un segundo plano, fuera del ámbito más industrial.

Más recientemente, la litografía por nanoestampación (NIL), inventada en la década de los 90, ha tomado fuerza como la nueva NGL por su extrema sencillez, en comparación a la litografía UV y por su demostrada elevada resolución.

La NIL térmica (T-NIL) consiste en la deformación de un termoplástico bajo presión ($\sim 6\,\mathrm{MPa}$) y temperatura por un molde con estructuras nanométricas, mientras que la NIL por UV (UV-NIL) consiste en la polimerización de un monómero a temperatura ambiente bajo una cierta presión ($\sim 0{,}5\,\mathrm{MPa}$) por un molde transparente al UV.

Uno de los principales problemas que afronta esta técnica es la separación de molde y polímero, una vez finalizado el proceso. Este problema es especialmente importante para la UV-NIL, dado que los tratamientos de moldes que funcionan para el T-NIL, fallan con luz UV por interacción con esta.

En esta situación, se han propuesto los recubrimientos delgados de carbono amorfo como alternativa a los tratamientos existentes por su baja reactividad química y posibilidad de incorporación de otros elementos químicos a fin de reducir su ya baja energía superficial.

El carbono amorfo existe en diferentes formas según las condiciones de depósito utilizadas. Sus propiedades mecánicas pueden ser desde similares a polímeros o al grafito a casi tan resistentes como el diamante. Este amplio rango de propiedades se debe a la coexistencia de hibridación sp^2 y sp^3. En general, mayores proporciones de sp^3 conducen a capas más duras. Muchas técnicas de depósito, sin embargo, introducen hidrógeno en las capas, lo que aumenta la proporción de los enlaces tetrahédricos (sp^3) sin aumentar por ello la dureza o resistencia al desgaste. El caso límite, seria un material con propiedades poliméricas. Al rango de materiales con contenidos de hidrógeno reducidos o nulos y con una fracción de hibridación sp^3 importante, se les llama genéricamente carbono amorfo tipo diamante (DLC).

A parte de las excelentes propiedades mecánicas que presenta el DLC, y que se concretan en elevada dureza, gran resistencia al desgaste, alta constante elástica y baja fricción en seco, al carbono amorfo también se le ha encontrado utilidad en aplicaciones en las que se requieren superficies inertes y/o biocompatibles.

El proyecto del Ministerio de Ciencia e Innovación DPI2007-61349, "Moldes de carbono amorfo para micro y nanograbado de superficies poliméricas", pretende es-

tudiar los efectos de la incorporación de diferentes elementos en capas de DLC para la mejora de los moldes de NIL.

Esta tesis se ha centrado en una serie de objetivos de este proyecto, que se han concretado en:

(a) El diseño y la construcción de un reactor de muy alto vacío adecuado para procesos de depósito y grabado iónico.

(b) La incorporación de flúor a capas de carbono amorfo y su posterior caracterización mediante diferentes técnicas de análisis superficial, mecánicas y tribológicas, así como la espectroscópicas para la caracterización del plasma que se usará para su depósito.

(c) La puesta a punto y optimización de la técnica de grabado iónico profundo y de grabado con haz de iones, para la producción de moldes.

(d) El uso de diferentes técnicas litográficas orientadas a la producción en gran área de motivos nanométricos.

(e) La exploración del recubrimiento de moldes con carbono amorfo para incrementar su durabilidad y anti-adhesión, en procesos de nanoestampación.

Las capas se han depositado mediante la técnica de depósito químico en fase vapor activado con plasma (PECVD). El tipo de señal usada para excitar el plasma ha sido la DC-pulsada asimétrica. Esta ha demostrado ser adecuada para el depósito de DLC, y ha sido utilizada desde hace más de seis años en el grupo de investigación FEMAN, donde se ha desarrollado la tesis. A nivel industrial goza de mayor facilidad de implementación que la radiofrecuencia (RF), es más económica y permite una mejor escalabilidad de los procesos. Además, se ha demostrado que el importante estrés compresivo intrínseco de las capas de carbono amorfo, que dificulta su adherencia a los sustratos, se reduce con la utilización de este tipo de excitación del plasma.

La incorporación de flúor en capas de DLC ha demostrado recientemente ser útil en la mejora de las propiedades de los moldes de NIL, porque evita el uso de los actuales tratamientos superficiales (por ejemplpo siloxanos), los cuales, además de ser menos duraderos, pueden reaccionar con los polímeros en presencia de luz UV. Así, en esta tesis se ha estudiado la influencia de la incorporación de flúor a capas de DLC en la composición y en las propiedades de superficiales obtenidas.

A continuación se detalla el trabajo realizado y los resultados obtenidos para cada objetivo:

(a) El diseño y construcción de un reactor de muy alto vacío era un requisito indispensable para la consecución del resto de objetivos tanto del proyecto como de la tesis. Los antiguos reactores disponibles, aun siendo capaces de alcanzar bajas presiones base (10^{-3} Pa), presentaban problemas importantes de estanqueidad, especialmente en relación a los circuitos de refrigeración con agua de los cabezales de pulverización catódica y de PECVD.

Así, la construcción del nuevo reactor se centró en la substitución de la mayor parte de las juntas de vacío de elastoméricas a cobre. Por otro lado, también se renovó el diseño de los cabezales refrigerados por agua para asegurar su completa estanqueidad y durabilidad. Se está considerando la posibilidad de patentar este nuevo diseño de cabezales.
Una vez ensamblado, la comprobación de estanqueidad del reactor en su conjunto se llevó a cabo mediante detección de fugas de helio y la detección de la emisión óptica de plasmas, muy sensible a pequeñas cantidades de nitrógeno.
Finalmente, se diseñó un completo programa de control del reactor mediante LabView, que incluye la totalidad del sistema de vacío (válvulas, medidores de presión y controladores de flujo másico) así como el control de la fuente de potencia DC pulsada (ver figura 3.2). El programa además, permite la automatización de procesos mediante la creación de secuencias donde se pueden ajustar los flujos másicos de cada una de las cuatro líneas de gases controlables de forma simultánea y de la fuente de potencia. Se permite además, el cambio gradual de flujos entre dos elementos de la secuencia.

(b) Para la incorporación de flúor en capas de DLC se partió del trabajo anterior del grupo de investigación en el depósito de este tipo de capas, y se eligieron unas condiciones de depósito mediante plasma pulsado DC de metano, que proporcionasen un buen equilibrio de las diferentes propiedades de las capas. La incorporación de flúor se planeó a través de la sustitución gradual del precursor, de metano (CH_4) a trifluorometano (CHF_3). La relación $R^{gas}_{CHF_3} \equiv \Phi_{CHF_3}/(\Phi_{CHF_3} + \Phi_{CH_4})$, donde Φ_X es el flujo másico del precursor X, se ha utilizado durante toda la tesis. Éste precursor fluorado tiene la ventaja de poderse utilizar tanto para el proceso de depósito de capas, como para el de grabado iónico reactivo. Además, la investigación de este gas como precursor de PECVD para capas de carbono amorfo fluoradas ha sido muy poco investigada hasta ahora.
Las capas se caracterizaron mediante perfilometría, XPS, ángulo de contacto de diferentes líquidos, microscopía de fuerzas atómicas (AFM), tests de fricción y tests de desgaste abrasivo, mientras que el plasma utilizado durante el depósito se analizó por espectroscopía de emisión óptica mediante la adición de un actinómetro (Ar) a los gases precursores (metano y trifluorometano). Los resultados de estas caracterizaciones se resumen, finalmente, en un modelo descriptivo.
La perfilometría permitió medir tanto el ritmo de depósito, como su homogeneidad y también el estrés compresivo intrínseco de las capas. El ritmo de depósito (figura 5.1) incrementó con la adición de precursor fluorado hasta un factor 2, mientras se sufrió una pérdida de homogeneidad, en parte posiblemente debida a las inestabilidades que se observaron en el plasma. En cuanto al estrés (figura 5.3), éste disminuyó con la incorporación de flúor, posiblemente por una pérdida de reticulación y cohesión de las capas.

Los resultados de la caracterización mediante XPS mostraron la presencia de tres elementos en la superficie de las capas: C, F y O (figura 5.4). De estos tres, el oxígeno demostró ser únicamente superficial, y se atribuyó a contaminación superficial, al desaparecer tras un ligero bombardeo iónico de argón. Según los resultados de XPS, la relación F/C aumenta de forma muy lenta con $R^{gas}_{\mathrm{CHF_3}}$ para valores bajos de esta relación, mientras que para valores próximos a 0.8 aumenta de forma significativa (figura 5.5). Por otro lado, el análisis de las funcionalidades asociadas al átomo de carbono (deconvolución del pico C1s; figura 5.6) permite apreciar el incremento gradual de grupos fluorados ($\mathrm{C}-\mathrm{F}_x$), a medida que se aumenta $R^{gas}_{\mathrm{CHF_3}}$. Los enlaces $\mathrm{C}-\mathrm{F}_3$ se observan para $R^{gas}_{\mathrm{CHF_3}} \gtrsim 0{,}75$, mientras que los $\mathrm{C}-\mathrm{F}_2$ y $\mathrm{C}-\mathrm{F}$ se pueden discernir para $R^{gas}_{\mathrm{CHF_3}} \gtrsim 0{,}5$.

En cuanto al ángulo de contacto, se midieron los de cuatro líquidos diferentes en las capas (figura 5.12). Esto permitió el cálculo de la energía libre superficial y la determinación de sus componentes, mediante la teoría de van Oss, Chaudhury y Good (figura 5.13). Los ángulos de contacto de los diferentes líquidos (relacionados con el trabajo de adhesión termodinámico entre sólido y líquido), fueron superiores a los del silicio para $R^{gas}_{\mathrm{CHF_3}} \gtrsim 0{,}25$ excepto en el caso del diiodometano, para el cual fue necesaria la incorporación de mucho más flúor ($R^{gas}_{\mathrm{CHF_3}} \gtrsim 0{,}8$), para observar dicha circunstancia. La energía libre superficial calculada a partir de estos datos, con dos escalas de energía superficial distintas (la original VOCG y la de Della Volpe y Siboni DVS), mostró un ligero descenso con $R^{gas}_{\mathrm{CHF_3}}$, desde los iniciales $40\,\mathrm{mJ/m^2}$, que se acentuó significativamente a partir de $R^{gas}_{\mathrm{CHF_3}} \approx 0{,}8$. Este comportamiento se observó para ambas escalas, de la misma forma que la predominancia de la componente básica sobre la ácida. Por otro lado, la histéresis del ángulo de contacto se ve incrementada para altos valores de $R^{gas}_{\mathrm{CHF_3}}$ (figura 5.14). Este fenómeno se ha relacionado con el incremento que se ha observado en la rugosidad, mediante AFM, para capas con $R^{gas}_{\mathrm{CHF_3}} \gtrsim 0{,}5$ y con la ya mencionada pérdida de homogeneidad del depósito.

Los tests de fricción contra bolas de carburo de tungsteno, mostraron una significativa dependencia con la humedad ambiente. Por este motivo se diseñó, ensambló y puso en marcha un sistema de control de humedad en la cámara del nanotribómetro. Éste consistió en un burbujeador de agua a una temperatura controlada, por el que se hacía pasar un flujo de nitrógeno regulado mediante un controlador de flujo másico. El flujo se determinaba mediante la retroalimentación del controlador con la lectura de un medidor de humedad.

De esta forma se determinó la dependencia de la fricción con la humedad en capas con diferentes proporciones de flúor (figura 5.17). La presencia de agua en el ambiente mostró la capacidad de reducir la fricción en todas las capas, y de estabilizarla en valores bajos cuando la humedad relativa es elevada. Esto se interpreta en base a la eliminación superficial de hidrógeno, y posiblemente de flúor, por efecto de la fricción y del aumento de disponibilidad de hidrógeno y

grupos hidroxilos para pasivar la superficie con la humedad. La estabilización de la fricción significaría la saturación de la superficie con agua.
Finalmente, los tests de desgaste mostraron una gran resistencia de las capas, con valores de ritmo de desgaste que incrementan muy ligeramente con $R^{gas}_{\mathrm{CHF_3}}$ (figura 5.18). Sin embargo, para valores de $R^{gas}_{\mathrm{CHF_3}}$ más altos de 0.8 se observa una pérdida repentina de resistencia, incluso más acentuada que el incremento en incorporación de flúor, determinado por XPS. Esto sugiere un cambio estructural importante de las capas para concentraciones altas de flúor.
En cuanto a la emisión óptica del plasma, el uso del actinómetro permitió determinar la evolución de la concentración de diferentes especies y átomos. Las especies observadas fueron el propio actinómetro (Ar), flúor, hidrógeno, CHF, CH y CF_2. Las medidas revelaron que las especies CH son exclusivamente producidas por el metano, mientras que el hidrógeno atómico, presente en el plasma, lo proveen ambos precursores en relación estequiométrica (figura 5.9). Por otro lado, la emisión del flúor atómico sufre un primer incremento con $R^{gas}_{\mathrm{CHF_3}}$ para posteriormente estabilizarse y volver a disminuir.
Todos estos resultados provenientes tanto de la caracterización de la capa como del plasma, se han explicado con un modelo descriptivo basado en los comúnmente aceptados para el crecimiento de carbono amorfo hidrogenado.
Para valores de $R^{gas}_{\mathrm{CHF_3}}$ bajos, el bombardeo de la capa con cationes y la reacción de ésta con átomos neutros de hidrógeno, evita que la ya pequeña cantidad de flúor en el gas precursor, se incorpore a la capa, debido a la reacción con hidrógeno y la formación de HF volátil. Este mecanismo también se da con los enlaces C–H, debido a la posibilidad de formar hidrógeno molecular, pero en menor medida debido a la gran abundancia de este elemento en el gas precursor.
Sin embargo, para valores más elevados de $R^{gas}_{\mathrm{CHF_3}}$, la reducción de hidrógeno en el gas y su sustitución por un átomo fuertemente electronegativo, reduce el bombardeo causado por especies hidrogenadas como hidrógeno atómico y CH. Esta reducción perme a su vez al flúor permanecer en la capa, lo cual explica la disminución de la emisión del flúor atómico en el plasma y el importante cambio estructural y de composición, cuando la proporción de metano se acerca a cero, que evidencian las propiedades de superficie analizadas: rugosidad, energía superficial y ritmo de desgaste, así como los resultados de XPS.

(c) De cara a fabricar nanoestructuras en grandes áreas, se ha trabajado en dos líneas. Por un lado se ha optimizado un proceso de grabado iónico reactivo profundo que combina diferentes gases para conseguir paredes verticales y superficies poco rugosas. Por otro lado, se ha estudiado el funcionamiento y características de un cañón de iones, mediante el cuál se puede controlar la direccionalidad del grabado, lo cual permite generar estructuras con anisotropía en el plano de la muestra para diferentes aplicaciones ópticas o propiedades superficiales anisotrópicas.

Respecto al grabado iónico reactivo profundo, se seleccionó la combinación de gases SF_6, O_2 y CHF_3 que permiten controlar el ritmo de grabado, la protección química de la pared, necesaria para conseguir su verticalidad, y una rugosidad reducida de las superficies. Inicialmente se escogió el aluminio como máscara para estos procesos, debido a su muy alta resistencia al ataque, y por lo tanto alta selectividad del proceso. Con esta máscara se investigó buena parte del espacio de flujos de los tres gases (figura 6.1), y se determinó la rugosidad y velocidad del ataque para cada uno (figuras 6.2 y 6.4). Sin embargo, los efectos de generación de micromáscaras por parte del aluminio, que hacía aumentar la rugosidad, no permitió la consecución de un proceso con superficies lisas. Eso motivó el estudio del empleo de óxido de silicio como máscara. En el caso del aluminio, la estructuración se hizo mediante la técnica "lift-off", consistente en depositar el aluminio sobre una resina previamente litografiada y luego eliminar la resina por métodos químicos. Así, el aluminio solo quedaba donde no había anteriormente resina. En el caso del óxido de silicio, sin embargo, el procedimiento fue diferente. El óxido de silicio se crecía térmicamente en el mismo sustrato de silicio y previo depósito y proceso de litografía en una resina, se atacaba con CHF_3 puro. Las máscaras de óxido de silicio, si bien no proporcionaban tan alta selectividad como las de aluminio, permitieron obtener superficies mucho menos rugosas. Así, finalmente se determinaron los parámetros de un proceso con el que se obtienen paredes verticales, baja rugosidad y alta selectividad.
El cañón de iones incorporado al reactor, se caracterizó mediante una copa de Faraday. Con este dispositivo se determinó la dependencia de la energía de los iones respecto los parámetros de funcionamiento de la fuente. Además, se determinó la función de distribución de energía de los iones con un valor de dispersión de energía ligeramente superior al nominal proporcionado por el fabricante, lo que podría ser debido a una diferencia en la presión de trabajo (figura 6.8). Por otro lado, mediante la copa de Faraday se determinó que la densidad de corriente iónica aumenta con el valor absoluto del voltaje de la rejilla aceleradora (negativo) lo que significa que la rejilla aceleradora colima el haz, puesto que no puede influir en la cantidad total de iones que salen de la fuente (figura 6.9). Finalmente, se calibró el ritmo de ataque del silicio para incidencia normal con diferentes configuraciones de voltaje de pantalla y acelerador (figura 6.10).

(d) Para conseguir la estructuración en grandes áreas con patrones nanométricos, se han utilizado dos técnicas litográficas distintas. Por un lado, se ha utilizado la litografía de haz de electrones (EBL), consistente en sensibilizar una resina mediante un haz de electrones y posteriormente revelarla, para eliminarla o mantenerla en las zonas sensibilizadas (dependiendo del carácter positivo o negativo de la resina) y descubrir así, de forma selectiva, determinadas regiones del sustrato. Esta técnica permite la realización de estructuras de pocas

decenas de nanómetros con patrones de elevada complejidad en grandes áreas, al precio de un equipo muy costoso y de varios días de funcionamiento automatizado continuado para algunos cm^2 en una muestra. Por otro lado, la técnica de litografía coloidal (CL), consistente en el depósito de una monocapa de partículas en un sustrato y su posterior utilización como máscara, supone una alternativa válida para algunas aplicaciones, con la ventaja de la elevada sencillez, rapidez y bajo coste.

El equipo de EBL que se utilizó inicialmente fue el instalado en los Serveis Cientifico-Tècnics de la Universitat de Barcelona. Sin embargo, las limitaciones de este equipo en lo relativo a la estructuración de grandes áreas planteó la necesidad de utilizar un equipo más sofisticado. Por ese motivo se solicitó la concesión de un proyecto de trabajo en la instalación científica y tecnológica singular (ICTS) del Instituto de Sistemas Optoelectrónicos y Microtecnología de la Universidad Politécnica de Madrid, que está equipada con un sistema de EBL de última generación. Con este equipo se pudieron realizar litografías con motivos de hasta 30 nm separados 67 nm y en áreas de $5 \times 5\,mm^2$. Estas litografías fueron posteriormente atacadas con el grabado iónico reactivo profundo, y se obtuvieron estructuras con altas relaciones de aspecto de hasta 6:1 (figura 6.7).

Para la CL se utilizaron monocapas de partículas submicrométricas de sílice depositadas con empaquetamiento hexagonal compacto mediante la técnica de Langmuir-Blodgett (figura 6.11). En este caso se utilizó el cañón de iones, que mediante el cambio de ángulo de incidencia del haz de iones, permitió introducir anisotropías en el grabado (figura 6.13). Del análisis de las micrografías de barrido electrónico, se extrajo la profundidad del ataque, que se había realizado durante diferentes tiempos en cada muestra (figura 6.12). La altura de los pilares de sección circular resultantes del ataque en incidencia normal aumentó con el tiempo del mismo, hasta un cierto punto en el que las partículas (máscara) empezaban a reducir su diámetro debido al ataque. A partir de ese momento la parte superior de los pilares empieza a ser atacada y los bordes los mismos pierden definición. Para ataques más largos, los pilares acaban desapareciendo otra vez. Cuando el ataque se realiza con incidencia oblicua, el ritmo de grabado es superior. Esta dependencia con el ángulo es consistente con los resultados reportados en la literatura [Giannuzzi and Stevie, 2005]. En esta configuración, además, se producen patrones con anisotropía en el plano, que pueden ser de utilidad para determinadas aplicaciones.

(e) Con el fin de explorar la viabilidad del recubrimiento de nanoestructuras con capas de carbono amorfo, las producidas con CL y con cañón de iones, en incidencia normal, se recubrieron con una capa de DLC (sin flúor) de 50 nm. Todas las muestras fueron recubiertas con una capa conforme (figura 6.15). El previsible intenso bombardeo del proceso aparentemente no afectó las estructuras, aunque los bordes de los pilares se vieron suavizados. Este cambio, sin

embargo, es probable que sea debido al hecho que el grosor de la capa es del orden de la altura de los pilares, por lo que el cambio relativo de forma es más acentuado.

Conclusiones:

- Se han depositado capas de carbono amorfo fluorado mediante depósito químico en fase vapor activado por plasma DC pulsado, a través de la progresiva sustitución del metano por trifluorometano. El dispositivo experimental empleado para el depósito ha sido dieñado y construido para permitir diferentes procesos en el mismo reactor. Los resultado del estudio de las capas muestran la viabilidad de esta técnica, de fácil aplicación industrial, para el depósito de este tipo de recubrimientos.

- La caracterización tanto de las especies activas presentes en el plasma como de los grupos incorporados en las capas depositadas han ayudado a la comprensión del proceso de incorporación de flúor así como del cambio en las propiedades superficiales que éste conlleva.

- Para concentraciones de trifluorometano en metano inferiores al 80 %:

  - La relación F:C en la capa muestra una dependencia débil con la fracción de precursor fluorado y aumenta lentamente desde cero hasta una relación 1:4. Los enlaces $C-F$ y $C-F_2$ empiezan a detectarse a partir del 50 % de trifluorometano y aumentan con la concentración de éste.
  - La energía superficial total sufre un ligero descenso de $44\,mJ/m^2$ a $40\,mJ/m^2$, mientras la componente ácido-base se reduce linealmente hasta cero para trifluorometano puro.
  - La humedad juega un papel significativo en la fricción, al reducirla y finalmente estabilizarla en valores bajos, cuando la humedad relativa alcanza valores elevados. Este comportamiento se interpreta sobre la base de la eliminación superficial de hidrógeno, y posiblemente de flúor, por efecto de la fricción y del aumento de disponibilidad de hidrógeno y grupos hidroxilos, con la humedad, para pasivar la superficie.
  - La resistencia al desgaste abrasivo y la rugosidad cambian ligeramente con la concentración de trifluorometano. La primera se mantiene entre cinco y siete veces superior al silicio, mientras la segunda mantiene la rugosidad de nivel atómico del carbono amorfo sin flúor.
  - La combinación de propiedades en este rango hace adecuadas las capas para recubrimientos anti-adhesivos y resistentes al desgaste.

- Para concentraciones de trifluorometano superiores al 80 %, las capas experimentan un súbito e importante cambio estructural y químico que:

  - Incrementa la relación F:C en la capa hasta 1:1, junto con una mayor concentración de los enlaces $C-F$, $C-F_2$ y $C-F_3$.
  - Aumenta la rugosidad en un orden de magnitud a la vez que se incrementa el número de defectos en la capa.
  - Reduce la energía superficial a valores similares al PTFE de $18\,mJ/m^2$ sin apenas contribución ácido-base.
  - Provoca una combinación de pérdida de adhesión a la capa de cimentación y de disminución de reticulación y cohesión interna, con valores del ritmo de desgaste abrasivo que podrían ser de alrededor de un orden de magnitud mayores que los de las capas menos fluoradas.

- La mezcla de trifluorometano y metano ha demostrado incrementar el ritmo de depósito y disminuir el estrés compresivo intrínseco de las capas. Ambos fenómenos podrían estar relacionados con una reducción de la densidad de las capas y la pérdida progresiva de cohesión.

- Las medidas de actinometría espectroscópica de emisión óptica han revelado que las especies CH son producidas exclusivamente por el metano, mientras que el hidrógeno atómico, presente en el plasma, proviene de ambos precursores en relación estequiométrica. Además de estas especies, las medidas han mostrado la presencia de CF_2, CHF y flúor atómico en el plasma.

- A partir de la caracterización de las especies activas en el plasma y de la composición de las capas depositadas, se ha elaborado un modelo descriptivo de los mecanismos que controlan la incorporación de flúor, sobre la base de los mecanismos comúnmente aceptados en la comunidad científica para capas sin flúor:
  Para cantidades pequeñas de trifluorometano en el plasma, el bombardeo de la capa con cationes y la reacción de ésta con átomos neutros de hidrógeno, evita que la ya pequeña cantidad de flúor en el gas precursor, se incorpore a la capa, debido a la reacción con hidrógeno y la formación de HF volátil. Este mecanismo también se da con los enlaces C–H, de los cuales se forma hidrógeno molecular, pero en menor medida debido a la gran abundancia de este elemento en el gas precursor.
  Cuando la cantidad de trifluorometano se incrementa, la reducción de hidrógeno en el gas y su sustitución por un átomo fuertemente electronegativo, reduce el bombardeo causado por especies hidrogenadas como hidrógeno atómico y CH. Esta reducción permite a su vez al flúor permanecer en la capa, lo cual explica la disminución de la emisión del flúor atómico en el plasma y el importante cambio estructural y de composición, cuando la proporción de metano se acerca a cero, tal como evidencian las propiedades de superficie analizadas: rugosidad, energía superficial y ritmo de desgaste, así como los resultados de XPS.

- En cuanto a la fabricación de moldes para litografía por nanoestampación, se han explorado dos técnicas diferentes con configuraciones adecuadas para la estructuración en gran superficie. De este modo se completa uno de los objetivos de la tesis y del proyecto SURFaC. Con litografía de haz de electrones se ha conseguido producir estructuras de hasta 30 nm separadas 67 nm y en una extensión de $5 \times 5\,\mathrm{mm}^2$. Por otro lado, la litografía coloidal ha permitido la producción de estructuras periódicas con motivos de alrededor de 300 nm sobre áreas de $20 \times 20\,\mathrm{mm}^2$. La combinación de las técnicas litográficas en gran área con las capacidades de grabado iónico profundo o direccional abre la posibilidad de producir tanto moldes de nanoestampación como otros materiales nanoestructurados con propiedades macroscópicas observables.

- La técnica del grabado iónico profundo se ha optimizado para conseguir baja rugosidad, junto con alta verticalidad de las paredes y moderada selectividad. Concretamente, se han conseguido combinar en un mismo proceso ritmos de grabado de alrededor de 200 nm/min con selectividades de 4.5 y paredes totalmente verticales.

- Se han realizado experimentos de ataque iónico con diferentes duraciones y ángulo de incidencia mediante el cañón de iones, y se han descrito y explicado las diferentes fases del ataque en función del grabado simultáneo de máscara y substrato. La transferencia anisotrópica de patrones al substrato abre la puerta a la fabricación de dispositivos de nanofluídica o cristales fotónicos.

- Globalmente, las propiedades de las capas depositadas apuntan a su utilidad para el recubrimiento de superficies que requieren baja energía superficial combinada con alta resistencia mecánica. Además, el recubrimiento conforme de nanoestructuras abre las puertas al uso de estas capas en moldes con patrones nanométricos como los utilizados en litografía por nanoestampación.

- Como trabajo futuro, también en el marco del proyecto SURFaC, sería interesante investigar en más profundidad el depósito de capas con concentraciones de trifluorometano superiores al 80 %, para lo cual haría falta mejorar la adhesión a la capa de cimentación.

Table of Contents

List of Figures

List of Tables

Nomenclature

AFM Atomic Force Miscroscopy

CVD Chemical Vapor Deposition

DC Direct Current

DLC Diamond-like carbon

EBL Electron Beam Lithography

ECWR Electron Cyclotron Wave Resonance

EEDF Electron Energy Distribution Function

EPL Electron Projection Lithography

EUV Extreme UV lithography

FCVA Filtered Cathodic Vacuum Arc

FDLC Fluorinated DLC

FIB Focused Ion Beam

HVAC Heating Ventilating and Air Conditioning. Sometimes referred to as climate control

IBE Ion Beam Etching

ICP Inductively Coupled Plasmas

LF Low Frequency (30 kHz to 300 kHz)

MFC Mass Flow Controller

MFM Magnetic Force Miscroscopy

MSIB Mass-Selected Ion Beam

MW Microwave (2.45 GHz)

NIL Nanoimprint Lithography

OEA Optical Emission Actinometry

PBS Plasma Beam Source

PECVD Plasma Enhanced Chemical Vapor Deposition

PLC Polymer Like Carbon

PMMA Polymethylmethacrylate

PTFE polytetrafluoroethylene

PVC Polyvinyl chloride

PVF Polyvinyl fluoride

RF Radio Frequency (13.56 MHz)

RF-PECVD Radio Frequency driven PECVD

RH Relative Humidity

RIE Reactive Ion Etching

RMS Root Mean Square

SCT-UB Scientific and Technical Services of the Universitat de Barcelona

SEM Scanning Electron Microscope

SPM Scanning Probe Microscopy

T-NIL Thermal NIL

UV Ultra Violet

UV-NIL UV-assisted NIL

XPS X-Ray Photoelectron Spectroscopy

Part I.

State of the art

1 Nanoimprint lithography

1.1 Scaling down

Since the advent of the first transistor around 1947 by Texas Instruments' scientists, and the development of the first integrated circuit in 1958, by the same company, a lot of effort has been put on scaling down this devices.

In 1965, Intel's engineer Gordon Moore, wrote about the trend of increase of transistor density on integrated circuits for the upcoming decade, and in 1975 he forecasted a doubling in the number of transistors that could be placed inexpensively on an integrated circuit every two years.

Since then, Moore's law has become a target for integrated circuits manufacturers and hold true by the improvements on the lithographic techniques used for microprocessor fabrication. Specifically, the technology mostly used in the industry (UV lithography) has evolved toward shorter UV wavelengths as the required feature size has been reduced (see figure 1.1). After the diffraction limit, for feature sizes smaller to that of the wavelength, further improvements have been done by using optical proximity correction [Chen et al., 1997], phase-shifting masks [Levenson et al., 1982], immersion lithography [Pfeiffer et al., 1999] or double-patterning [Flagello et al., 2004].

During the last decades, diverse alternative approaches to UV lithography have been sought after in order to replace it when their limits are reached. These have been called new generation lithography techniques (NGL). During the 1970s, electron beam lithography (EBL) [Heidenreich et al., 1973] was the most popular, but it was soon replaced as an alternative by X-Ray lithography [Spears and Smith, 1972] in the 1980s and early 1990s, due to its reduced throughput. Extreme UV lithography (EUV) [Zernike, 1994] succeeded both of them from the mid-1990s to mid-2000s, because of the high costs involved with X-Ray lithography. However, none of them has finally been used in industrial processes, as UV lithography has continued to improve its resolution.

More recently, nanoimprint lithography (NIL), a new technique developed in the late 1990s, has been adopted as the NGL, their strong points being its inherent ease of implementation and high resolution (sub-10 nm). It is to this technique, what this chapter is devoted to.

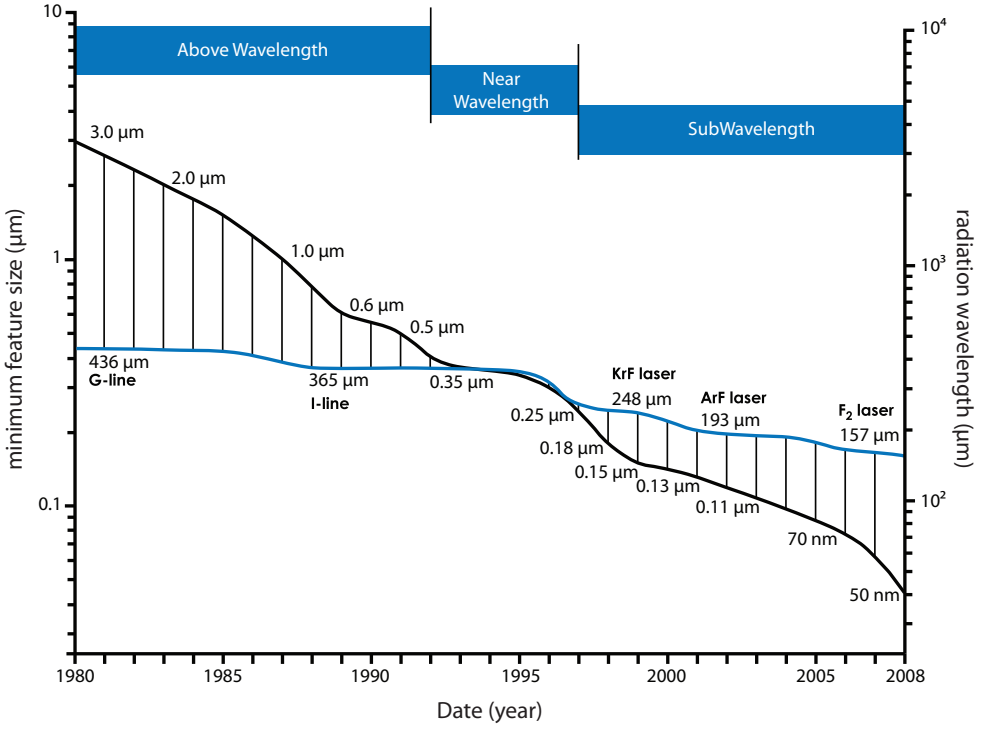

Figure 1.1.: UV lithography technology evolution since 1980. Blue lines is the wavelength used while the black line represents the minimum feature size.

1.2 Advent and fundamentals

When certain soft materials (specially thermoplastics) are pressed and heated, they acquire the topography of the pressing element. For example, when you press wax with your finger, your body temperature and the pressure you apply transfer the topography of you finger skin on the wax surface. This simple and old principle was used by Chou et al in 1997 [Chou and Krauss, 1997; Chou et al., 1997] to demonstrate a technique named nanoimprint lithography (NIL) capable of reproducing nanometric patterns with sub-10 nm features on polymethylmethacrylate (PMMA).

This technique was a breakthrough in lithography because in addition to the high resolution that had been proved, it required a extraordinary simple setup compared to other state-of-art lithography equipments such as extreme UV lithography (EUV) or parallel electron beam lithography, and was able to operate in parallel, as opposed, for example to common EBL equipments. In 2003 it was added to the international technology roadmap for semiconductors (ITRS) for the 32 nm node and beyond.

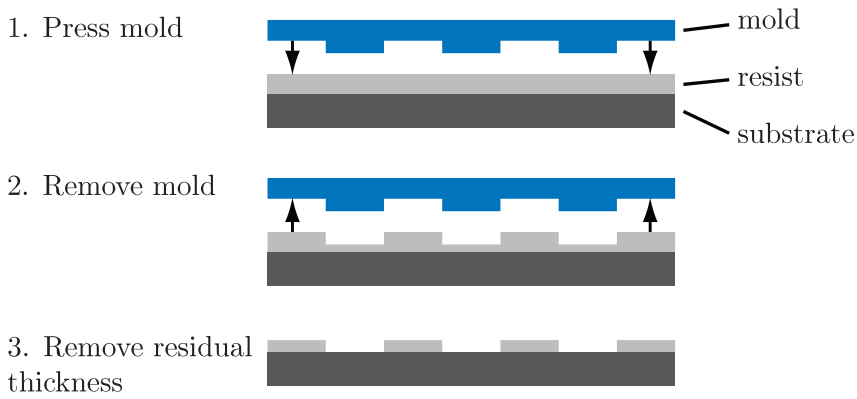

Figure 1.2.: Basic NIL process. Substrate and resist are heated up; mold is pressed on the resist; temperature is reduced and pressure is released. In some cases, it may be interesting to remove the residual thickness by plasma etching.

A common nanoimprint transfer process (see figure 1.2) requires a hard mold (also called stamp and usually made of Si or SiO_2), and a thermoplastic (resist) in the form of a thin film (from tenths of nm to a few µm) on top of a hard substrate. The process starts heating the resist to a temperature over its glass transition, in order to decrease the resist's viscosity. The mold is then pressed against the coated substrate at a few MPa and is left for some time to allow the resist to flow to all the cavities of the mold. Finally, the temperature is decreased, and the pressure is relieved. The transferred pattern can then be used for other purposes, like processing of the underlying substrate. To do this, the residual thickness of resist remaining on the thin areas of the pattern, has to be removed by thinning all the polymer layer (usually a short plasma etching).

A few years after Chou et al.'s demonstration, UV light started to be used to photopolymerize the resist after the application of pressure [Coburn and Chen, 1980]. The advantage of such approach is the possibility of avoiding thermal cycles, and also a much faster processing, at the expense of a more expensive equipment and complex processing of the mold (so that it can be transparent to UV light). The new technique was named UV-NIL, while the original one was referred to as thermal-NIL (T-NIL).

1.3 Applications

Nanoimprint lithography both in its UV or thermal variants has not only attracted the attention of the microelectronic industry, but also of a number of scientific and industrial fields for which a cheap technique for mass nanopatterning is of interest.

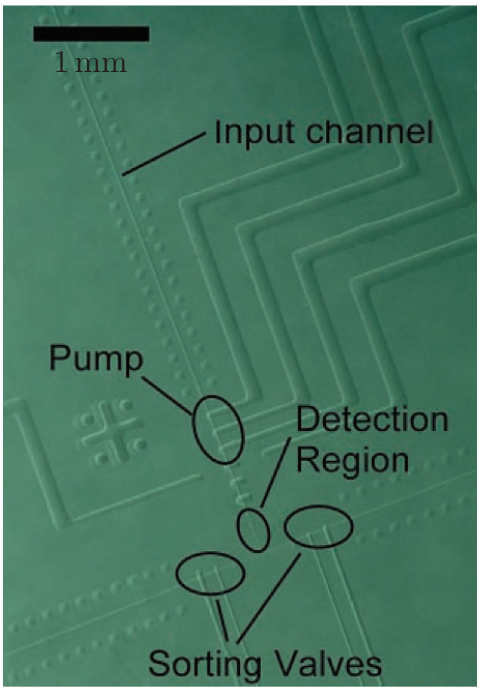

(a)

(b1)

(b2)

Figure 1.3.: (a) A micrometer sized cell sorter with integrated valves and pumps fabricated with standard methods [Quake and Scherer, 2000].; (b) Two level nanochannels with offset (b1) and aligned (b2) fabricated with nanoimprint lithography [Reano and Pang, 2005].

Besides microelectronic applications, different uses of nanoimprint lithography can be found in the literature, such as for nanofluidics, biological and biochemical chips and sensors, and optical waveguides and devices, among others.

In the newly emerging field of bionanotechnology, extremely small nanofluidic structures need to be fabricated and used as matrices for the manipulation and analysis of biomolecules such as DNA and proteins at single molecule resolution [Han and Craighead, 2000; Quake and Scherer, 2000]. Nanoimprint lithography has proven to be a suitable technique for this purpose. Millimetric sized nanofluidic devices can be fabricated with this technique, with channel cross-sections as small as $10 \times 50\,\mathrm{nm}$ [Cao et al., 2002]. Other nanofluidic devices such as electrokinetic fluid pumps have also been fabricated recently by patterning an array of interdigitated asymmetric micro-electrodes on a previously formed micro-channel [Studer et al., 2002]. Nanoimprint lithography also permits the fabrication three-dimensional nanochannel networks (see figure 1.3) [Reano and Pang, 2005].

Biology has found in NIL a cheap an convenient way of mass producing biosensors and biochips. Microring waveguides, for example, have been used to detect biomolecules in solutions surrounding the structure with high sensitivity [Chao et al., 2006] and DNA electrophoresis chips improve the efficiency of DNA molecules separation for application in the Human Genome Project or human polymorphism analysis [Pépin et al., 2002].

Nanoimprint lithography has also been investigated for improved functionality of solar photovoltaic cells. Transparent and conducting layers, for example, have been fabricated by patterning a metal with NIL [Kang et al., 2008]. Regarding the electron acceptor/donor interface, the artificial increase of its area by NIL has increased the fill factor, the power conversion efficiency and the short circuit current, without affecting the open circuit voltage [Kim et al., 2007].

Briefly, the most benefited applications by nanoimprint lithography are those requiring a high number of nanopatterned samples for which UV lithography is not a solution because of the limited resolution and other nanopatterning techniques are not suitable because of the low throughput.

1.4 Demolding

A fundamental point in NIL is the good anti-sticking properties of the mold. The surface of the mold must be such that the polymer slips when the mold is detached, without damaging the resist nor the mold. Besides mechanical considerations such as roughness of the mold surface, or cavities in the mold that wouldn't allow the polymer to move in a direction normal to the substrate surface, the adhesion between mold and polymer surfaces must be sufficiently low.

If the stamp material does not exhibit such properties, either anti-sticking coating is applied to the mold, or modified resists for decreased adhesion to mold material have to be used [Kim et al., 2008]. The most common anti-adhesive coating for Si molds is $F_{13} - TCS$[1] with surface energy of $12.4\,mJ/m^2$ (calculated using geometric mean - Owen's method; see section 4.1) [Beck et al., 2002; Schift et al., 2005], also known as the silanation process, but other self-assembled monolayers have also been used for this purpose, such as OTS[2] or FDTS[3], [Wu et al., 2007], or variations of $F_{13} - TCS$. These coatings are applied either by immersion (in OTS), or by chemical vapor deposition (CVD) at room temperature (T_R) or at a few tenths of degrees Celsius over T_R (for FDTS).

The main disadvantages of this type of coatings are that they are very vulnerable to mechanical abrasion (repeated use deteriorates its functionality) and that their feasibility depends on the presence of hydroxyl groups on the mold surface. In

[1] tridecafluoro-(1,1,2,2)-tetrahydrooctyl)-trichlorosilane, or 1H,1H,2H,2H-perfluorooctyl-trichlorosilane

[2] octadecyltrichlorosilane

[3] perfluorodecyltrichlorosilane

addition, the immersion technique presents uniformity problems depending on how the particular surface structure affects wettability. The problem with repeated use becomes particularly problematic when the coated mold is used in UV-NIL processes. UV light has shown to deteriorate the chemical stability of the coating, by creating volatile subproducts with fluorine, and thereby decreasing the concentration of this element on the film overtime [Tao et al., 2008]. The search of alternative anti-sticking layers for UV-NIL is therefore, particularly important for industrial application.

For metallic molds such as those made of Ni, the use of alkyl phosphate salts monolayers has been studied [Keil et al., 2004], providing good anti-sticking functionality and moderate resistance to abrasion. However, its dependence again of the chemical termination of the mold prevents a widespread use with independence of the mold material. The use of trichlorosilanes on metallic surfaces depends upon the deposition of an oxide layer on the metallic mold prior to the treatment. Ni molds have been successfully silanated depositing different oxides (SiO_2, TiO_2 and NiO), the best results being provided by the silicon dioxide [Park et al., 2004].

Other methods such as ion sputtering of PTFE[4], using CHF_3 as feed gas, have also been studied [Jaszewski et al., 1997, 1999]. These coatings have shown to have similar surface energies to that of PTFE, and a durability comparable to that of silanation. Moreover, these films can be deposited on molds other than Si or SiO_2. However, their resistance to abrasion, other than that produced by the imprint, was not studied.

Plasma polymerization from fluorocarbon gases has also been explored as a way of obtaining low surface energy coatings [Schulz et al., 2000]. Mostly deposited from C_4F_8 gas, the films have shown surface energies down to $17\,mJ/m^2$ (calculated using harmonic mean - Wu method; see section 4.1) with water contact angles about 105°.

More recently, a few months after we started to work on the same idea, amorphous carbon films were first used as an anti-sticking coating for nanoimprint molds [Park et al., 2006]. In that study, three-dimensional molds were coated with diamond-like carbon (DLC; see chapter 2) which presented a contact angle of about 70° with a home-made UV-curable resist based on TPGDA[5].

In September 2006 fluorinated DLC (FDLC) was first used as coating material for nanoimprint molds independently by two different groups [Nakamatsu et al., 2006; Altun et al., 2006].

Although Nakamatsu et al. did not provide many details about the experimental setup they used, their regular DLC films, deposited by RF-PECVD showed a water contact angle of 73° while after fluorination (16 at.%), this value rose to 103°. The coated mold sustained 100 imprint processes while keeping the same value for the water contact angle. With regard to hardness, this magnitude only decreased from 26 GPa to 24 GPa after fluorination. The calculated surface energy for the FDLC was $23\,mJ/m^2$.

[4] polytetrafluoroethylene
[5] tripropylene glycol diacylate

On the other hand, Altun et al. published a more detailed study of films with different fluorine concentrations of up to 38 at.%. The films were deposited by simultaneous sputtering of both graphite and PTFE and later on, they were structured by O_2 ion etching. Water contact angle raised from 60° for non fluorinated DLC to about 105° for the maximum amount of fluorine, while UV transmittance increased from 1% to almost 40% (200 nm thick films). Regarding hardness, 10 at.% F films kept almost the same value as DLC films (12.7 GPa), but further fluorination decreased hardness to 4.5 GPa and 1.9 GPa for fluorine concentrations of 25 at.% and 38 at.%. The produced molds could be successfully used for UV-NIL without requiring additional anti-sticking treatments.

2 Amorphous carbon

2.1 Carbon, a versatile element

The peculiar electronic configuration of carbon atoms, $1s^2 2s^2 2p^2$, and the small energy difference between their 2p and 2s orbitals, compared to the binding energy of the carbon bonds, allow the electrons to rearrange in s and p mixed orbitals that enhance the binding energy with other atoms. This process is called hybridization and produces three different types of orbitals: $sp = s + p$, $sp^2 = s + p + p$ and $sp^3 = s + p + p + p$.

Each different bonding state corresponds to a certain structural arrangement: sp bonding gives rise to chain structures, with the following configuration (every arrow signifies an electron with its spin direction):

$$\underset{1s}{\uparrow\downarrow}\ \underset{sp}{\uparrow}\ \underset{sp}{\uparrow}\ \underset{p}{\uparrow}\ \underset{p}{\uparrow}$$

which corresponds to two σ bonds and two π bonds. On the other hand, sp^2 bonding conforms onto planar structures:

$$\underset{1s}{\uparrow\downarrow}\ \underset{sp^2}{\uparrow}\ \underset{sp^2}{\uparrow}\ \underset{sp^2}{\uparrow}\ \underset{p}{\uparrow}$$

corresponding to three σ bonds and one π bond. Finally, sp^3 bonding produces tetrahedrical structures:

$$\underset{1s}{\uparrow\downarrow}\ \underset{sp^3}{\uparrow}\ \underset{sp^3}{\uparrow}\ \underset{sp^3}{\uparrow}\ \underset{sp^3}{\uparrow}$$

with four σ bonds.

The smaller overlapping of p orbitals makes π bonds weaker than σ bonds. However, a number of scenarios are possible. Sometimes, as in ethene (C_2H_4), a σ and π bond combine producing a stronger bond between carbon atoms. This is called a double bond: C=C. Triple bonds consist of a σ bond and two π bonds, as in ethyne (C_2H_2). Although chemically stronger thanks to double bonds, the mechanical stability obtained with sp^2 hybridization is limited, due to the planar geometry.

Category	Hardness (GPa)	sp^3 content (%)	Band gap (eV)	Density (g/cm^3)	H content (%)
DAC or DLC	20–40	40–60	0.8–4.0	1.8–3.0	20–40
TAC	40–65	65–90	1.6–2.6	2.5–3.5	0–30
PAC or PLC	Soft	60–80	2.0–5.0	0.6–1.5	40–65
GAC	Soft	0–30	0.0–0.6	1.2–2.0	0–40
NAC	20–40	30–80	0.8–2.6	2.0–3.2	0–30

Table 2.1.: Typical properties for different forms of amorphous carbon films. The acronyms stand for: Diamond-like a-C (DLC), Tetrahedral a-C (TAC), Polymer-like a-C (PLC), Graphitic a-C (GAC) and Nanocomposite a-C (NAC), respectively. Extracted from [Silva, 2003].

Instead, sp^3 hybridization allows the creation of a three dimensional network of σ bonds.

Due to this variety of possible bonding configurations, carbon has a number of allotropes: graphene (sheet of sp^2 bonded carbons: σ bonds plus delocalized π bonds), carbon nanotubes and fullerenes (graphene sheets rolled over themselves forming cylinders or spheres, respectively), graphite (Bernal stack of graphene sheets), diamond (network of sp^3 bonded carbons) and amorphous carbon (cross-linked and non-organized carbon matrix with a mixture of sp^2 and sp^3 bonds). It is to the latter that this chapter is devoted to.

2.2 Amorphous carbon and diamond-like carbon

Amorphous carbon is defined by the International Union of Pure an Applied Chemistry (IUPAC) as:

> "A carbon material without long-range crystalline order. Short range order exists, but with deviations of the interatomic distances and/or interbonding angles with respect to the graphite lattice as well as to the diamond lattice."

Depending on the ratio of sp^2 and sp^3 bonds in the matrix, amorphous carbon (a-C) presents a variety of mechanical properties outlined in table 2.1 and described next.

Tetrahedral amorphous carbon films (ta-C or TAC) present the highest hardness, with a high degree of sp^3 bonding and low hydrogen content. It is almost exclusively deposited by filtered cathodic vacuum arc (FCVA), [Martin et al., 1988; McKenzie et al., 1991; Fallon et al., 1993] although other techniques such as mass-selected ion

beam (MSIB) [Kaukonen and Nieminen, 1992; Miyazawa et al., 1984] or laser deposition [Scheibe and Schultrich, 1994; Voevodin and Donley, 1996] can also be used. For the hydrogenated version of ta-C, plasma beam source (PBS) [Weiler et al., 1996] and electron cyclotron wave resonance (ECWR) [Morrison et al., 1999] have been used. Despite the high resemblance to diamond on its short range microstructure and mechanical properties, its optoelectronics properties are controlled by the small percentage of sp^2 electrons with energies close to the Fermi level. [Silva, 2003]

On the other hand, films with comparable degrees of sp^3 bonding but soft are named polymer like carbon (PLC). These films have high H content (above 40%) which terminates single bonds and therefore reduces carbon-carbon cross-linking. The quantity of sp^3 bonds is high due to hydrogen's preferential bonding to carbon in sp^3 configuration, but this is no longer related to enhanced hardness. This kind of films present a small amount of defects compared to other types and have a wide bandgap [Silva et al., 2002].

Films with intermediate hydrogen content can be either hydrogenated ta-C or hydrogenated a-C (a-C:H). The latter is the most studied type of a-C films and has been known in the literature as diamond-like carbon (DLC). It is softer than ta-C(:H) but still harder than most materials: values ranging from 20 to 40 GPa. Density is also slightly smaller than that of ta-C(:H). Its main advantage is the simple setup for its deposition. A wide range of deposition techniques is available compared to the complex setup for ta-C deposition [Aisenberg and Chabot, 1971; Zou et al., 1989; Koidl et al., 1990; Kessels et al., 1998]. Also, DLC has a wider range of optical gaps than ta-C depending on the deposition conditions, which enables it for applications such as UV nanoimprint molds, where middle or near UV light transmission is necessary. For shorter wavelengths, thin films allow to further extend the working range.

Figure 2.1 shows the space of film types depending on the $sp^2 : sp^3$ ratio and H content. Figure 2.1a is an updated version of the popular diagram by [Ferrari and Robertson, 2000] which includes hydrogenated films. Figure 2.1b by [Silva, 2003] presents a revised diagram based on a wider review.

High hardness and elastic modulus are the main features of a-C:H and ta-C(:H) films. However, the rigid network of the films produces a high intrinsic compressive stress up to 12 GPa [Ferrari et al., 2002]. This is an important drawback in the production of DLC coatings, since it limits the thickness depending on the adhesion to the substrate. For badly adhered or too thick films, cracks can appear and finally peel off the film if they progress, or otherwise dramatically reduce wear resistance. Thin buffer layers between substrate and film can be used to avoid this problem. Several transition metals and compounds can be used to this respect (W, Ta, TiC, Cr, SiC, etc.) depending on the substrate nature [Lee et al., 2000; Bahl et al., 2000; Kiuru et al., 2003].

With regard to surface properties, water contact angle has usually been examined providing relatively high values from 55° to 70°, depending on the presence of low energy C–H groups on the surface and the oxygen contamination of the film. The

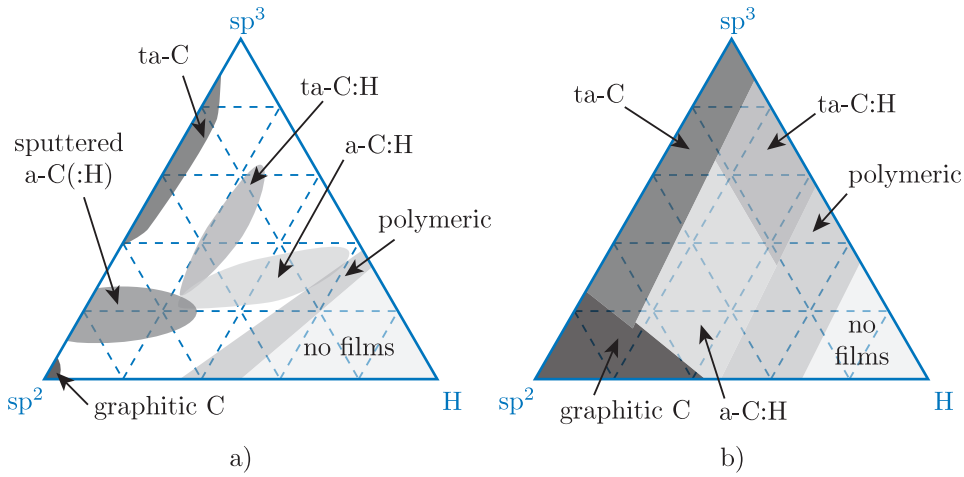

Figure 2.1.: Ternary diagrams of amorphous carbon types with respect to sp^2 and sp^3 fraction, and H content. a) by [Robertson, 2002]; b) by [Silva, 2003]

introduction of dopants like F, Fe, Al and others has proven to be a useful method for increasing contact angle values up to more than 100° [Grischke et al., 1995; Chen et al., 2001].

2.3 Applications

The best known and most wide spread commercial application field of DLC is in magnetic storage technology. For example, hard disks and read/write heads are coated with ultrathin DLC films to protect the magnetic media from corrosion. Due to the required short distance between head and disk, films must be thinner than 5 nm [Robertson, 2003; Goglia et al., 2001]. However, in order to obtain larger areal data density this distance must be further reduced. Compared to a-C:H films that fail to protect from corrosion when thinner than 3 nm, ta-C films deposited by FCVA show excellent corrosion and wear resistances for thicknesses down to 1 nm, whereas atomic smoothness (0.12 nm RMS) and absence of pin-holes ensure the quality of the coating [Casiraghi et al., 2004].

In tribological systems with separation of the two counterparts by an oil film, DLC coatings do not show improved performance. However, when lubrication is not complete (e.g.: due to stopping/starting, severe load conditions, or during temporary loss of lubricant) DLC and metal containing DLC coatings can significantly reduce wear [Gåhlin et al., 2001].

In the automotive industry, different parts coated with DLC have already been investigated and demonstrates the excellent performance of DLC coated car parts, for example gears [Vassell et al., 1997; Murakawa et al., 1999], valve lifters, camshafts,

Figure 2.2.: Left: WC/C multilayer (Balinit C®) coated spur gear from Balzers; Top right: Uncoated (left) and coated (right) piston pin from Katech Performance; Bottom right: DLC coated camshaft from Alpha Racing.

fuel injector parts or piston rings [Tung and Gao, 2003] (see figure 2.2). As of 2004, worldwide, more than half of the diesel fuel pumps and fuel injectors had critical parts coated with DLC [Hauert, 2004].

Also for injection molding, the anti-sticking properties of DLC result in a more durable mold and better product quality. Wear resistance of DLC protects the mold against abrasive particles used as additives in polymers. Moreover, anti-sticking properties (improved with different additives in DLC such as fluorine), provide good release characteristics that allow the reduction of the cycle time by 5%.

Diamond-like coatings have also been used by watch makers to reduce wear due to everyday use or by razor blades makers such as Gillette (Mach3®) and Wilkinson-Sword and Schick (FX-Diamond®) [Hauert, 2004].

DLC's high transparency in the IR range makes DLC films suitable for surface-protective applications in IR optics [Silva, 2003]. The company Morgan sells scratch resistant DLC coated AEGISGLASS® glass plates for laser barcode scanner window applications [Hauert, 2004].

For fluid transport, DLC coatings, and specially when modified to reduce its surface energy, are useful to improve surface properties of inner walls of pipes. The

coating of these geometries is possible by plasma-based ion immersion (PBII) applied with bipolar pulses [Miyagawa et al., 2002].

Finally, biocompatibility and antithrombogenicity of DLC films make them candidates for a number of medical applications where wear resistant coatings, such as prothesis, or simply biocompatible parts are required [Kiuru et al., 2003; Saikko et al., 2001; Loir et al., 2005; Saito et al., 2005].

2.4 Deposition techniques

As already stated, hard amorphous carbon thin films can be deposited by a number of deposition techniques. First deposited in 1971 by Aisenberg and Chabot with an ion beam, [Aisenberg and Chabot, 1971] it was soon after deposited by RF plasma enhanced CVD (PECVD) by Ojha and Holland [Ojha and Holland, 1977].

In 1990, Lifshitz et al. described the so called subplantation model by which a progressive densification of the film's sub-surface by penetration of energetic ions was produced, associated to the formation of metastable sp^3 sites [Lifshitz et al., 1990]. An energy of 100 eV was established as the optimum for high hardness a-C films, [Robertson, 1994b] although more recently studies have revealed that lower ion energy can produce equally high sp^3 fractions [Ferrari et al., 2002]. Ion energy is therefore an important parameter in amorphous carbon thin film growth, and specially for hard films. See section 2.5 for a more detailed explanation of the growth mechanism.

A summary of the characteristics of different deposition techniques follows.

2.4.1. Ion beam techniques

These were the first to be used for amorphous carbon deposition [Aisenberg and Chabot, 1971]. A graphite cathode in a plasma source or a hydrocarbon are used to generate the carbon species, which are later on accelerated towards the substrate [Spencer et al., 1976; Kaufman, 1978; Weissmantel et al., 1980; Mori and Namba, 1983].

A refinement of this technique is the mass selected ion beam. Carbon ions are produced in an ion source from a graphite target, accelerated from 5 to 40 kV and passed through a magnetic filter. This filters out any neutrals and selects ions with an e/m ratio of the C^+ ion. The ions are then decelerated to the desired ion energy by electrostatic lens, and the beam is focused onto the substrate in a vacuum of order 10^{-6} Pa to produce a ta-C film [Pouch and Alterovitz, 1990; Hofsäss et al., 1994; Lifshitz, 1996].

Useful only for research activity, MSIB provides a controllable deposition in species and energy but at the cost of very low deposition rate and complex setup.

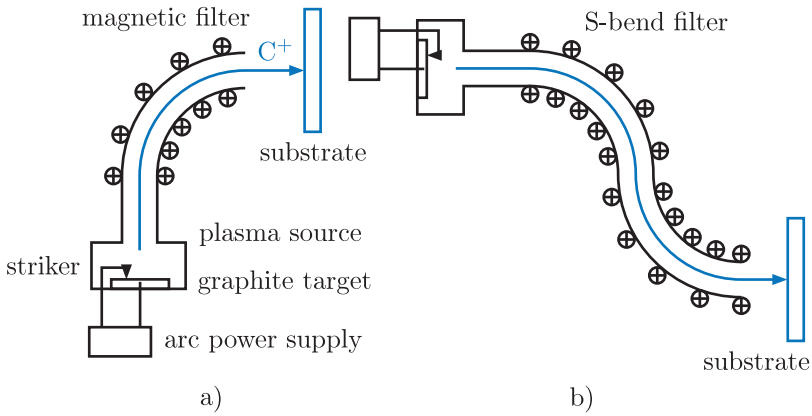

Figure 2.3.: Schematic of a (a) single bend and (b) double (S) bend FCVA. Extracted from [Robertson, 2002].

2.4.2. Cathodic arc

Cathodic arc techniques are unusual, although they have been used to deposit the hardest ta-C films with sp^3 fractions up to 90% [Polo et al., 2000]. An arc is initiated in high vacuum by touching the graphite cathode with a small carbon striker electrode and withdrawing the striker. This produces an energetic plasma with a high ion density of up to $10^{13}\,cm^{-3}$. Subsequent filtering (FCVA) with a magnetic field in a single or double bend eliminates particulates and neutrals, providing a highly ionized beam (see figure 2.3) [Aksenov et al., 1980; McKenzie et al., 1991; Fallon et al., 1993]. This technique can therefore be seen as part of the ion beam techniques. Ion energy is adjusted by biasing the substrate. FCVA has been used for some industrial applications.

2.4.3. Sputtering

This is the most common industrial process for DLC deposition together with PECVD. It is commonly used with either DC or RF power to sputter a graphite target by an Ar plasma. Magnetron sputtering heads are a must due to the low sputtering rate of graphite. In order to improve film's characteristics, DC bias can be applied to the substrate to modify ion energy and unbalanced magnetrons can provide additional ion bombardment to the film's surface. This technique is sometimes combined with Ar ion beams to bombard the growing film, densifying it and promoting sp^3 bonds [Savvides, 1984; Jansen et al., 1985; Cuomo et al., 1991].

Being simple, widespread and versatile, sputtering is an ideal technique for industrial processes. Its drawback, however, is the rather low ion density which prevents the deposition of the hardest DLC films.

2.4.4. PECVD

RF PECVD is the most widely used deposition technique for DLC films (see subsection 3.1.1 for technique description) [Holland and Ojha, 1976; Catherine and Couderc, 1986; Koidl et al., 1990; Bubenzer et al., 1983]. The main drawback of conventional PECVD is that it is not possible to have independent control of the ion current and the ion energy, as they both vary with the RF driving power. Workarounds to this issue involve the setup of some kind of plasma source or ion beam, such as inductively coupled plasmas (ICP) configurations or PBS and independent control of substrate bias [Weiler et al., 1996].

The feed gas has an important effect on the film's properties. Benzene, for example, due to its low ionization potential provides a high growth rate but due to the high number of C atoms per molecule, a high bias voltage is required to get the desired 100 eV per ion. Acetylene on the other hand has a comparable ionization potential, but only 200 V biases are required. Acetylene and methane are the most popular choices. The latter has higher ionization potential and therefore lower growth rate, but opposed to acetylene it is available in high purity form. Methane also provides more hydrogenated films [Robertson, 2002].

In this thesis, amorphous carbon thin films have been deposited using PECVD technology powered with bipolar pulsed-DC power at LF. Details about the experimental setup are available in section 3.1.

RF excitation provides rather inefficient ionization in the plasma, with plasma densities about $10^9\,\mathrm{cm}^{-3}$. In addition, the DC self-bias developed in the cathode of an RF-excited plasma depends on the surface ratio between anode and cathode (see subsection 3.1.1), which in practice imposes an upper limit of substrate surface, because chamber's (anode) volume grows faster than its area and pumping velocity depends on volume.

On the other hand, bipolar pulsed-DC does not have such limitation associated to RF excitation, so that big parts can be coated efficiently, using this technology. Moreover, time-resolved Langmuir probe experiments have shown that ion densities in plasmas excited with pulsed-DC power are at least twice as with RF. Regarding ion energy, the increased peak voltage for equal average power could provide more energetic ions depending on the pressure. [Corbella et al., 2005] This technique also provides films with lower intrinsic stress, due to the pulsed characteristic, and higher growing rates.

2.5 Growth mechanism

The main properties of pure DLC films are related to their sp^3 bonding. This characteristic is controlled by ion bombardment, energies about 100 eV providing the highest sp^3 fractions [McKenzie, 1996; Lifshitz, 1996, 1999]. In order to simplify, a first description for hydrogen free DLC films will be exposed.

Several explanations for the preferential sp^3 bonding with high energy ions have been proposed. Spencer et al. proposed various mechanisms such as the preferential sputtering of sp^2 sites from the sp^2 and sp^3 mixture [Spencer et al., 1976]. However, Lifshitz et al. noted that because of the low sputtering yield of carbon this mechanism would not work [Lifshitz et al., 1990]. Weissmantel suggested that the sp^3 bonding arose from a shock wave of the displacement spike of the ion cascade, but the shock wave is more appropriate to higher ion energies and masses [Weissmantel, 1982].

Later, Lifshitz et al. used Auger analysis of the depth profiles of medium energy C ions incident on Ni substrates to show that the growth was sub-substrate. They named this process "subplantation" (for low energy subsurface implantation). They proposed that the sp^3 sites accumulate by a preferential displacement of sp^2 sites to interstitial positions. This hypothesis arose from early estimates of the displacement threshold in graphite and diamond of 25 and 80 eV. However, after that direct measurements found similar values for graphite (35 eV) and diamond ($37 - 47$ eV), [Koike et al., 1992] so preferential displacement is not correct. Still, some authors keep taking the hypothesis to be correct, due to the anisotropic nature of sp^2 bonds [Banhart, 1999].

Some time later, McKenzie et al [McKenzie et al., 1991; McKenzie, 1993]. proposed that the role of the ion bombardment is to create a compressive stress in the film which would move it above the Berman-Simon line where diamond is the stable phase (see figure 2.4). Once the phase is created it is quenched into the growing film. Similarly, Robertson suggested that the ion bombardment creates a metastable increase of density that tends to change the local bonding to sp^3 [Robertson, 1993, 1994a]. Both models assume that although deposition is a non-equilibrium process, some parts of it can be described by thermodynamics.

Although there is a clear link between sp^3 bonding fraction and stress, recent reviews have questioned the requirement of high stress to obtain high sp^3 fraction [Ferrari et al., 2002]. Apparently, stress would be needed during growth, but not necessarily after. This conclusion was obtained after examining a wide set of different experiments where sp^3 fraction had always been determined by EELS. Certain techniques or post-treatments showed a reduced stress after deposition with small, if any, sp^3 to sp^2 conversion.

2.5.1. Hydrogenated amorphous carbon

In hydrogenated a-C, the deposition process becomes more complicated. Many processes take place, as shown in figure 2.5. As in a-C, the dependence of plasma-deposited films' properties on bias voltage (related to ion energy) indicates the critical role of ions. However, also neutrals contribute to growth, as the mass deposition rate exceeds that due to ions alone [Robertson, 2002]. Neutrals will be closed shell molecules such as undissociated precursor gas, radicals and significant amounts of atomic hydrogen.

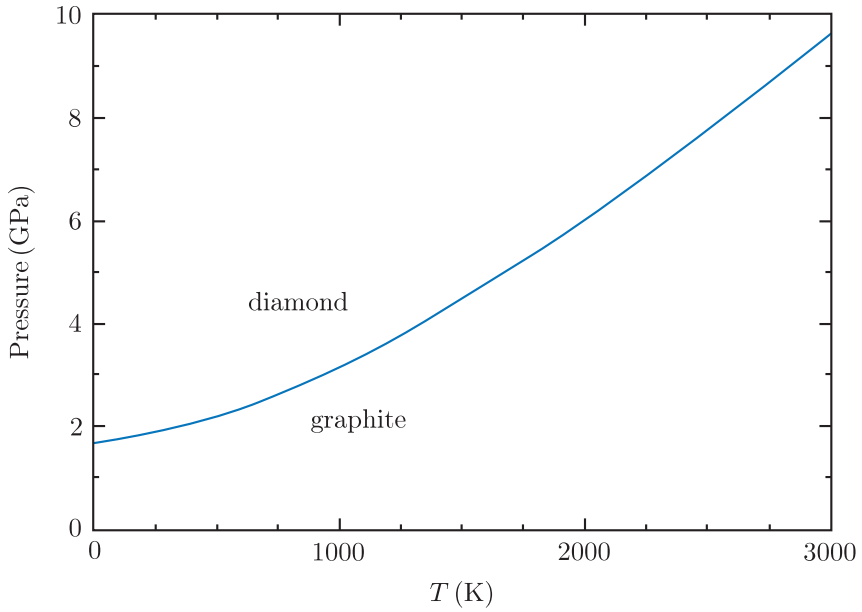

Figure 2.4.: Berman-Simon phase diagram for carbon. [Robertson, 2002]

It is also known, that the observed temperature dependence of growth rate is due to the etching effect of atomic hydrogen, which is more intense at higher temperatures. Growth itself is not temperature-dependent [von Keudell and Jacob, 1996; Kessels et al., 1998].

Unsaturated species and di-radicals (even neutral) can directly react with C–C and C–H bonds, so their sticking coefficient approaches 1. On the other hand, closed shell neutrals like CH_4 have very low sticking coefficient of under 10^{-4}. Mono-radicals have a moderate effect. They can only react with dangling bonds, which can be produced by ions displacing H from the bond or by abstraction of H by atomic H or other radicals. However, it has been found that atomic H is the most efficient species for abstraction (30 times faster than CH_3, for example) [von Keudell et al., 2001].

Neutral hydrocarbons can only react at the surface, they cannot penetrate the film. However, both ions and atomic hydrogen can penetrate the film. Neutral H atoms, being so small, can thermally penetrate about 2 nm into the film (ions would penetrate even more) [Schwarz-Selinger et al., 2001]. Once there, H can also create subsurface dangling bonds or absorb H to create H_2.

The rest of ions can also penetrate the film. Specifically, carbon and hydrocarbon ions can cause subplantation, which ultimately increases sp^3 fraction, or also displace

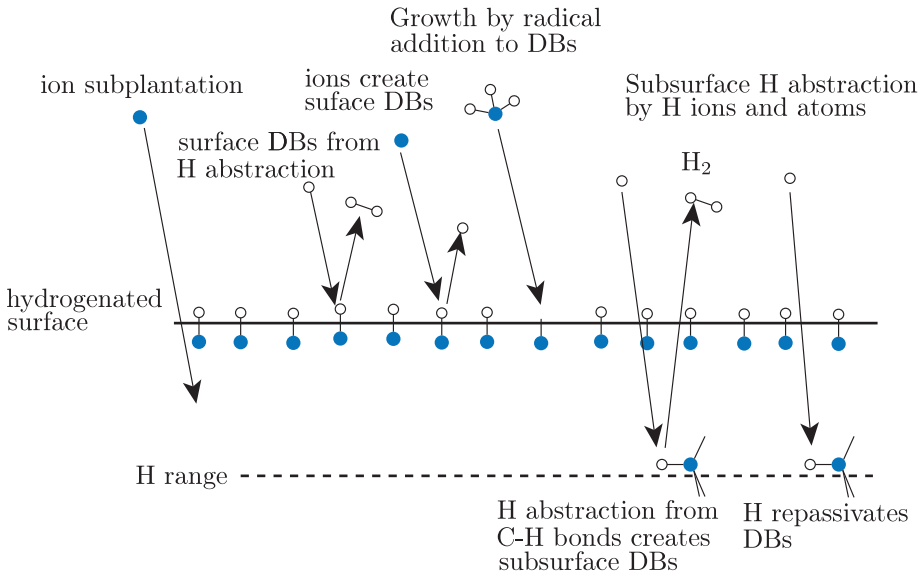

Figure 2.5.: Component processes in the growth mechanism of a-C:H. Dangling bonds are abbreviated DBs. [Robertson, 2002]

H which would then recombine with other H atoms. This would be the main cause of hydrogen reduction with increasing bias voltage [Robertson, 2002].

According to Schwarz-Selinger, a-C:H films have three characteristic depths: the surface itself, controlled by reactions of hydrocarbon and hydrogen species; the upper 2 nm in which chemistry is controlled by reactions of atomic H, and a larger depth, depending on ion energy, in which reactions are controlled by H^+ ion [Schwarz-Selinger et al., 2001].

2.6 Fluorinated amorphous carbon

The introduction of alloying elements in amorphous carbon thin films has been used for a long time to improve specific properties of the films depending on the aimed application. Some of the most studied modifications include the reduction of internal compressive stress with N, Si or metal incorporation, surface energy with F and some metals, friction coefficient with F and Si–O, or the modification of the electrical properties. Metal-containing films are probably the most known modification for mechanical applications where hardness and friction are specially important. Metals like Ta, W and Nb reduce films' intrinsic compressive stress while wear resistance and friction do not suffer an important reduction if the content is low. [Grischke et al., 1995]

Also surface properties are modified with metals incorporation. Al, Fe, Ni, Nb and Ti, for example, reduce surface free energy (SFE or γ_s) with water contact angle values up to 102° for Al-containing films and γ_s as low as $22\,\mathrm{mJ/m^2}$, while, on the other hand, W slightly increases SFE. [Chen et al., 2001; Zhang et al., 2004; Corbella et al., 2004b] In addition to metals, the introduction of Si, O, N or F in a-C films has been investigated, too. In this case, O and N increase SFE, while Si and F reduce it. Interestingly, addition of both Si and O can reduce the SFE more than only with Si. [Grischke et al., 1995] Among these elements, fluorine incorporation exhibits the highest water contact angles (more than 100°) and lowest surface energies (about $20\,\mathrm{mJ/m^2}$).

A number of studies regarding the introduction of F in DLC films can be found in the literature. However, one must distinguish between growing fluorinated films and fluorinating films or other surfaces. The former corresponds to the growth of films containing fluorine in bulk, while the latter only adds fluorine functionalization to the surface.

Fluorination of surfaces is easily achieved by etching with common fluorocarbon plasmas. This consequence has sometimes been seen as an adverse effect and cleaning procedures have been designed to remove fluorinated groups from the surface. [Simko et al., 1991] Others, have intentionally used fluorocarbon plasmas to functionalize surfaces. [Miyamoto et al., 1991; Korotkov et al., 2007; Roy et al., 2007]

The advantage of growing fluorinated films is that even after being worn out to some extent, the new surface preserves bulk's chemical composition. In addition, fluorine does not only change surface properties but also provides interesting bulk properties. Fluorinated amorphous carbon has been extensively studied as a low dielectric constant (low-κ) material for electronic devices where parasitic capacitance must be avoided, because it can be deposited with microelectronic compatible methods. Static dielectric constant values as low as 2.1 have been obtained by RF-PECVD with CH_4 and CF_4, with increasing ε_r with RF power. [Endo and Tatsumi, 1995] As a comparison, the traditional dielectric layer in microelectronics, SiO_2, has $\varepsilon_r = 4.0$ and current dielectrics used in 90 nm, 65 nm and 40 nm lines of Intel® processors have $\varepsilon_r = 3.0$. [Grill, 1999]

The other major property of fluorinated amorphous carbon is its reduced surface energy. Compared to Si, fluorine not only reduces its polar component but also the dispersive contribution. The introduction of fluorine in the film displaces hydrogen, and bigger $-CF_2$ and $-CF_3$ groups are formed. This reduces the network density therefore reducing the dispersive component. [Grischke et al., 1995] When the appropriate growing conditions are used, low surface energy coatings ($20\,\mathrm{mJ/m^2}$) with improved hardness (5 to 20 GPa) over PTFE ($18\,\mathrm{mJ/m^2}$ and 0.3 GPa) can be obtained. These conditions are reported to fall into the moderate fluorination conditions ($R_F^{film} \equiv [\mathrm{F}]/([\mathrm{F}]+[\mathrm{C}]) < 0.2$). [Donnet, 1998]

The deposition process of fluorinated a-C films is usually performed by PECVD although sputtering has also been used in some studies. The deposition by sputtering can be performed in reactive mode by using a graphite target and some fluorocarbon

gas (e.g. CF_4, CHF_3, etc.), [Trippe et al., 2004; Jiang and Ning, 2006; Guerino et al., 2007] or by directly sputtering a PTFE target. [Gonon and Sylvestre, 2002; Tang et al., 2005]

More work can be found in the literature about PECVD. There is a number of possible precursors with different C:F ratio which can be used to deposit fluorinated amorphous carbon. As reported, the film fluorine content is primarily determined by the gas precursor chemistry. Generally, more fluorine in the process gas results in higher fluorine concentration in the film; adding hydrogen to the feed gas reduces the film F:C ratio. [Mountsier and Samuels, 1998] CF_4 is one of the highest F:C ratio precursors available. Combined with CH_4, it is reported to produce lower dielectric constant than other precursors, and Vicker's hardness values from 5 GPa to 10 GPa [Jacobsohn et al., 2000]. Other studies, show results for the same gases with hardness values from 16 GPa to 19 GPa and surface free energy values descending from 40 mJ/m^2 for films deposited from pure CH_4 to about 28 mJ/m^2 for 4:1 CF_4 : CH_4 gas flow ratio. [Yu et al., 2003]

On the other hand, the gas used in this thesis (CHF_3) has barely been studied for PECVD processes. Only a few papers, concerning deposition of low-κ dielectrics, can be found in the literature and diamond-like properties have virtually not been sought with this precursor. Among them, a paper from Winder and Gleason shows lower roughness values and higher fluorine incorporation for films deposited from CHF_3 than $C_2H_2F_4$ or CH_2F_2 [Winder and Gleason, 2000]. Y. Xin et al. have also published work about growth of a-C:F:H films deposited with CHF_3 and using ECWR-PECVD. Neither the mechanical properties nor the surface energy of the films were examined. [Xin et al., 2003]

However, more work can be found dealing with the use of CHF_3 as precursor for plasma treatments, including treatments of previously grown DLC films. [Kawasaki et al., 2004] Schvartzman and Wind make use the modified DLC for NIL molds, as sought in this thesis, and show slightly lower surface free energy values for surfaces treated with CHF_3 than C_4F_8. [Schvartzman and Wind, 2009]

The use of Si substrates and fluorinated gases presented a problem during the first stage of this thesis, because F-containing plasmas easily etch Si. To change the etching behavior to growth, some authors suggest to increase of gas pressure. [Kawasaki et al., 2004] Here, a pure a-C layer with known good adhesion to Si from previous studies, [Corbella et al., 2004a] was used as inert buffer for the subsequent growth of the film, so that F could not react with Si. In this case, the buffer layer was not aimed to improve adhesion but to allow the growth itself.

Part II.

Experimental device

3

Deposition and fabrication techniques

As described in the Preface, the main objectives of this thesis are:

- The deposition and characterization of fluorinated amorphous carbon films
- The production of nanostructures on silicon for mold fabrication
- The exploration of mold coating with a-C for durability and anti-sticking purposes

In order to achieve these goals, several experimental devices have been used. The reactor for deposition and etching has been completely designed and set up during this thesis.

In this chapter, the main features of the reactor are exposed, along with a brief introduction to the deposition and fabrication techniques used for the thesis' objectives: plasma enhanced chemical vapor deposition (PECVD), for deposition of a-C films; electron beam lithography (EBL), for pattern definition; and reactive ion etching (RIE) and ion beam etching (IBE), for the pattern transfer and production of nanostructures on silicon. Of these three, EBL and RIE have been used in the research group for the first time during this thesis. In addition, pulsed-DC PECVD is a novel technique for fluorinated a-C films.

3.1 Deposition and ion etching reactor

During the course of this thesis, a reactor capable of performing several of the needed processes has been engineered and constructed. The older available reactors in the group, although capable of achieving low base pressures of 10^{-3} Pa, presented important tightness problems, specially regarding the water cooling circuits of the sputtering and PECVD heads. Therefore, the design of the new reactor was focused on the use as many copper sealings as possible. The number of elastomeric seals was reduced to the minimum, only for the mobile elements, valves, gates and movement feedthroughs. Once assembled, the reactor was checked for leaks by using helium detection systems and optical emission spectroscopy of plasmas, very sensitive to small quantities of nitrogen.

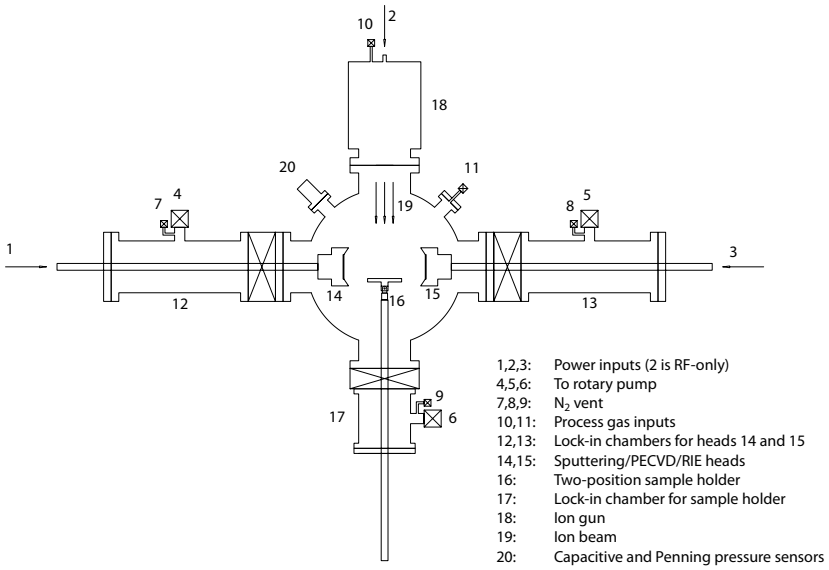

Figure 3.1.: Reactor. Several techniques can be used, including sputtering, PECVD, RIE or IBE.

Besides tightness, versatility has been taken into account in the design, so that a number of techniques are available:

- Magnetron sputtering, which has been used for DLC [Rubio-Roy et al., 2007, 2008b] and Permalloy [Olziersky et al., 2009] growth.
- Plasma enhanced chemical vapour deposition (PECVD), used through this thesis [Rubio-Roy et al., 2008a, 2009].
- Ion beam etching (IBE), used through this thesis [Portal et al., 2009] and for patterning of superconductor materials.
- Reactive ion etching (RIE), used through this thesis.

The reactor consists in a 304 stainless steel spherical chamber capable of reaching very high vacuum (10^{-5} Pa) whose gas feeds and vacuum system are fully computer controlled with RS-232 interfaces and through a digital output card (see figures 3.1 and 3.2). As previously described, the seals are mainly of ISO-CF type (copper) and the chamber is pumped by a LEYBOLD TMP360C turbomolecular pump backed by one of two LEYBOLD TRIVAC rotary pumps, the selection of which depends on the pumped products: combustibles or comburents. The gas feeds consist of six different lines each one equipped with pneumatic valves and mass flow controllers (MFC) which introduce the gases in the chamber.

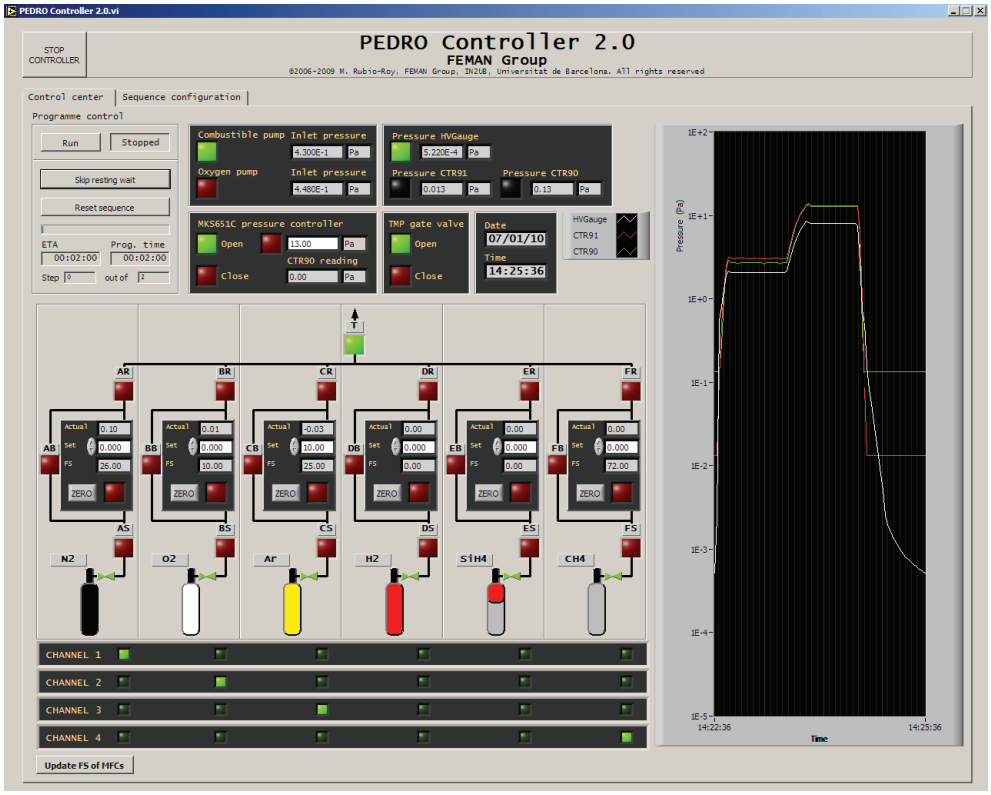

(*a*)

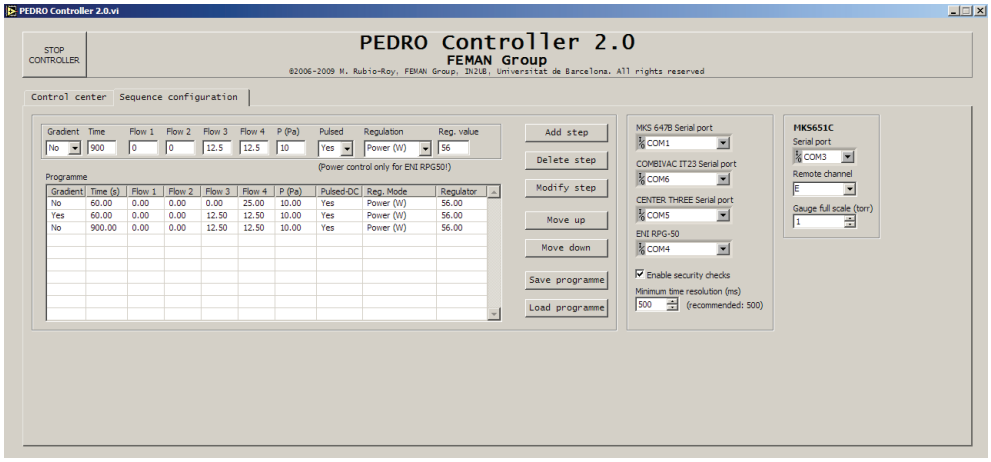

(*b*)

Figure 3.2.: Graphical user interface of the reactor controller. (a) Main process and control view; (b) Configuration view.

Three load-lock chambers are connected to the main spherical chamber. Two of them are used for entering water-cooled cathodes (for magnetron sputtering, PECVD or RIE) while the other is used to enter miscellaneous sample holder. Different sample holders can be used depending on the application (heated, multi-sample or for ion beam etching). Moreover, an ion source is located in front of the sample holder.

The water-cooled PECVD sample holder, used throughout this thesis for the deposition of fluorinated DLC films, was also redesigned and built in order to assure its complete tightness and durability, and incorporated all the experience of the more than twenty years of experience with plasmas of the research group. The PECVD head consists on a cathode partially shielded by a grounded anode which avoids the formation of plasma in the covered cathode-surfaces. This way, the effective cathode surface is reduced to a circle of 3" in diameter, concentrating the power and forcing a more uniform distribution of the electrical field in the cathode sheath. A water flow is maintained through the circuit in order to dissipate the heat generated at the cathode by the impingement of ions and power transmission losses.

The reactor controller software was designed with LabView. It has two tabs: the "Control center" and the "Sequence configuration tab" (figure 3.2, a and b, respectively). The software can operate in two modes: manual or automatic. In the former, the following elements can be controlled as desired at any time:

- Bottle-side, bypass and reactor-side valves of the six different gas lines available
- Valve for the cold cathode pressure gauge
- Main valve between turbomolecular pump and chamber
- Valves between turbomolecular pump and backing pumps
- Butterfly valve: fixed position or pressure regulation
- MFCs' setpoint, on/off state and zero adjustment

In addition, all pressure and flow readings are available all time and updated every two seconds:

- Full scale of the MFCs and actual flow
- Valve open/closed state
- Pressure in the chamber (two capacitive gauges with full scale of 133 Pa and 13 Pa plus one full range Pirani + cold cathode for down to 10^{-6} Pa) with numeric displays and a graphic plot of time evolution
- Pressure in the entry port of both backing pumps

Manual mode includes a security switch in the "Sequence configuration" tab (figure 3.2b) that watches over bad operation of the reactor by disabling certain actions:

- Open the bottle-side valve of a gas that could damage the cold cathode if its valve is opened
- Open the cold cathode valve if the bottle-side valve of any harmful gas is opened
- Open the bypass valve of any line if the bottle-side valve is also opened
- Entering combustible gases when pumping with the comburent pump and vice versa.

On the same tab, a programme can be defined, or saved or loaded to/from a file. When automatic mode is started, the programme is run. Every step of the programme defines the flow setpoint for every MFC, the pressure setpoint for the butterfly valve, the duration of the step and the state of the pulsed-DC power supply. In addition, every step has a "Gradient" switch. When on, flow setpoints are changed in the MFC linearly from the initial value to the defined setpoint. With this feature, layers with varying mixtures of different gases can carried out. In this thesis, the change from buffer layer to the actual film was done this way.

3.1.1. Plasma enhanced chemical vapor deposition

PECVD is an evolution over CVD processes, in which a thermally activated set of gas-phase and surface reactions produce a solid product at a surface [Lieberman and Lichtenberg, 1994]. In PECVD, both types of reactions are controlled by the plasma properties, because electron impact dissociation of the feed gas is possible for the typical energies ($T_e = 2 - 3\,\mathrm{eV}$) of electrons in a low-pressure discharge. Film precursors are generated in the plasma bulk, as dissociated species, and then condense onto the substrate. Although deposition rate is not heavily substrate-temperature dependant, film properties such as composition, stress, morphology or crystalline structure generally do, so that low temperatures (< 250℃) are typically used. Due to this particularity, most of the materials deposited with this technology are amorphous.

The type of electrical signal used to excite the plasma determines its electronic and ionic characteristics, which in turn, influence film's properties. Moreover, it can also determine the type of materials that can be deposited. For insulating films, if the film is intended to grow on the cathode, an alternating signal must be provided so that electrical charge in the film does not limit deposition process. Several signals of this kind can be used, each one producing different results: RF, pulsed RF, pulsed DC, MW, etc.

As in etching processes, different coupling configurations can be used. In figure 3.3 two RF driven configurations are shown. The advantage of using inductive coupling such as that shown in figure 3.3b, is that independent control of plasma ionization (dependent on signal power) and sample bias voltage is possible.

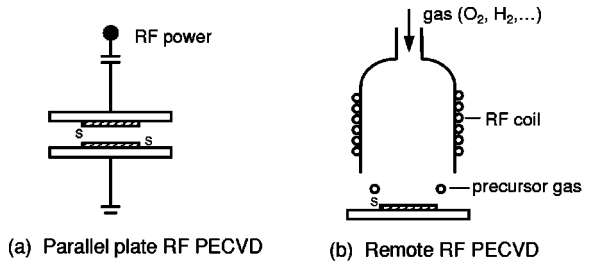

Figure 3.3.: Schematic illustration of different types of high frequency plasma systems for PECVD of optical films: (a) asymmetric capacitively coupled RF plasma; (b) remote plasma RF reactor. Extracted from [Martinu and Poitras, 2000]

In the most common RF plasmas, electrons, as opposed to ions, are able to follow the electric field due to their high mobility (the electronic plasma frequency is much higher than 13.56 MHz). For this reason, the regions close to the electrodes end up developing a positive spacial charge (more ions than electrons) called plasma sheath. In addition, in this region there is an electric field pointing towards the electrode. The rest of the plasma volume is at a constant positive voltage. The voltage drop from the plasma to the electrodes is called the self-bias.

In capacitively-coupled configurations, such as that shown in figure 3.3a, the difference in electrode areas A_1 and A_2 implies sheath voltages V_1 and V_2 on the electrodes that follow:

$$\frac{V_1}{V_2} \approx \left(\frac{A_2}{A_1}\right)^q$$

with q around 2.5 [Lieberman and Lichtenberg, 1994]. In order to maximise cathodic voltage, process chamber walls are grounded and are considered anode. In a discharge between two electrodes of different area, the difference of sheath voltages justifies why the depositing film is subjected to a more intense ion bombardment when placed on the cathode.

The basic steps in any CVD process have been summarised in the following list by [Ohring, 2002]:

(a) Transport of the reactants from the gas inlets to the reaction zone.

(b) Reactions in vapour-phase that form the gas precursors of the film and by-products.

(c) Transport of the reactants and their products from the gas phase to the substrate.

(d) Adsorption of these species on the substrate surface.

(e) Surface diffusion, chemical reactions and incorporation of these species on different growth sites.

(f) Desorption of the volatile by-products of surface reactions.

(g) Transport of the by-products away from the reaction zone.

Pulsed-DC PECVD

Throughout this thesis, asymmetric bipolar pulsed-DC PECVD at LF (see figure 3.4) has been used to deposit FDLC films. Pulsed-DC at LF presents some advantages over the more extended RF technique [Andújar et al., 2003]. From an industrial point of view, pulsed-DC is a cheaper alternative to RF and some studies point out to reduced plasma sheaths that allow better coating of holes [Michler et al., 1998]. On the other hand, this technique has shown an increase in deposition rate and a reduction of intrinsic stress, the latter being due to the changing polarity (bipolar characteristic) of cathode bias. This characteristic of the signal enables stabilization of the film during the positive period of each cycle (τ_+), while for RF this voltage is always negative. In addition, with respect to RF, pulsed-DC at LF also has the advantage of providing more energetic ions to the cathode. Although for equal power, mean cathode voltage is roughly the same for both signals, peak voltage is higher for pulsed-DC than for RF.

The use of this technique for film deposition has made use of the previous experience in the research group with it. The deposition of the films has been done by keeping the negative peak voltage at $-1000\,\mathrm{V}$, which represents an approximate power of $1.3\,\mathrm{W/cm^2}$ at $10\,\mathrm{Pa}$. These conditions had previously been observed to produce DLC films with average characteristics [Corbella et al., 2005]. The precursor has been varied from pure methane to pure trifluoromethane, to study the effects of the progressive fluorination of the films. A buffer layer deposited with the same power excitation but with pure methane was found to be adequate to avoid the etching action of fluorine atoms and species on silicon.

3.1.2. Ion etching

Ion etching or dry etching is an engraving technique which uses accelerated ions to remove material from the target. When inert ions are used, the material is etched by transferring enough momentum to the atoms and mechanically extracting them from the crystalline or amorphous network. This process is called sputtering, and occurs when impinging atoms have an appropriate energy [Rossnagel, 2003]. The impact of an energetic particle in the target dislodges, by momentum transfer, one or more atoms of the surface or next to it. These atoms, that have received a considerable amount or kinetic energy from the initial particle, penetrate into the target and dislodge other atoms. The process continues until the remaining kinetic energy is insufficient to dislodge more atoms. At that moment, the remaining energy is absorbed as phonons and the temperature raises locally. During all this process,

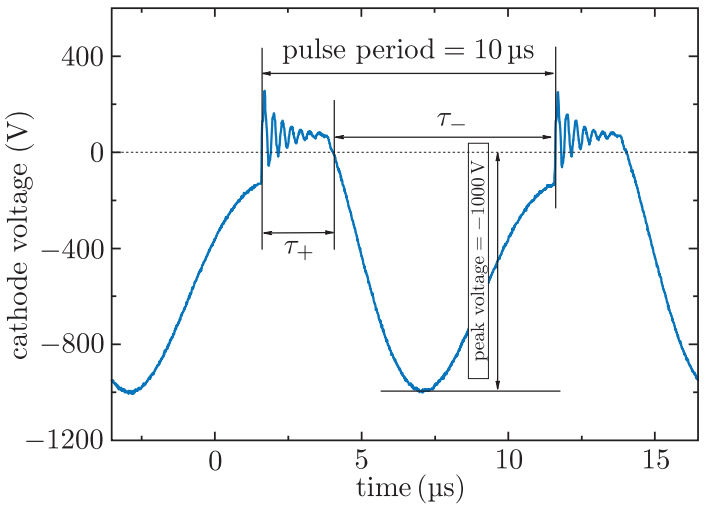

Figure 3.4.: Asymmetric bipolar pulsed-DC waveform in a 10 Pa CH_4 discharge at 100 kHz with a positive pulse time (τ_+) of 2016 ns and −1000 V of peak voltage. Extracted from [Corbella, 2006]

atoms at the surface may have been dislodged with sufficient energy so that surface binding energy is overcome and atoms are emitted from the target.

Mass and energy of incident particles determines collision process (see figure 3.5). For very low energies, particles are not able to dislodge too many atoms. For higher energies, between 50 and 2000 eV, particles follow the process described in the former paragraph and target is sputtered. This is the so-called knock-on or collisional sputtering range and is the most used for thin film work (PVD or ion etching). For even higher energies, between 2 and 50 keV, the incident particle forms a collision cascade near the impact point which breaks all the bonds of a vast number of atoms and can numerically be treated almost as a very dense gas [Rossnagel, 2003]. At energies above 50 keV, incident particles move deep into the target before depositing its energy. Little energy in present in the surface and sputtering yield drops significantly so that the process is better described as ion implantation.

When chemically active species are used in a plasma, the etching process is a combination of the physical sputtering and the chemical action of the species. Physical sputtering only relies on the momentum transfer of the impinging atom on the target. Although differences in sputtering yield exist between materials, due to the different cohesion forces of the materials, etching rates are roughly the same. However, when chemically active species are used, big differences in reactivity can be observed so that etching rate depends strongly on the chemical composition of target and ions.

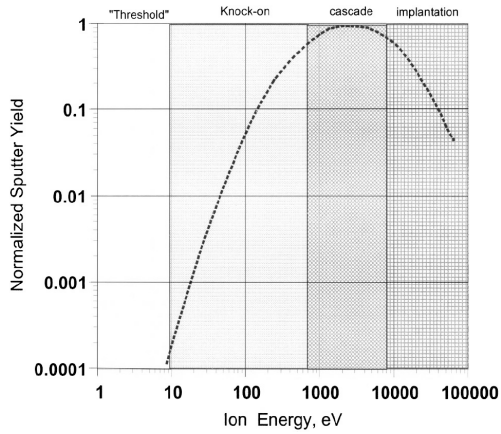

Figure 3.5.: Physical sputtering regimes for different energies. Extracted from [Rossnagel, 2003].

A parameter usually referred when characterizing an etching process is selectivity, defined as the etching rates ratio between two different materials. This is very useful, as etching processes are commonly carried out after having masked some parts of the samples in order to protect them, so differences in etching rate between mask and target surface are of interest.

Another attribute of etching processes is the isotropic or anisotropic characteristic. Physical sputtering is perfectly anisotropic. As etching relies on momentum transfer, engraving is only produced in the direction of ion impact. On the other side, chemical etching is possible in any direction, as it only relies on reactions between the species and the material. The latter is therefore isotropic although when chemically active ions are accelerated towards the target, a certain degree of anisotropy is achieved.

To sum up, four different processes can be considered to take part of a dry etching process (see figure 3.6):

(a) Sputtering
The etching is obtained by the momentum exchange between the incident ions with the target material surface. This process is anisotropic (it is only produced in the ion movement direction) and not selective (etching rate for different materials is similar). In general, the sputtered species are not volatile and can occasionally be redeposited. Contamination of the surface is rare.

(b) Chemical etching
The etching is produced by the chemical reaction of ions with material, the production of volatile products and finally their elimination by the vacuum system of the reactor. Through an accurate choice of the process gas, high selectivities can be obtained. The etching is isotropic.

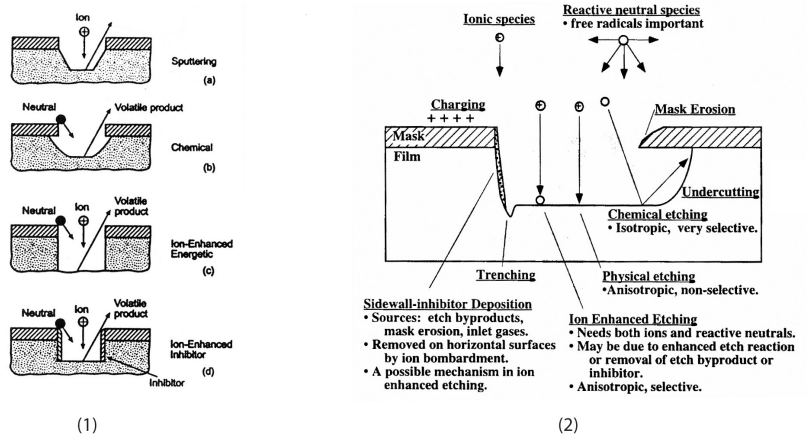

Figure 3.6.: Etching processes. (1) As explained on the previous page (3.1.2). From *"Plasma Etching"* p. 93 (1989), (2) Summary of processes.

(c) Reactive ion assisted etching
Combined process where both physical sputtering and chemical etching happen. Its effect is not the sum of both. Some mechanisms to explain this are found in the literature [Tu et al., 1981; Coburn and Winters, 1979]: defect creation in the surface of the material that could lead to spontaneous dissociative chemisorption, ion-impact-induced dissociation of molecules, non-volatile residues elimination or energy supply to surface that would promote molecule dissociation and subsequent reaction.

(d) Ion-inhibitor etching
A step forward from reactive ion assisted etching. A mixture of gases is chosen so that an inhibitor reacts with freshly etched material and protects it from further etching. In the regions where physical sputtering is happening, the inhibitor protecting layer is removed and etching progresses.
Oxidation frequently produces an involatile oxide which remains upon the surface while a similar interaction with halogens often yields a volatile product (e.g., SiF_4 for Si and F), which is subsequently desorbed into the gas phase. The oxidation reaction is inhibited by the involatile oxide layer while fluorination (for example) may continue indefinitely because the products are desorbed. [Winters et al., 1983]
This technique is useful for high aspect ratio profiles and frequently results in surfaces passivated with the radicals contained in the plasma.

Reactive silicon etching

In order to fabricate nanostructures, and eventually coat them with an a-C film, some material must be etched. Because of the compressive stress associated for DLC films not all substrate materials are adequate. When deposited with pulsed-DC PECVD of methane the films adhere to silicon without further buffer layers. Also, most nanoimprint molds are made of silicon because of the wide scientific experience on silicon etching. For these reasons, silicon was chosen as substrate for mold fabrication and fluorinated a-C deposition. Instead of etching silicon and depositing a-C, another option is the deposition of a thick film and the subsequent etching with O_2 plasma [Altun et al., 2006]. However, this alternative presents a number of problems. Although experimentally easier, oxygen etching would probably change the surface functionality of the film, with high energy groups and increase roughness. Moreover, silicon etching has been refined to allow the obtention of vertical walls with high aspect ratios, while for oxygen etching of carbon this has not been so studied. In this thesis, the first approach (first etch silicon, then deposit FDLC) has been used.

Fluorine interaction with solid silicon to form SiF_4 (gas) is one of the best understood examples of etching from a surface science point of view. This is mostly due to the importance of this material and their machining processes in the electronic industry. Nevertheless, surfaces in a plasma etching environment are complex from a chemical point of view. For example, it is widely believed that fluorine atoms cause the etching of silicon in a glow discharge generated in a fluorocarbon gas. This belief is undoubtedly correct when F atoms are the most abundant radical in the gas phase. However, when CF_x or CF_x^+ are also present in the gas phase, these species are also expected to contribute fluorine to the etching reaction. In other words, the fluorine which leaves the surface as part of an SiF_4 molecule may have originally reacted with the surface in the form of CF_x, CF_x^+ or F [Winters et al., 1983].

The etching process used for Si surface nanostructuration in this thesis is an implementation of the ion-inhibitor etching processes. In such processes, different products are provided to the plasma: a chemical etchant to react with the substrate, a passivator to block the etching of the sidewalls and an ion source for the local removal of the passivation layer at the bottom of the etching trenches. When these processes are controlled in the correct manner, it is possible to create all kinds of trenches with excellent profile control, high etching rates and selectivity.

The low-toxic and easy-to-handle SF_6, CHF_3, O_2 gases have been chosen in this thesis for the reactive ion etching of silicon. In such plasma, SF_6 produces F^- radicals for the chemical etching of Si, forming SiF_4; O_2 creates the O^- radicals to passivate Si surface and avoid sidewall etching by forming a SiO_xF_y protective layer; and CHF_3 is the source of CF_x^+ ions that etch the SiO_xF_y layer in one direction, forming CO_xF_y (see figure 3.7). SF_x^+ ions also participate of directional etching of protective layer but as SF_6 flow is fixed on the O_2 flow, so that vertical walls regime is achieved, CHF_3 is a nearly independent source of oxyfluoride-etching ions [Jansen et al., 1995].

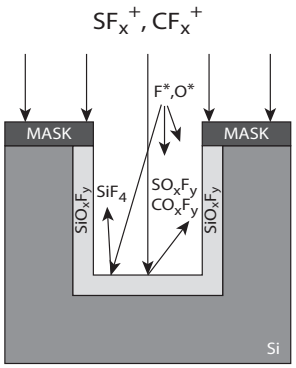

Figure 3.7.: The SF_6, CHF_3, O_2 chemistry. Extracted from [Jansen et al., 1995]

Although vertical walls regime can be found without the need of CHF_3 addition, surface roughness (grass or micrograss as usually referred in the literature) is usually observed when the other two gases are used alone. This could be due to the formation of micromasks from SiO_2 mask or from particulate generation from Si and subsequent oxidation with O_2. The addition of CHF_3 results in a lower roughness, probably by removing silicon dioxide from the horizontal surfaces [Legtenberg et al., 1995].

With regard to mask material, metals show higher selectivities to Si (hundreds, depending on the metal) compared to SiO_2 (between 4 and 5 for our experiments). However, some materials can act as catalyst for SF_6 to generate fluorine, which is not desirable.

In this thesis, both aluminum and silicon dioxide have been used as masks. The former was patterned with a lift-off process, whereas the latter was etched in a pure CHF_3 plasma. Conditions for this plasma were optimized for the mask thickness and are described in the results part.

Finally, cathode material has an important role in etching processes. For Si etching, a silicon cathode, or Si loading, is necessary in order to achieve a higher uniformity along it. For this reason, the entire cathode area has been covered with a 3" in diameter crystalline Si wafer, which in addition removed Al micromasking effects, described in 6.1.1, caused by the aluminium cathode.

Ion beam etching

For direction-controlled physical sputtering, an ion source HFQ1303-3 from Plasma Consult has been used. The ion source is filamentless and capacitively coupled to the RF power generator. The anode/cathode setup is axial, with the latter in the center of the source, as depicted in figure 3.8a.

An extraction system composed of two grids in one side of the source, provides a way to select the ion energy and control the divergence of the beam. Different types

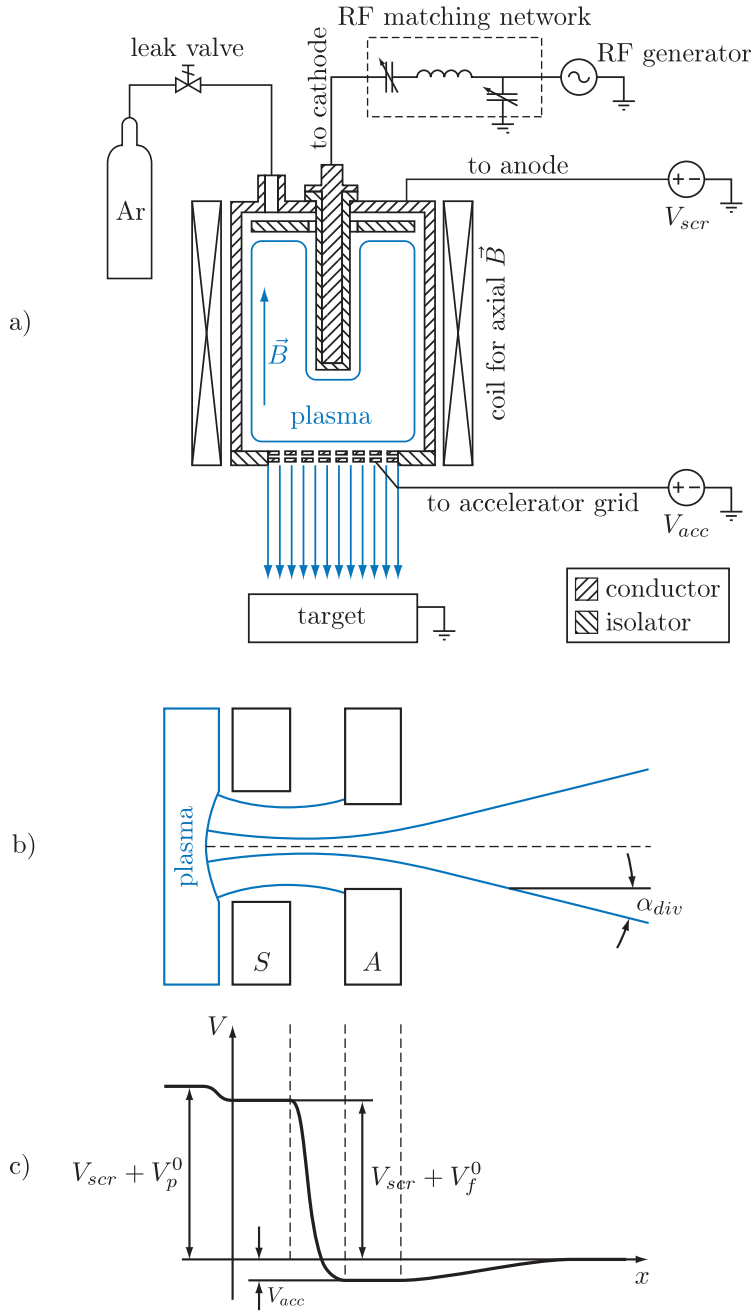

Figure 3.8.: (a) HFQ1303-3 ion source schematics; (b) ion beamlet from plasma and through screen and accelerator grid to vacuum; (c) Potentials through the grids. V_{scr}, V_{acc}, V_p^0 and V_f^0 are the screen, accelerator, plasma and floating potentials, respectively. The plasma and floating potentials are referred to the anode.

of extraction systems can be installed in this ion source, depending on the number of grids and their material. Standard extraction systems are made of silicon, stainless steel, molybdenum or graphite. Each of them is suitable for different conditions, depending on the feed gas or ion energy.

A coil around the anode produces an axial magnetic field in the plasma chamber that leads to a reduction in the diffusion constants for directions orthogonal to the magnetic field. This way, recombination losses on the cylinder walls are minimized. On the other hand, electrons move on cycloidal trajectories that increase ionization. The generated magnetic field is 4.4 mT/A with a maximum current for continuous operation of 8.5 A (with water cooling working). All the system is controlled by: RF power (P), screen and accelerator potentials (V_{scr} and V_{acc}) and coil's current (I_B).

As shown in figure 3.8a, the screen grid (closer to the plasma than the accelerator grid) is electrically isolated, so it acquires the floating potential corresponding to the particular plasma conditions. This potential is commonly close to the plasma potential. The screen potential is applied to the anode.

From figure 3.8c, follows that the ion energy is $V_{scr} + V_p^0$, where V_p^0 is the plasma potential referred to the anode. The additional energy provided by the accelerator grid to the ions is lost while traveling to the grounded target. This grid is aimed at reducing the divergence of the ion beam (see figure 3.8b for a diagram of a beamlet).

As opposed to other ion sources, the set up of this provides an ion-only beam, as electrons are confined by the strong potential decay after the screen grid.

3.2 Electron beam lithography

Electron Beam Lithography (EBL) is a lithographic technique based on the sensitivity of certain polymers (resists) to electron exposure [Owen, 1985; Rai-Choudhury, 1997]. Compared to optical lithography, where energetic electromagnetic radiation (typically UV down to 193 nm) is used, diffraction limit in electron systems is much far away, due to the shorter wavelength $\lambda \leq 0.1$ nm of electrons ($10 - 50$ keV). In fact, nowadays, EBL resolution is not limited by diffraction effects but by virtual diameter of electron source, focusing power of condenser lens, instrumental aberrations or dispersion of electrons inside the resist.

In contrast with Electron Projection Lithography (EPL), where a wide electron beam is masked and projected to the resist, EBL relies on a narrow beam which is scanned over the resist surface. EBL is therefore much slower than EPL but allows the users to easily modify the pattern, while EPL needs a different physical mask for each one.

EBL has been one of the techniques used to define the mask for the subsequent etching step in the nanostructuration of silicon procedure. Other techniques have also been used, such as colloidal lithography [Portal et al., 2009]. However, EBL does not have any inherent limitation for pattern design.

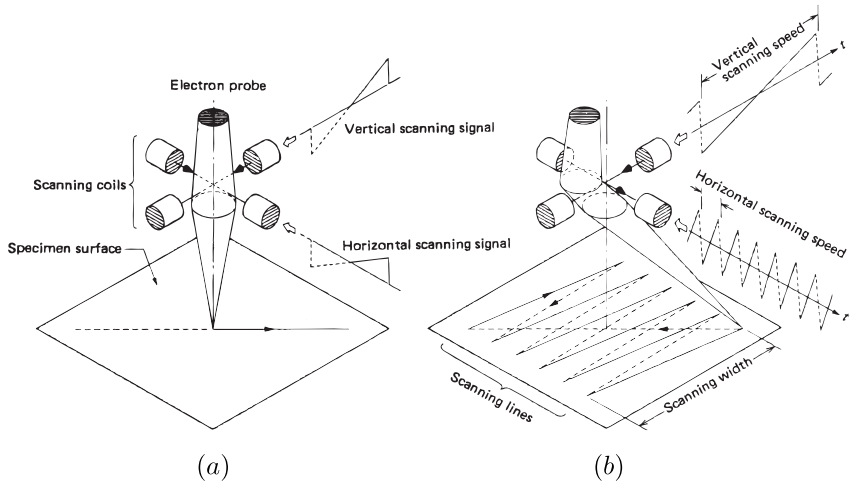

Figure 3.9.: Examples of signals and their produced scan. (a) Diagonal scan; (b) Square area scan. From JEOL JSM-840 User Manual.

The scanning nature of EBL permitted the use of Scanning Electron Microscopes (SEM) for this technique by using specifically designed attachments. A RAITH ELPHY Plus attachment installed in the JEOL JSM-840 in the Scientific and Technical Services of the Universitat de Barcelona (SCT-UB) was used. However, also specialized turn-key systems with advanced features specific to EBL are marketed. During this thesis a CRESTEC CABL-9500C system was used in the Technological Center of the Optoelectronic Systems and Microtechnology Institute (CT-ISOM) of the Universidad Politécnica de Madrid through a project for the use of this singular scientific and technological equipment (ICTS) financed by the science and innovation department (MICINN) of the Spanish government.

3.2.1. Electron optics

Essentially, an EBL equipment consists of an electron source that generates and accelerates electrons, electromagnetic or electrostatic lenses that condense, focus and deflect the beam and a beam blanker, that allows a fast switching of the beam. The beam is focused on the resist, which is then locally sensitized. The deflection of the beam is controlled by a pattern generator that scans the beam on the regions to be exposed. Figure 3.9 shows examples of signals sent to the deflection lenses, in order to control the position of the beam.

Electron sources

Electrons can be emitted from a material either heating it, applying an intense electric field, or a combination of both methods relying on Schottky effect. For EBL

Source	emissivity (A/cm^2sr)	virtual diameter of source (nm)	energy dispersion (eV)	required vacuum (Pa)
W thermal	$\sim 10^5$	25000	$2-3$	10^{-4}
LaB_6 thermal	$\sim 10^6$	10000	$2-3$	10^{-6}
hot Schottky effect	$\sim 10^8$	20	0.9	10^{-7}
cold field effect	$\sim 10^9$	5	0.22	10^{-8}

Table 3.1.: Typical SEM electron sources characteristics. [Rai-Choudhury, 1997]

applications stability of emitted current is one of the most important features. For this reason, cold field effect sources, which show large variations in emitted current with time, are not the ideal choice, despite their low energy dispersion and small virtual diameter of the source. On the other hand, tungsten and LaB_6 tips (thermal emission) are much cheaper but provide lower emissivities and resolution and have a short lifetime. Hot Schottky effect emitters have reached a compromise between the different characteristics with emissivities and resolution close to field effect sources but much higher stability and long lifetimes (years). In table 3.1 a summary of electron sources characteristics is exposed.

The JEOL JSM-840 used in this thesis was equipped with a tungsten filament which allowed the patterning of features (circles) with a minimum diameter of 80 nm after heavy optimization. However, the age of the system added a difficult to correct astigmatism and probably produced positively tapered walls. On the other hand, the CRESTEC CABL-9500C, equipped with a hot Schottky effect emitter, allowed the patterning of 20 nm in diameter features pretty straightforward and even smaller when optimized. Compared to the average lifetime of a couple of weeks for the tungsten filament (not used all day), the hot Schottky emitter was turned on (emitting electrons) during all day and for several months without interruption.

Beam blanker

EBL systems are equipped with a beam blanker in order to shut the electron beam off while moving through the resist, without exposing it, or while moving from one object to another in a single write field. A typical approach is to electrostatically deflect the beam in the column so that it is completely masked by one of the following apertures. In order to do so, a beam blanker must fulfill some requirements:

- Beam attenuation must be at least 10^6 times the original current
- Any noise introduced by the blanker must correspond to a beam deviation smaller than the desired pixel dimension

- Response time must be much shorter than the exposure time of a single pixel

3.2.2. Electron-solid and electron-resist interaction

EBL resolution does not only depend on electron optics but also on the way electrons and resist/solids interact. When the electron beam enters into the resist, several phenomena may happen and the same way when the electrons reach the substrate.

Depending on the atom and electron involved in the interaction, different processes may happen: [Businaro, 2005]

(a) Elastic scattering: After electron and atom collision, the latter remains in its fundamental state, while the electron keeps its energy but in a different movement direction.

(b) Inelastic scattering: The collision promotes a bonded electron to a higher energetic level. The incoming electron looses energy.

(c) Ionizing interaction: The collision promotes an atomic electron to the continuous spectrum of the atom. Secondary electron (less than 50 eV is emitted).

(d) Induced de-excitation: Atom's excitation energy is transferred to the incoming electron.

(e) Recombination: All energy of incoming electron is transferred to the atom's electrons.

Essentially, only processes from 1 to 3 play an important role in EBL. When electrons enter into the resist, they suffer several low angle scattering interactions (see figure 3.10), which tend to enlarge initial beam diameter. These are called *forward scattered electrons*. As electrons penetrate into the resist or arrive to the substrate, they may be scattered by a large angle which may result in a movement opposite in direction to the initial. These are called *backscattered electrons*.

During all these processes, inelastic scattering occurs and secondary electrons with energy between 2 and 50 eV are emitted (the majority of them well above the 3.7 eV [Leroy et al., 1993] needed to break abundant C–C bonds in polymers).

Secondary electrons emitted on the way back of backscattered electrons expose adjacent regions to beam position, which can reach several micrometers. This is called *proximity effect*.

In conclusion, resolution of EBL is in practice determined, not only by electron optics, but also by the ability to avoid backscattered electrons and by the enlargement of the beam due to forward scattering.

Proximity effect

When patterning features with different areas or simply non uniform patterns, the exposure a certain region is reinforced with those in the vicinities, due to backscattered electrons. Therefore, the proximity of other structures has to be taken into

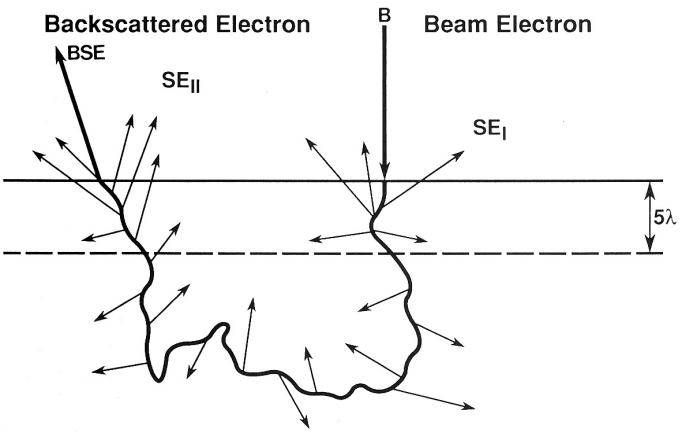

Figure 3.10.: Possible scattering path of an electron once inside a solid. Either several low angle scattering collisions or a high angle scattering may occasionally backscatter the electron.

account in order to obtain patterns with the desired dimensions (not overexposed). Due to the micrometric range of proximity effect, nanometric structures are the most affected.

Luckily, for regular patterns (e.g.: reticular pattern of holes or parallel lines over a micrometric area) proximity effect can be corrected by slightly reducing the overall electronic dose. However, for more complex designs such as those used for microelectronics, microelectromechanical systems, microfluidic devices or information codification, an accurate correction must be performed to preserve shapes and dimensions.

Most methods for proximity effect correction rely in modulating applied electronic dose for the different elements of the pattern or deliberately modifying their dimensions. For uniform patterns, a global change in the electronic dose is usually enough. On the other hand, for complex designs, the elements can be divided in smaller units to which specific doses are applied.

In the case of very thin substrates, as those used for X-Ray masks, the increase of electron energy favors the elimination of the effect, as electrons go through the mask without the possibility of being backscattered. However, in case of thicker substrates, the atomic number determines the amount of proximity effect.

Charge dissipation

When using isolating substrates for EBL processes, charge may accumulate and deform the patterns, specially when they are small and close one to each other. To avoid this charge, thin films of 5 to 10 nm of Al, Au, Au/Pd or Cr may be deposited on top of the resist, when energies above 10 keV are used. For such energies, the

metallic film does not interfere in electrons path and avoids charge accumulation. Other possibilities include the use of electrically conducting resists.

4

Characterization techniques

Analogously to Chapter 3, here the experimental techniques used to characterize both the deposited a-C films and the etched nanostructures will be described. Some of them have been used in the research group for the first time during this thesis:

- Dynamic contact angle measurements with surface free energy calculations.
- Humidity dependant friction measurements through a self-made humidity PID controller attached to a nanotribometer.
- Optical emission actinometry

4.1 Surface free energy determination

It is of interest for this thesis the characterization of the films in terms of their adhesion to other surfaces. The thermodynamic *work of adhesion* between a solid surface and a liquid is related to the surface free energy of the solid and the surface tension of the liquid. These magnitudes are experimentally available by different methods, one of them being the connection between wetting parameters and thermodynamic magnitudes.

Wetting involves the interaction of a liquid with a solid. It can be the spreading of a liquid over a surface, the penetration of a liquid into a porous medium, or the displacement of one liquid by another.

Wetting is most often described by the contact angle of a sessile or resting drop, low contact angles meaning high wettability and the other way round. Systems having more than one stable contact angle are said to show contact-angle hysteresis.

4.1.1. Contact angle measurement

Although several methods exist for measuring contact angles of liquids on solids, two of them are the most extended: sessile drop and Wilhelmy plate methods. In the former, the interface between solid, liquid and gas is video recorded and analyzed by adjusting an appropriate model. In the latter, the force of the meniscus is measured with an electrobalance.

Contact angle measurements can be carried out in either static or dynamic mode. In static mode, the liquid/solid/gas (l/s/g) interface does not move, while in dynamic mode the opposite happens.

Dynamic mode provides a measurement less dependent on the position of the interface on the surface of the film. Moreover, it allows the measurement of two magnitudes: the advancing and receding contact angles, as well as the hysteresis, defined as the difference between the advancing and receding angles. The advancing contact angle is measured when the l/s/g interface moves towards the gas phase, while the receding is measured when it moves towards the liquid phase. If the interface moves at sufficiently low speed, the advancing contact angle tends to the static contact angle value. This is the quasi-static case.

Hysteresis is caused by metastable states at the s/l/v interface. Each of these states is characterized by a contact angle. Surface heterogeneity is the major cause of hysteresis, small amounts being able to lead to large hysteresis. A number of studies about hysteresis have been made. Most of them agree qualitatively in that the advancing angle is a suitable measure of the low-energy portion of a surface whereas the receding angle is highly affected by the high-energy portion.

Starting from Young's qualitative model of 1805 (see next subsection), Laplace expressed in an adequate mathematical form the shape of solid/liquid interfaces in 1806:

$$\Delta p = \gamma \nabla \cdot \hat{n} = \gamma \left(\frac{1}{R_1} + \frac{1}{R_2} \right) \tag{4.1}$$

where Δp was the pressure difference between the concave and convex side of the surface at each point of the interface, γ was the liquid surface tension, $\hat{n}$ was the unitary normal vector to the surface, and R_1 and R_2 were the principal radii of curvature at each point.

Young-Laplace model describes exactly the shape of a drop but, in general, equation (4.1) does not have an analytical solution and thus their solutions have to be numerically computed. For this reason, other numerically faster methods were used depending on the experimental conditions on which the drop is observed (gravity, for example, is increasingly important as drop volume is higher). Elliptical, polynomial, circular, height-width or tangential methods.

4.1.2. Wettability

In 1805, Thomas Young [Young, 1805] related the contact angle to the surface energies of the three interfaces meeting at the interline:

$$\cos \theta_{s/l} = \frac{\gamma_{s/g} - \gamma_{s/l}}{\gamma_{l/g}} \tag{4.2}$$

where subindexes s, g, l and / correspond to "solid", "gas", "liquid" and "interface" respectively, and $\gamma_{s/g}$, $\gamma_{s/l}$, and $\gamma_{s/l}$ are the reversible works of formation of such interfaces:

$$\gamma_{i/j} = \left(\frac{\partial G_{i/j}}{\partial A_{i/j}}\right)_{T,p,equil} \tag{4.3}$$

$G_{i/j}$ being the Gibbs excess free energy of the i/j interface, $A_{i/j}$ its area, T the absolute temperature, p the pressure and "equil" denoting the assumption of adsorption equilibrium, in the case of multicomponent systems. We denote vacuum by "o" and we define $\gamma_s \equiv \gamma_{s/o}$ for abbreviation purposes.

Experimentally, it can be observed that for low-energy surfaces, the spreading pressure of a vapor on a solid $\pi_{s/g}$, is close to zero when $\theta_{s/l} > 0$. In this case, there is no practical difference between the free energy associated to the solid phase surface against the vapor-phase and the energies associated to those surfaces against vacuum. Thus, we can consider $\gamma_s \approx \gamma_{s/g}$, where the latter is directly measurable in the laboratory.

When a drop is placed on top of a surface, both the s/g and l/g interfaces are destroyed and s/l is created. Therefore, the work of adhesion $W_{a:s/l}$, defined as the work required to disjoin a unit area of the s/l interface, is given by:

$$W_{a:s/l} = \gamma_s + \gamma_l - \gamma_{s/l} \tag{4.4}$$

which is known as the Dupré equation. Combined with equation (4.2), Young-Dupré equation is obtained:

$$W_{a:s/l} = \gamma_l \left(1 + \cos\theta_{s/l}\right) \tag{4.5}$$

Since the interfacial tension between identical phases is zero, following the same reasoning, but for work of cohesion, leads to:

$$W_{a:i/i} \equiv W_{c:i} = 2\gamma_i \tag{4.6}$$

It usually is a premise that interactions between molecules in bulk phases or across interfaces between them are physical or chemical in nature. Physical interactions are always present and chemical interactions can arise whenever there is the possibility of donating a proton or an electron pair that is then shared between neighboring molecules or functional groups, leading to complexation, or adduct formation (all describable as acid-base interactions). It is further assumed that when chemical as well as physical interactions are possible, their effect on the macroscopic thermodynamic properties of the system is additive. For work of adhesion: [Berg, 1993]

$$W_{a:s/l} = W_{a:s/l}^{physical} + W_{a:s/l}^{chemical} \tag{4.7}$$

Physical interactions

Excluding Coulombic interactions (between ions) and metallic bonding, the physical interactions between molecules include the London (dispersion) forces, Keesom (dipole/dipole) forces and Debye (dipole/induced dipole) forces, known collectively as van der Waals forces. Forces due to quadrupoles or more complex permanent charge distributions are generally negligible.

London forces result from the natural oscillations of the electron clouds of the molecules inducing synchronous oscillations in the neighboring molecules. The resulting temporal dipoles of neighboring molecules have the mutual orientation producing maximum attraction.

Keesom forces result from interaction between permanent dipoles. When both molecules have substantial dipole moments, Keesom and London interactions are comparable in magnitude. If only one of them has a permanent dipole, it can induce a dipole in a neighboring molecule, which is known as Debye interaction. The contribution of this force is usually a few percent of the London interaction.

In order to calculate cross magnitudes (actually cross Hamaker constants) for van der Waals interactions, geometric mean mixing rule is usually of general validity [Berg, 1993, page 92]. It assumes $W^u_{a:s/l} = \sqrt{W^u_{c:s} W^u_{c:l}}$ (where u makes reference to every particular van der Waals interaction), which, considering equation (4.6) and Young and Dupré equations, is transformed into:

$$\begin{aligned} W^u_{a:s/l} &= 2\sqrt{\gamma^u_s \gamma^u_l} \\ \sum_u 2\sqrt{\gamma^u_s \gamma^u_l} &= \gamma_l \left(1 + \cos\theta_{s/l}\right) \end{aligned} \tag{4.8}$$

As long as γ_l is directly measurable, and many of them are already tabulated, equation (4.8) allows the calculation of the surface energy of a solid surface $\gamma_s = \sum_u \gamma^u_s$ (additivity of surface energy components after [Fowkes, 1962]) by measuring $\theta_{s/l}$ angles for sufficient liquids.

On the basis of Lifshitz theory [Lifshitz, 1956] calculations, van Oss et al suggested [van Oss et al., 1986] that polar (Keesom and Debye) contribution to surface tension was much smaller than previously though. London interaction is dominant and therefore all these contributions could be rolled into a single "Lifshitz-van der Waals" (LW) component. The remaining energy (previously assigned to polar interactions) should be now attributed to chemical interactions, and we have:

$$W^{LW}_{a:s/l} = 2\sqrt{\gamma^{LW}_s \gamma^{LW}_l} \tag{4.9}$$

By using inert liquids (that is $\gamma_l = \gamma^{LW}_l$), such as saturated hydrocarbons, LW component of a solid surface may be determined. From equation (4.8):

$$\gamma^{LW}_s = \frac{\gamma_l}{4}\left(1 + \cos\theta_{s/l}\right)^2 \qquad \text{if} \quad \gamma_l = \gamma^{LW}_l$$

Chemical interactions

Although many types of chemical reactions may take place across the solid/liquid interface, only reactions which do not destroy the long-term stability of the interface itself or result ultimately in changing the composition of either of the bulk phases are considered in this thesis. This leaves for consideration reactions that are capable of forming complexes between molecules on both sides of the interface.

It has been widely contended that nearly all of the chemical reactions between liquids and solid surfaces that are important in wetting phenomena are acid-base (AB) reactions [Berg, 1993; Fowkes, 1987]. Thus, equation (4.7) can be rewritten as:

$$W_{a:s/l} = W^{LW}_{a:s/l} + W^{AB}_{a:s/l}$$
$$\text{or } \gamma_i = \gamma_i^{LW} + \gamma_i^{AB}$$

which constitutes an example of multicomponent model. The most widely recognized and successful multicomponent model so far is the van Oss-Chaudhury-Good theory, which is described next.

4.1.3. van Oss-Chaudhury-Good (vOCG) correlation

In order to determine the acidic or basic functionality of solid surfaces, as well as the amount of AB component of surface energy, van Oss et al. proposed [van Oss et al., 1987] an expression for AB component of work of adhesion and surface tension:

$$W^{AB}_{a:i/j} = 2\sqrt{\gamma_i^+\gamma_j^-} + 2\sqrt{\gamma_i^-\gamma_j^+} \tag{4.10}$$

$$\gamma_i^{AB} = 2\sqrt{\gamma_i^+\gamma_i^-} \tag{4.11}$$

where γ_i^+ and γ_i^- are the characteristic acid and base parameters of each phase, respectively. No fundamental justification for using a geometric mean type of expression was given (or is needed, if the parameters are simply operational). Equation (4.10) defines the empirical parameters it contains. There is no way to meaningfully compare the characteristic parameters γ_s^+ and γ_s^- with other measures of solid surface acidity or basicity [Berg, 1993].

Adding AB term of equation (4.10) and LW term of equation (4.9) in Young-Dupré equation (4.5) we obtain:

$$\begin{cases} 2\sqrt{\gamma_s^{LW}\gamma_l^{LW}} + 2\sqrt{\gamma_s^+\gamma_l^-} + 2\sqrt{\gamma_s^-\gamma_l^+} &= \gamma_l\left(1+\cos\theta_{s/l}\right) \\ \gamma_l^{LW} + 2\sqrt{\gamma_l^+\gamma_l^-} &= \gamma_l \end{cases} \tag{4.12}$$

which is a $2L$ equations and $3+3L$ unknowns system, where L is the number of probe liquids and liquid surface tensions γ_l are considered known. The linearity

of the system is only achieved if one previously knows or can measure all three components of liquids (γ_l^{LW}, γ_l^+ and γ_l^-). However if more than three solids are analyzed with nine or more liquids, the non-linear equation system can be used to find a best-fit optimized solution.

I this thesis four liquids have been used to calculate γ_s: water, diiodomethane, formamide and dimethyl sulphoxide, and the solution to the overdetermined equation system has been found using the method described in Appendix A.

The basicity catastrophe

If one multiplies and divides γ_l^+ and γ_l^- by the same constant k, the new values $k\gamma_l^+$ and γ_l^-/k are again solution of the system and surface energies of the solid are also changed: $k\gamma_s^+$ and γ_s^-/k. Therefore, either a nonlinear equation system is solved, or a particular scale must be defined in which acid-base components of liquids will be measured. This is an important problem for vOCG theory. As long as the scale is not properly defined, a direct comparison of the acidic and basic parameters of the same material makes no sense. That is, $\gamma^+ > \gamma^-$ does not necessarily characterize a surface as acidic and the other way round. Comparisons only make sense within the same components (i.e., between components of the same type).

The original proposal of vOCG theory was that these components can be experimentally measured in a scale where water had equal acid and basic components. This assumption is critical, because although water is neutral for stoichiometric reasons in terms of Brønsted theory, in terms of Lewis' it is uncertain. In the case of common distilled or bidistilled water, carbon dioxide present in the air, due to its high Henry constant, is able to dissolve in water 30 times more than oxygen, with the result that common distilled water is commonly more acidic than basic. Therefore, imposing water as a neutral liquid in the vOCG scale, actually corresponds to reduce in a significant way the acidic strength of water and consequently, that of any other material. [Mittal, 2000, page 63]

Moreover, the measurements of surface tensions carried out by van Oss and coworkers by the "encased gel method" and by considering certain surfaces as monofunctional basic (they used the term monopolar), are experimentally difficult to perform and their interpretation is questionable. [Mittal, 2000, page 70]

One of the most important controversial issues of vOCG theory is the typical finding of the theory that polymer surfaces are strongly basic ($\gamma^+ < \gamma^-$), while certain materials' surfaces are thought to be acidic like PVC[1]. Some authors have proposed alternative scales or solutions [Good and Hawa, 1997], in order to improve the results of the original, while van Oss accepted the idea that the general prevalent basicity was a real fact [van Oss et al., 1997].

One of the alternative scales is that of Della Volpe and Siboni (DVS) [Della Volpe and Siboni, 2000] (see Table 4.1), which assigns water a LW component of $26.2\,{}^{\mathrm{mJ}}/_{\mathrm{m}^2}$ while the ratio γ^+/γ^- is set to 4.35. This scale shows better results: liquids and

[1] Polyvinyl chloride

Liquid	$\gamma^{LW}_{\text{vOCG}}$	γ^{LW}_{DVS}	γ^{+}_{vOCG}	γ^{+}_{DVS}	γ^{-}_{vOCG}	γ^{-}_{DVS}
Water	21.8	26.2	25.5	48.5	25.5	11.2
Ethylene Glycol	29.0	33.9	1.92	0.97	47.0	51.6
Diiodomethane	50.8	50.8	0.00	0.00	0.00	0.00
Formamide	39.0	35.5	2.28	11.3	39.6	11.3
Glycerol	34.0	35.0	3.92	27.8	57.4	7.33
Dimethyl sulphoxide	36.0	32.3	0.5	0.0373	32.0	763

Table 4.1.: Surface tensions in $^{\text{mJ}}/_{\text{m}^2}$ of typical contact angle probe liquids in the original vOCG scale [van Oss, 1994] or DVS scale [Della Volpe and Siboni, 2000].

solids are acidic or basic, and the acidic components are significant and greater than basic ones. PVF[2] and nylon 66 are effectively acidic surfaces while PMMA remains strongly basic. However, it still gives bigger basic than acidic component to PVC.

The ill-conditioning of the equation system

Another criticized aspect of vOCG theory is the non consistent results that arise from different experiments when used in the linear determined form (i.e., known liquid surface tension components and three probe liquids). Different triads of liquids give different results of surface free energy of the same solid, due to the ill-conditioning of the equation system [Della Volpe and Siboni, 2000; Della Volpe et al., 2004]. If we assume liquid surface tension components to be known, the set of equations (4.12) reduce to:

$$\mathbf{Ax} = \mathbf{b}$$

where

$$\mathbf{A} = \begin{pmatrix} \sqrt{\gamma_1^{LW}} & \sqrt{\gamma_1^{-}} & \sqrt{\gamma_1^{+}} \\ \sqrt{\gamma_2^{LW}} & \sqrt{\gamma_2^{-}} & \sqrt{\gamma_2^{+}} \\ \sqrt{\gamma_3^{LW}} & \sqrt{\gamma_3^{-}} & \sqrt{\gamma_3^{+}} \end{pmatrix}, \qquad \mathbf{b} = \begin{pmatrix} \gamma_1 \frac{(1+\cos\theta_1)}{2} \\ \gamma_2 \frac{(1+\cos\theta_2)}{2} \\ \gamma_3 \frac{(1+\cos\theta_3)}{2} \end{pmatrix}, \qquad \mathbf{x} = \begin{pmatrix} \sqrt{\gamma_s^{LW}} \\ \sqrt{\gamma_s^{+}} \\ \sqrt{\gamma_s^{-}} \end{pmatrix}$$

The use of improper liquids sets (i.e., without dispersive liquids or with two prevalently basic or prevalently acidic liquids) strongly increases the ill-conditioning of the system, so the wrong chemical choice is reflected on mathematics.

[2]Polyvinyl fluoride

Liquids			Condition number ℓ^1
Water	Ethylene Glycol	Glycerol	193.27
Water	Formamide	Dimethyl sulphoxide	119.84
Glycerol	Ethylene Glycol	Dimethyl sulphoxide	118.29
Formamide	Ethylene Glycol	Glycerol	74.99
Formamide	Ethylene Glycol	Dimethyl sulphoxide	53.10
Formamide	Glycerol	Dimethyl sulphoxide	36.93
Formamide	Ethylene Glycol	Water	27.79
Formamide	Glycerol	Water	25.46
Water	Ethylene Glycol	Dimethyl sulphoxide	21.76
Glycerol	Water	Dimethyl sulphoxide	19.99
Water	Ethylene Glycol	Hexane	6.43
Water	Ethylene Glycol	Hexadecane	5.62

Table 4.2.: Condition numbers for different triplets. Extracted from [Della Volpe et al., 2004]

A quantitative way of expressing the conditioning of the system is through the condition number, corresponding low values to a well-balanced set of liquids and high values to limited and/or unbalanced sets. It is defined as $\mathrm{cond}\,(\mathbf{A}) = \|\mathbf{A}\| \left\|\mathbf{A}^{-1}\right\|$, where $\|\mathbf{A}\|$ is the norm of matrix $\mathbf{A}$ ($\|\mathbf{A}\|_1 = \max_j \Sigma_i |A_{ij}|$ for ℓ^1 matrix norm). The choice of norm makes almost no difference in the order relation of the condition numbers. In Table 4.2 these are shown for different triplets.

A possible way of overcoming the problem of the "goodness" of the triplets is by using wide sets of liquids (10 or more). The increase in the number of liquids equilibrates the LW, acidic and basic components of the set and provides more accurate solutions. The use of more than three liquids in vOCG theory corresponds to finding a best-fit solution for an overdetermined equation system. An overview of the solving methods for such type of problems is given in Appendix A.

4.1.4. KSV CAM200-Auto4 contact angle meter

A CAM200 goniometer from KSV Instruments (see figure 4.1) has been used through this thesis in order to measure the contact angle of different liquids on the deposited films by the sessile drop method. The goniometer is equipped with an Auto4 auto-dispensing unit that allows speed-controlled dispension from up to 4 different sy-

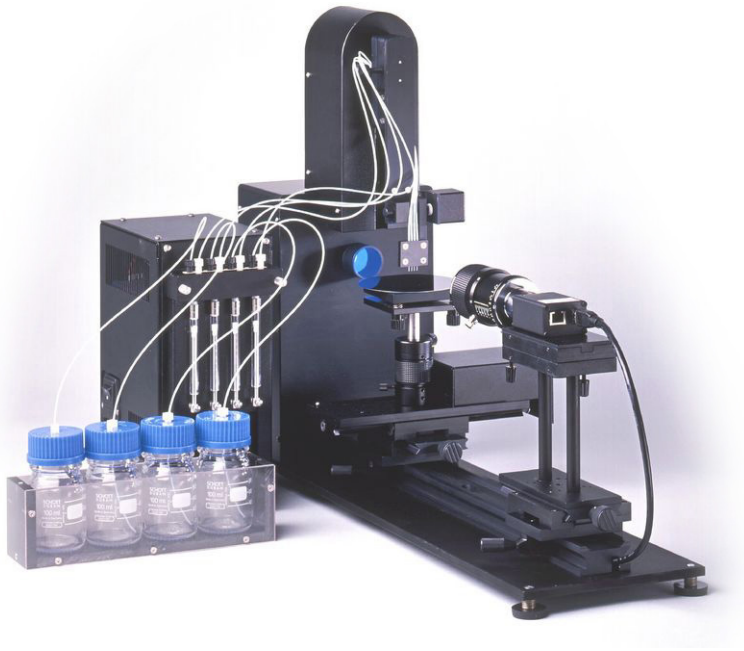

Figure 4.1.: KSV Instruments CAM200-Auto4. Extracted from KSV Instruments web page.

ringes and motorized sample holder. The liquid is dispensed on top of the surface of interest and a video camera records, through a 50 mm lens, a sequence of images which are subsequently analysed. The equipment is capable of recording up to 130 $^{\text{frames}}/_{\text{s}}$ at full resolution and up to 420 $^{\text{frames}}/_{\text{s}}$ when it is reduced. The background lighting is LED-based monochromatic. The automatic dispenser mechanism allows dispensing speeds from 0.8 $^{\mu\text{l}}/_{\text{s}}$ to 50 $^{\mu\text{l}}/_{\text{s}}$ when using standard 1 ml syringes.

The controller software allows the measurement of contact angles from the recorded frames by several methods, including Young-Laplace equation solution.

The contact angle measurements on the deposited films were done with all liquids shown in table 4.1. A dispensing speed of 0.8 $^{mm^3}/_{\text{s}}$ or lower was used for all of the measurements.

4.2 Ball-on-disk friction test

The application of a precisely known force N on a ball against the surface of interest and the measurement of the tangential friction force F_f in a circular movement, constitutes the classic ball-on-disk test configuration, and allows the measurement of friction coefficient μ:

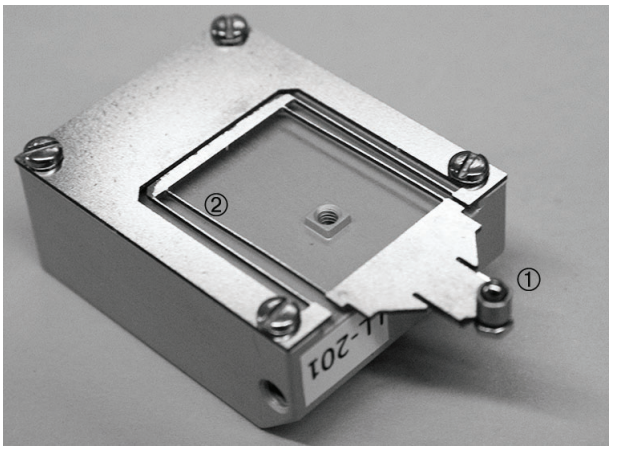

Figure 4.2.: Sensing head of CSM Nano Tribometer. ① is the ball that slides over the surface. ② is the spring that allows the conversion of the horizontal and vertical displacements to F_f and N forces, respectively.

$$\mu = \frac{F_f}{N}$$

In such configuration, the horizontal deflection of the sensing arm is related to the friction force. Therefore, the experimental parameters of the test are: the normal load N, distance from spin axis R, angular speed ω, and lubricant (if present). On the other hand, environmental parameters would include: temperature, pressure and gas composition.

In this thesis, a relative humidity controller has been designed, in order to probe friction under different environmental conditions (see 4.2.2 for details). On the other hand, temperature control has relied on the external HVAC system of the laboratory.

4.2.1. CSM Nano Tribometer

CSM Nano Tribometer equipment, installed on the FEMAN Group of the Department de Física Aplicada i Òptica of the Universitat de Barcelona, allows different sliding tests configurations: ball-on-disk, pin-on-disk, ball on linear track and pin on linear track. Selection of either pin or ball depends on what is installed in position ① of figure 4.2. In order to test friction for linear or circular track configurations, two sample holders are provided.

The equipment permits the installation of different sensing heads which, depending on their spring constant (part ② of figure 4.2), provide different normal and friction force ranges (see table 4.3). Precisely, the peculiarity of this tribometer is the capability of applying very low normal loads, which reduces the test area and wear of the film.

Magnitude	Value
Load range	$50\,\mu N - 1\,N$
Load resolution	$0.1\,\mu N$
Friction range	$10\,\mu N - 1\,N$
Friction resolution	$1\,\mu N$
Rotation speed range	$1\,rpm - 100\,rpm$
Rotation radius	$30\,\mu m - 10\,mm$
Linear stroke length	$10\,\mu m - 500\,\mu m$
Linear speed	Up to $10\,^{mm}/_{s}$
Linear frequency	$0.1\,Hz - 10\,Hz$

Table 4.3.: CSM Nano Tribometer specifications. Extracted from CSM datasheet.

4.2.2. Relative humidity proportional-integral-derivative controller

In order to control humidity of friction tests, a self-regulated controller has been designed during this thesis. The system allows a precise setting of relative humidity (RH) of $N_2 + H_2O$ atmospheres with stability within $\pm 0.1\%$RH.

A diagram of the controller is shown in figure 4.3. N_2 gas is bubbled in a water bath with a flow controlled by means of a mass flow controller (MFC). Temperature control of water allows different degrees of gas humidification and therefore ranges of relative humidity settings. Humid nitrogen is mixed with dry gas, in order to speed up drying of the chamber. Finally, a RH transducer is used to regulate humid N_2 flow, whose dynamic correction is carried out by a proportional-integral-derivative controller integrated into the MFC unit.

The transducer has been carefully calibrated against known patterns of humidity provided by supersaturated salts baths. Calcium chloride 6-hydrate ($CaCl_2 \cdot 6H_2O$) and potassium tartrate ½-hydrate ($C_4H_4K_2O_6 \cdot \frac{1}{2}H_2O$), have provided 31.0% and 75.0% of relative humidity at 25℃, respectively [O'Brien, 1948].

Although CSM Nano Tribometer chamber is prepared for environmental control, additional precautions have been necessary, specially those related to chamber sealing.

4.3 Wear measurement

The wear rate (W) of a material is defined by the volume of material V removed in a sliding test per unit of sliding distance s and applied normal force F:

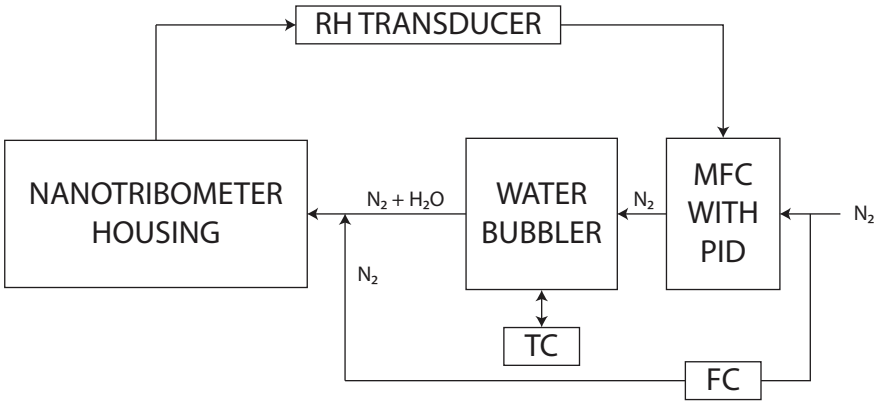

Figure 4.3.: Relative Humidity (RH) controller diagram. MFC stands for Mass Flow Controller; TC stands for Temperature Controller and FC stands for Flow Controller.

$$W = \frac{V}{s\,F} \tag{4.13}$$

This magnitude is not independent of measurement conditions, but instead is modified by the environment, the use of lubricants or abrasives. or the materials of the counterface among others. Therefore, the use of repeatable and constant conditions is a must. Moreover, comparison between different values is only possible when similar or equal test conditions are used.

Several methods are used to test wear resistance of thin films. Among them, in this thesis the Calotest method has been used, which requires a small test surface and consists of a fairly simple test apparatus.

4.3.1. CSM Calowear test

CSM Calowear equipment, installed on the FEMAN Group of the Department de Física Aplicada i Òptica of the Universitat de Barcelona has been used to measure the abrasive wear resistance of the amorphous carbon films. The measurement method consists on a plastic or hardened stainless steel ball (② in figure 4.4) leaning against the surface ① of interest (tilted a known angle α) and spun by a rotating shaft ③ at a known distance from the surface. As the ball center does not move relatively to the surface, the footprint of the test is very small.

In order to wear hard films, a suspension of alumina microparticles in glicerine is usually used as abrasive, between ball and film. Special care must be taken with both the alumina powder and the glicerine so that they do not absorb water, as

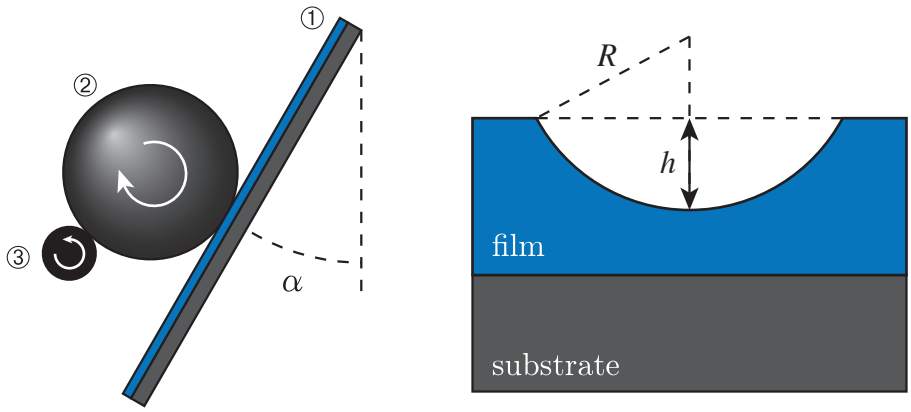

Figure 4.4.: Calotest wear test sketch. ① is the film to be characterized, ② is the hardened stainless steel ball and ③ the rotating shaft.

both of them are hygroscopic. A suspension with water can affect substantially the result of the wear process, by creating hydroxyl terminations that bond either to the abrasive suspension or to the counterpart. In the presented experiments, a 1:3 suspension of spherical particles 1 µm in diameter in glicerine has been used, trying to work always in similar environmental conditions of temperature and humidity.

From the ball weight and radius (R), the angle α and the distance between shaft and the surface, the force F can be determined. On the other hand, the sliding distance depends upon the rotation speed ω and test duration t. Finally, the removed volume can be calculated from topographical measurements of the surface. In this thesis a stylus profiler (described in 4.4.1) has been used to determine the depth of the crater.

In this configuration, equation (4.13) turns into:

$$W = \frac{\frac{1}{3}\pi h^2 (3R - h)}{\omega R t F} \tag{4.14}$$

4.4 Topography

4.4.1. Stylus profiler

A simple method for measuring 1D topography of a film or sample is by probing the surface with a stylus using a certain constant force. This is the approach of the Dektak 3030 profilometer of Veeco, which uses a diamond tip and measures its vertical displacement by means of a capacitance transducer.

The aim of this type of equipment is to allow the measurement of large distances (from 50 µm to 50 mm) with high vertical (z) resolution (0.1 nm, 1 nm or 2 nm for 6.5 µm, 65.5 µm or 131 µm z-ranges, respectively). Depending on the hardness of the sample to measure, the applied force can be set from 10 µN to 400 µN.

A Dektak 3030 profiler, installed at the Departament de Física Aplicada i Òptica of the Universitat de Barcelona, and a Dektak 6M installed at the Cientific Park of Barcelona (PCB-UB) has been used through this thesis in order to measure the crater depth of Calowear tests and the intrinsic stress σ of the deposited films.

In order to carry out these second measurements, the Stoney equation [Stoney, 1909] has been used:

$$\sigma = \frac{Y_s\, t_f^2}{6\ (1-\nu_s)\ t_c} \left(\frac{1}{R_f} - \frac{1}{R_s} \right) \tag{4.15}$$

where Y, t and ν are the Young's modulus, thickness and Poisson's coefficient of either the substrate (s) or the film (f), respectively, and R is the radius of curvature of the sample before (s) and after (f) the film deposition. The equation assumes positive σ values for tensile stress and negative for compressive stress.

4.4.2. Atomic force microscopy

Another approach to topography measurement is that used by the so called Atomic Force Microscopy (AFM), which belongs to a broader group of techniques: Scanning Probe Microscopy (SPM). SPM techniques rely on a small tip that probes the surface in a line by line fashion, thereby creating a 3D surface image.

AFM is characterized by measuring the force exerted by the surface on the tip. When the main interaction is magnetic, though, the technique is called Magnetic Force Microscopy (MFM).

In AFM, a cantilever with a sharp tip is scanned across the surface while its position is monitored by using a reflecting laser beam (see figure 4.5a) [Kelsall et al., 2005].

The main imaging modes used with AFM are (see figure 4.5b):

- Contact mode: The tip is brought to a few angstroms from the sample surface, where the interatomic force between the cantilever and the sample is predominantly repulsive, due to overlapping of electron clouds. It provides the highest resolution.

- Non-contact mode: The tip is forced to oscillate close to the resonant frequency of the cantilever (stiffer than for contact mode) at a distance of ten to a hundred of angstroms. Here, the interatomic force between tip and sample is attractive, largely as a result of long-range attractive van der Waals interactions. This mode removes the possibility of contamination or degradation of the surface by the tip, as can occur in contact mode. However, the presence of a few

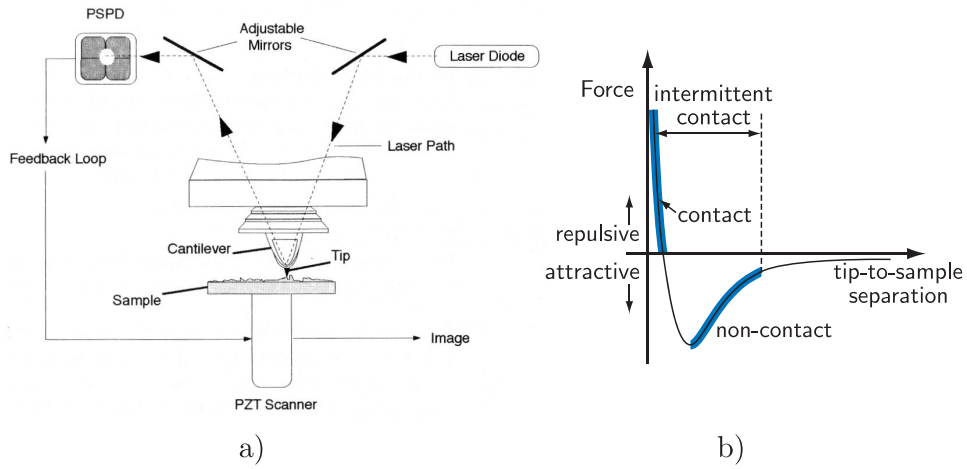

Figure 4.5.: a) Usual AFM setup, where a laser beam reflection is monitored in order to determine the vertical position of the cantilever. b) Force between tip and sample as a function of their separation and operating modes.

monolayers of liquid on the surface of a sample will result in non-contact mode to image the surface of the liquid, whereas contact mode will penetrate it to image the underlying surface.

- Tapping mode: Similar to non-contact mode, except that the tip is vibrated closer to the surface, so that at the bottom of its travel it just touches the sample. Tapping mode is less likely to damage the sample than contact mode because it eliminates lateral forces between the tip and the sample.

The topography of the analyzed surface may be provided by the cantilever deflection (or vibration amplitude in non-contact and tapping) or by the z position of the scanner. In the first case, the height of the cantilever is kept constant, and its deflection or changes in vibrating amplitude are interpreted as surface features. In this constant-height mode, the force exerted against the surface is not constant, but the speed of the scan is fast. On the other hand, when using the constant-force mode, the scanner corrects its z position by using a feedback circuit. In this case the force is well controlled, but the imaging speed is limited by the feedback circuit.

4.5 Scanning electron microscopy

The same principles (small electron diffraction) that allow high resolution with EBL (see section 3.2) also permit the observation of samples by analyzing the electrons emitted after irradiation. The experimental setup for EBL and SEM is extremely similar. Both share similar or equal electron source, electron optics and vacuum

system. However, the mode of operation for both of them is different. For EBL, the electron beam is focused on the resist surface and scanned on the regions that must be exposed. To do this, fast and precise electrostatic lenses are used. Instead, in SEM most lenses are electromagnetic, stable without too much shielding. Also, the beam blanker is not necessary for SEM.

However, the main difference in operation regards the way the beam is scanned over the sample surface. As opposed to EBL, in SEM the beam is always scanned, line-by-line over a surface depending on the set up magnification. On interaction with the sample, the electron beam penetrates a few µm and electrons (secondary, backscattered and Auger) and X-Rays are emitted. SEM focuses on the emission from the sample.

The energy distribution of the emitted electrons when irradiated with a beam with energy E_0 is represented in figure 4.6. The main part of emitted electrons are backscattered. That is, electrons that have suffered several elastic scattering until their direction is changed and leave the sample again. A small part of the electrons, called "secondaries", with energies under 50 eV is observed experimentally and correspond to the inelastic scattering between energetic electrons from the beam and conduction band electrons. Due to the large energy difference between these electrons, only a small part can be transferred. Also, due to this small energy their mean free path in the sample's volume is short so that the probability of an electron to leave the sample decays exponentially with depth (~ 1 nm for metals or ~ 10 nm for dielectrics). Once secondary electrons have left the sample, a positively biased detector attracts and counts them for every image pixel.

Unless otherwise noted, SEM images are representations of the secondary electrons emitted from the sample. However, also backscattered electron detectors or X-Ray spectrometers are commonly found on SEMs. Backscattered electrons commonly provide better chemical contrast, while X-Ray analysis provide elemental composition information.

4.6 X-Ray photoelectron spectroscopy measurements

X-Ray Photoelectron Spectroscopy (XPS), also known as Electron Spectroscopy for Chemical Analysis (ESCA), is a surface technique based on the photoelectric effect, that provides information about the elemental composition and chemical bonds present on the first ~ 10 nm from the surface.

After the First World War several groups analyzed the energies of electrons emitted from metals bombarded by X-rays. By 1914, Rutherford came close to stating the basic XPS equation:

$$E_K^s = h\nu - E_B - \phi_s \tag{4.16}$$

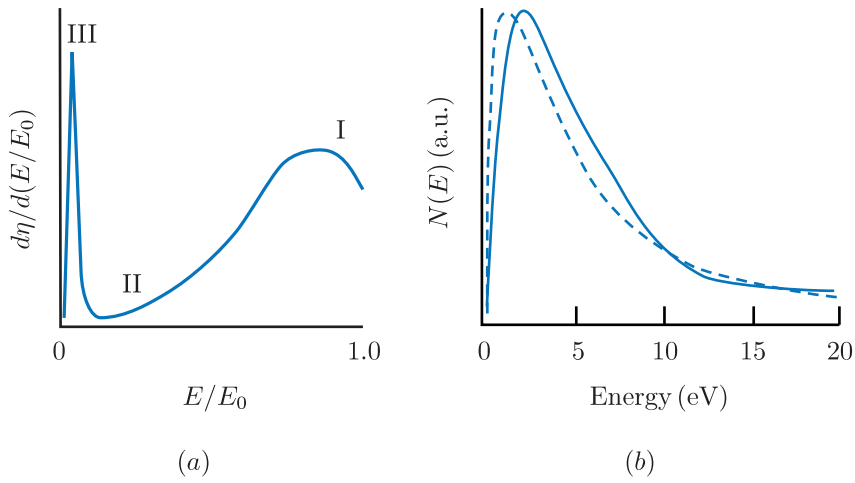

Figure 4.6.: (a) Energy distribution of electrons emitted from a sample. Regions I and II are backscattered electrons. Region III are secondary electrons. (b) Energy distribution of secondary electrons: measured (solid) and calculated (dashed) [Goldstein et al., 1992].

where E_K^s is the photoelectron kinetic energy with respect to the vacuum level of the sample, $h\nu$ the exciting photon energy, E_B the electron binding energy in the solid and ϕ_s its work function (Rutherford omitted this final term). [Briggs, 1998]

However, simultaneous measurement of E_B and ϕ_s is not readily achieved. In order to circumvent this difficulty, K. Siegbahn, who developed the technique during decades, noted that when examining conductors or even narrow band semiconductors, the sample could be placed in conductively contact with the conductive probe of the spectrometer. In such condition, Fermi edge coupling was achieved, and so assumed the spectrometer is calibrated against a well-established E_B, expression (4.16) could be rewritten as:

$$E_K = h\nu - E_B - \phi_{sp} \tag{4.17}$$

where ϕ_{sp} is known from the calibration. This situation is schematized in figure 4.7.

In an XPS instrument, a X-ray beam commonly coming from an Al or Mg cathode is focused on the sample. X-Rays produced with Al sources can be monochromatized in the K_α line (1.4866 keV) using a quartz crystal, resulting in the elimination of the Bremsstrahlung, satellite and ghost radiation to a linewidth of less than 0.5 eV.

These soft X-Rays focused on the sample, penetrate many microns into it. X-Ray absorption by an atom in the solid leads to the ejection of an electron, but only those generated a few nanometers away from the surface will have enough kinetic

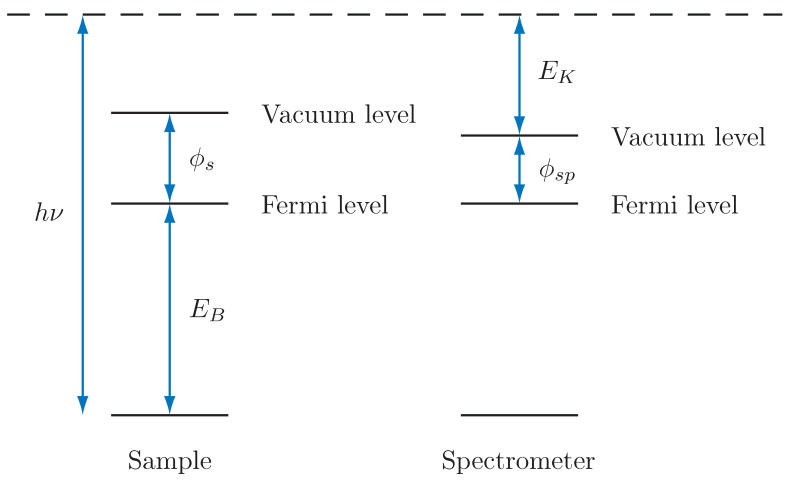

Figure 4.7.: Energy level scheme of XPS binding energies for a conducting sample. [Barr, 1994]

energy to reach the vacuum level. This particularity makes XPS a surface analysis technique.

The spectra collected in a XPS instrument shows a series of peaks corresponding to transitions in core levels, valence levels, or Auger transitions. The characteristic energy peaks of each element allows their quick identification, while the shift from this energy position and the shape of the peak describes the chemical bonding of the atom.

The XPS experiments in this thesis were carried out in a PHI 5500 Multitechnique System (from Physical Electronics) with a monochromatic X-ray source (Al K_α line) placed perpendicular to the analyzer axis. The analyzed area always was a circle of 0.8 mm in diameter. General spectra were acquired with a pass energy of 187.85 eV and 0.8 eV/step of resolution. On the other hand, high resolution scans were taken using 11.75 eV and 0.1 eV/step, respectively. All the measurements were made in a UHV chamber (pressure between 10^{-5} Pa and 10^{-6} Pa).

4.6.1. Analysis of hydrogenated amorphous carbon films

The first obvious problem of this technique with hydrogenated amorphous carbon films is the impossibility of measuring the amount of hydrogen in the film. However, still useful information can be obtained from XPS, such as carbon to fluorine atomic ratio, possible contamination, and information about chemical bonds of carbon.

Diamond has its C1s peak shifted 0.9 eV to higher energy than graphite, due to the reduced bond length of the latter. This difference has been associated in the literature to sp^3 and sp^2 bonds and has been successfully checked against the pre-

ferred technique for sp^3/sp^2 ratio determination, Electron Energy Loss Spectroscopy (EELS) [Haerle et al., 2001; Robertson, 2002].

For the determination of functionalities, fluorocarbon polymer data on peak position has been used from an extensive review on fluorinated carbon materials [Nansé et al., 1997]. That is, binding energy shifts of the 1s level of carbon atoms linked to one, two and three fluorine atoms are $3.0 \pm 0.2\,\text{eV}$, $6.1 \pm 0.2\,\text{eV}$ and $7.7 \pm 0.2\,\text{eV}$. These values have been used as a first approach to the analysis, due to structural differences between fluorocarbon polymers and fluorine-containing hard amorphous carbon.

Finally, the dielectric nature of the films, can introduce energy shifts in the spectra that must be corrected before comparing between them. In this thesis, a contamination peak has been used as reference for shift-correction of the spectra.

4.7 Optical emission spectroscopy actinometry

Optical emission spectroscopy actinometry (OESA or OEA) is a characterization technique of optical emitting species with respect to a constant-concentration non-reacting actinometer (e.g.: an inert gas in a low-pressure plasma). The technique is commonly performed in low-pressure plasmas to overcome the technical difficulties of other techniques as ion mass spectroscopy.

In a plasma, electron impact on species at their ground state may produce the following reaction:

$$e^- + X \rightarrow X^\star + e^-$$

where X is the species of interest, and the reaction is controlled by an excitation efficiency constant k_X.

Once excited, species may undergo different de-excitation paths; one of them being emission of photons with frequency ν:

$$X^\star \rightarrow X + h\nu$$

with a Γ_X branching ratio to all other possible de-excitation paths.

In this circumstances, the intensity of emission from the species X is:

$$I_X = \Gamma_X k_X [e^-][X]$$

where $[e^-]$ is the electron density and $[X]$ the concentration of species X. The excitation efficiency k_X is a function of the electron energy distribution function (EEDF) $f(\epsilon)$ and the excitation cross section $\sigma_X(\epsilon)$:

$$k_X = \int_0^\infty v(\epsilon)\sigma_X(\epsilon)f(\epsilon)\,dx$$

$v(\epsilon)$ being the electron velocity.

In order to take into account the changes in all the factors that control I_X, the actinometry technique relies on the introduction of an actinometer "Act" (commonly an inert gas) so that:

$$\frac{I_X}{I_{\text{Act}}} = \frac{\Gamma_X k_X [e^-][X]}{\Gamma_{\text{Act}} k_{\text{Act}} [e^-][\text{Act}]} \tag{4.18}$$

Maybe the most restrictive requirement for a valid analysis, is the adequate choice of the actinometer. This is chosen so that the group of electrons involved in the reactions are in the same energy range (i.e.: the monitored transitions have the same energy threshold) and the functionality with energy of the cross sections for both the actinometer excitation and the analysed excitation are similar. In these conditions, equation (4.18) can be expressed as:

$$[X] \propto \frac{I_X}{I_{\text{Act}}}[\text{Act}] \tag{4.19}$$

As summary, valid actinometry requires:

- Actinometer and measured species undergo the same excitation path (electron-impact).
- The relaxation occurs exclusively by photoemission or by photoemission plus a parallel de-excitation pathway with a constant branching ratio. This is usually true for low-pressure plasmas: the time for emission is much faster than the time between molecular collisions.
- Both species have similar cross-section functionality with energy and similar excitation thresholds.

In order to perform the optical emission acquisitions, a EPP2000C-UV-VIS spectrometer was used. All the figures shown in this section were made up from acquisition data taken during 20 s and averaged from 4 to 6 measurements from a pulsed-DC plasma at 56 W and 100 kHz with a positive pulse width of 2016 ns. The followed lines or bands are shown in table 4.4 [Pearse and Gaydon, 1976].

Species	λ (nm)
CH	431.5
H_α	656.3
H_β	486.1
CF_2	262.9
F	712.8

Table 4.4.: Optical lines followed for plasma chemical composition analysis.

4.7.1. Actinometry of fluorocarbon plasmas

The chemistry of carbon fluorides plasmas, often used in dry etching processes, was one of the first fields in which OEA was used. Its non-invasive and relatively simple setup are ideal for this purpose. In addition, the technique allowed the detection of stop layers, in etching processes.

The emission intensity of F^* at 703.7 nm (in this thesis the emission of F at 712.8 nm has been chosen due to the higher observed intensity) has an excitation threshold of 14.8 eV. Its comparison to the Ar^* emission at 750.4 nm with an excitation threshold of 13.5 eV is, therefore, straightforward. However, when it comes to monitoring molecular species (e.g.: CF_x), the much lower excitation thresholds (6.1 eV and 4.5 eV for CF^* and CF_2^*, respectively) suggest that actinometry might be invalid.

Instead of using molecular actinometers that might affect the plasma chemistry, Kiss et al. [Kiss et al., 1992] extended the validity of Ar actinometry of CF and CF_2 in CF_4 plasmas for a limited parameter space of pressure and power. The thesis was that if the EEDF can be assumed to undergo little change in this limited parameter space, then the restriction on the choice of an actinometer's excitation threshold can be relaxed and actinometry may be assumed to work.

In this thesis, the verifications that Kiss et al. carried out in CF_4 plasmas have been assumed to equally proof the validity of Ar actinometry in our CHF_3/CH_4 plasmas with the used pressure and power parameters.

4.8 Ion energy measurement

In order to measure ion energy and current density of an ion beam, the CEA device from CCR GmbH has been used, which is a Faraday cup. Schematically represented in figure 4.8, this device allows different operation modes depending on the potentials applied to each electrode.

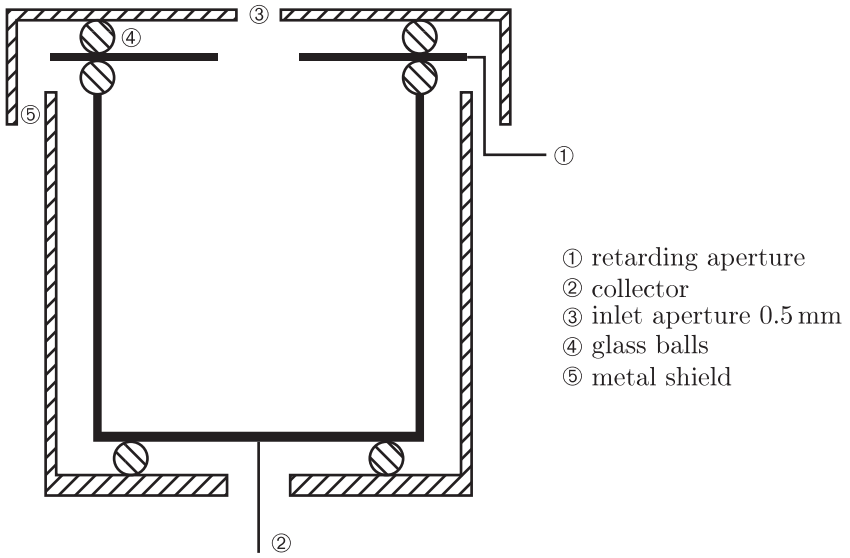

Figure 4.8.: Schematic representation of the CEA

Commonly, the metal shield (⑤ in figure 4.8) is grounded so that the plasma or the ion beam surrounding the analyzer is not perturbed by the potentials of the inner electrodes (① and ②). Soon after surpassing the inlet aperture, incoming ions find the retarding potential and then the collector bias. The operation of the device must take into account if only ions or both electrons and ions are being introduced into the cup.

If both particles are present, when performing ion current measurements, the retarding electrode can be negatively polarized so that electrons cannot go to the collector and only ion current is collected. The same scheme can work for ion energy measurements if the collector is connected in series with a power supply, in addition to the mandatory ammeter. In this case, the ion energy distribution is the derivative of the collected current where the collector bias is the energy.

When only ions arrive to the cup, as when measuring the ion beam generated with the ion source described in subsection 3.1.2, both current and energy measurements can be carried out with only one power supply biasing the retarding aperture. The collector can remain grounded through the ammeter.

Part III.

Results

5

Fluorinated amorphous carbon thin films

5.1 Growth rate and intrinsic stress

For the sake of compactness, a magnitude $R^{gas}_{CHF_3}$ has been defined and been used all along the thesis:

$$R^{gas}_{CHF_3} \equiv \frac{\Phi_{CHF_3}}{\Phi_{CHF_3} + \Phi_{CH_4}} \tag{5.1}$$

where Φ_X is the gas flow of X.

Initially, a total gas flow ($\Phi_{CHF_3} + \Phi_{CH_4}$) of 10 sccm was used to deposit the films. However, in order to use high $R^{gas}_{CHF_3}$ and because of the minimum possible flow provided by the mass flow controllers (MFCs), the total flow was increased to the maximum available: 25 sccm. Some of the first films were deposited on in-situ previously plasma-cleaned[1] substrates but this step was abandoned after confirming that it was not necessary. More details about these processes are shown in Appendix B.1.

The growth rates for both setups, when deposited in a plasma excited using a pulsed-DC power of 56 W at a frequency of 100 kHz and with a positive pulse width of $\tau_+ = 2016$ ns, are shown on figure 5.1. Although both of them produce the films at comparable speeds and both make the rate to increase with $R^{gas}_{CHF_3}$, the linearity and stability with 25 sccm and without plasma cleaning is significantly improved. However, chemical composition does not change for both flows (see subsection 5.2.1) which points out to plasma cleaning as a possible cause for differences between both series. As for the absolute values, the growth rate is high compared to films grown also using CHF_3 as precursor gas but at higher pressures (133 Pa) and using pulsed-RF as excitation source [Winder and Gleason, 2000], or compared to other gases (C_4F_8) at pressures closer to 10 Pa (13 Pa) [Kim et al., 2005].

The introduction of CHF_3 in a CH_4 discharge has shown to lead to instabilities and history-dependant processes. During the time the plasma is on, light-emitting plasma lobes appear on the cathode, their position depending on its previous conditions. The origin of these type of instabilities is speculated but poorly understood

[1] 2.2 W/cm^2 RF, 6.0 Pa of Ar and self-bias of −530 V

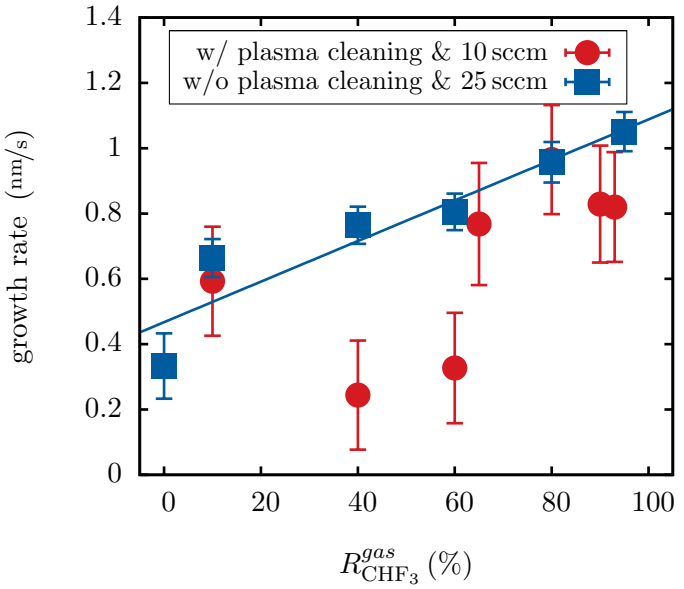

Figure 5.1.: Growth rate of fluorinated a-C thin films with (w/) and without (w/o) plasma cleaning.

in the literature [Schulze et al., 2008]. To minimize the impact of these plasma lobes on the deposition characteristics of the process, the sample holder has been cleaned with a damp wipe prior to every deposition. This procedure does not make the plasma lobes to disappear, but their positions become not fixed, and consequently, their effect is spread all over the surface of the substrate. Although the position of the plasma lobes is difficult to record or even describe, they usually move at a certain fixed distance from the center of the cathode, their trajectories globally describing circles. This is probably the cause of the annular shape observed in the homogeneity studies carried out in 2" in diameter Si wafers, which are shown in figure 5.2. For the study of growth rate, the substrates were always positioned in the center of the cathode.

With regard to the intrinsic compressive stress, the pulsed-DC excitation of the plasma provides low values but retains the high hardness characteristic, compared to RF excitation, when used with 100% methane (0.7 GPa vs 2.2 GPa). This is probably due to the pulsed characteristic of the excitation power, which allows the network to relax after every bombardment period. Figure 5.3 shows stress values for films deposited with a total flow of 25 sccm and the stress of films deposited in a similar setup with RF power excitation by Corbella [Corbella, 2006]. The introduction of CHF_3 further decreases the stress at the expense of mechanical resistance (see

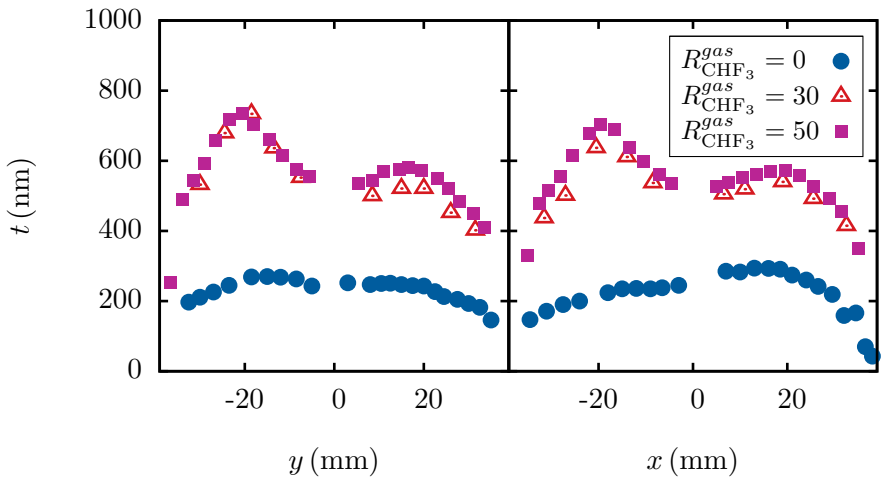

Figure 5.2.: Thickness of the films at different positions in a 2" in diameter Si wafer

subsection 5.3.4) with probably less C–C bonds. This change has already been observed in similar works [Jacobsohn et al., 2003].

5.2 Chemical composition

5.2.1. Films

XPS scans were performed on two series of samples with different values of $R^{gas}_{CHF_3}$ but the same deposition conditions. For the first series, $R^{gas}_{CHF_3}$ was: 10%, 40%, 65%, 80% and 95%, while for the second, it was: 0%, 25%, 50%, 75%, 96% and 100%. All these samples undertook a survey scan and high resolution scans of C1s and F1s. On the second series O1s peak was also analyzed at high resolution and the analysis was repeated after a gentle ion sputtering to remove surface contaminants.

The first observable feature of the survey scans on both series (see figure 5.4 for the spectra corresponding to the second series) is that only C, O and F are found on the surface. A few samples had a very small proportion ($< 1\%$) of Si or N, probably contamination from the substrate (Si) or adsorbed air molecules. In addition, after ion sputtering the films, oxygen completely disappeared, thereby proving that oxygen is exclusively present on the surface, and most likely due to air contamination.

Regarding the compositional analysis, hydrogen could not be detected, due to XPS limitations. Elemental analysis (gas chromatography of sample oxidation products) was tried, but experimental difficulties probably related to a deficient oxidation of the Si substrate invalidated the results. Therefore, only relationships between C, F

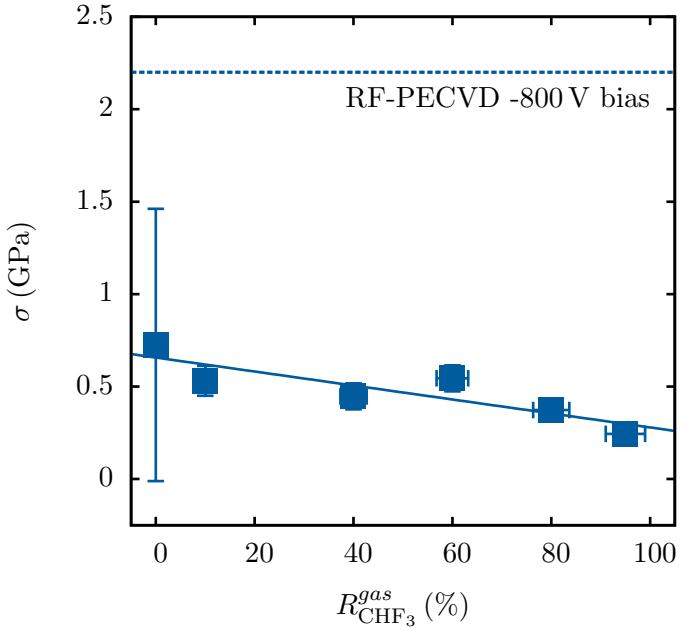

Figure 5.3.: Intrinsic compressive stress of a-C thin films with different fluorine incorporation. The dashed line corresponds to pure DLC deposited by RF-PECVD at similar conditions.

and O could be determined. Peak area, with the corresponding sensitivity factors, after background subtraction was used to obtain the relative proportions of the detected atoms in the analyzed volume. On the second series, oxygen was found to be between 7% and 10% of the total detected elements, except for highly fluorinated films (5% and 3% for $R^{gas}_{CHF_3} = 0.96$ and 1.00, respectively). On the other hand, the first series showed higher oxygen presence, with values ranging from 11% to 13% even for high CHF_3 flows (see table 5.1). Contamination O1s peak was used in all spectra (low and high resolution) to correct their energy offset.

Although some modifications aimed at the reduction of contamination were carried out in the deposition setup between both series, the difference in superficial oxygen content is attributed to an ageing effect. These modifications improved the lowest base pressure of the chamber about one order of magnitude (from 10^{-4} Pa to 10^{-5} Pa). However, compared to the deposition pressure (10 Pa) both were quite low and anyway, purity of the precursors was already about the same (N55 for CH_4; unknown for CHF_3). On the other hand, the first series underwent XPS analysis some months after being deposited, while the second one was analyzed about a week after deposition. The coverage of the surface by oxygen containing species such as water or carbon dioxide is likely to be fast during the first days but slower on the

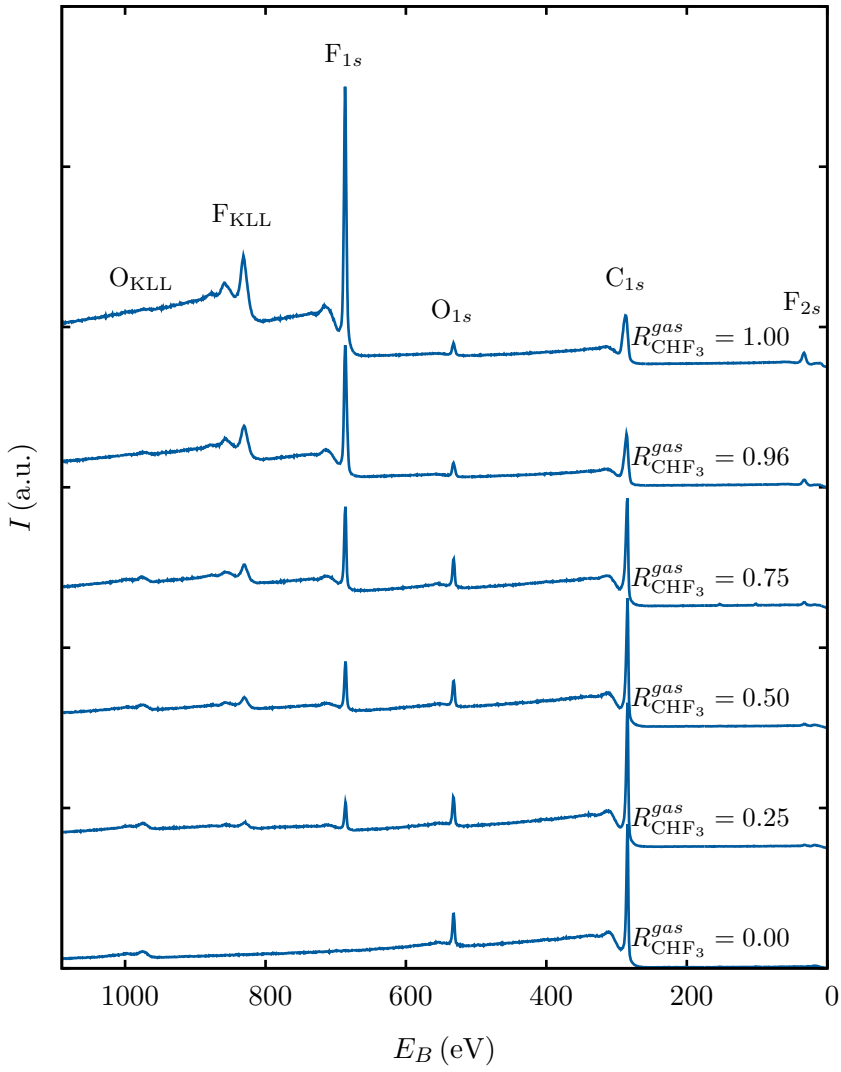

Figure 5.4.: XPS survey spectra of films with different fluorine content.

Series	Sample	$R^{gas}_{CHF_3}$ (%)	C (at.%) in bulk	F (at.%) in bulk	O (at.%) on surface
1	07A3101	10	84.5	2.0	12.9
1	07A1601	40	80.6	6.4	12.4
1	07B0501	65	76.5	12.0	10.7
1	07A1710	80	69.7	18.9	10.8
1	07A2201	93	57.6	28.3	13.0
1	07A2301	95	58.8	26.6	13.3
2	09K1201	0	90.5	0.0	9.5
2	09K1202	25	87.5	5.2	7.3
2	09K1301	50	84.3	9.2	6.5
2	09K1303	75	75.8	16.1	8.2
2	09L1501	96	58.1	36.5	5.4
2	09K1601	100	48.2	48.7	3.2

Table 5.1.: Films' composition for different $R^{gas}_{CHF_3}$ values, as per XPS.

long run. Fluorination could slow down this process to some degree. No significant ageing effect has been observed in contact angle measurements, which are sensitive to the first few angstroms of the surface (see subsection 5.3.2).

Figure 5.5 shows the evolution of fluorine to carbon ratio with $R^{gas}_{CHF_3}$. This is always lower than stoichiometric. Although for $R^{gas}_{CHF_3} = 1$, the ratio of fluorine to carbon atoms introduced into the chamber is 3, in the film only [F]/[C] = 1 is achieved. F to C ratio in the film is therefore always lower than stoichiometric. The diamond-like characteristics of the films for low $R^{gas}_{CHF_3}$ suggest that the growth mechanism is ruled by the subplantation model (see section 2.5) [Robertson, 2002; Lifshitz et al., 1989, 1990, 1994]. Under these conditions, there is an intense energetic ion bombardment which subplants energetic species, either locally increasing stress (according to McKenzie et al. [McKenzie et al., 1991]) and stabilizing diamond-sp^3 phase, or by locally increasing density which would tend to increase sp^3 bonding as well (according to Robertson [Robertson, 1993]). In any case, ion bombardment causes the loss of hydrogen and fluorine from the surface and subsurface.

Ion bombardment is carried out by positively charged species that are accelerated in the plasma sheath towards the sample. At low $R^{gas}_{CHF_3}$, fluorine (and probably hydrogen) incorporation into the film is low while for low methane concentrations the F:C ratio rises significantly. The high hydrogen content provided by CH_4 probably etches away fluorine atoms back to the plasma, which fits with OESA results for

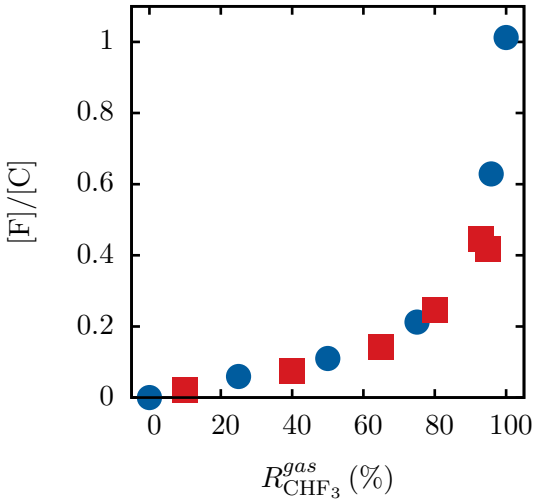

Figure 5.5.: Atomic F to C ratio in the film as determined from XPS analysis for two series of samples (deposited with 10 sccm of total gas flow, red squares; and 25 sccm blue circles).

atomic F shown in subsection 5.2.2. For a-C:H films, it is believed that atomic H, either neutral or ion, reacts with C–H bonds, abstracting H and creating H_2. According to the results of this thesis, when fluorine is added, atomic H probably reacts with F in the film creating volatile HF.

As $R^{gas}_{CHF_3}$ is increased, hydrogen introduced as part of the feed gas is reduced and, eventually, fluorine content in the films starts to increase. Therefore, the reduction of atomic hydrogen increases the chance of fluorine to remain in the film. Fluorine, the substitute of hydrogen when $R^{gas}_{CHF_3}$ is increased, does not produce the same effect as H, due to its strong electronegativity and, therefore, absence of bombarding F atoms.

In addition, ion energy measurements[2] have shown that the progressive substitution of CH_4 by CHF_3 reduces, and finally eliminates, the population of high energy ions [Corbella, 2009]. The combination of hydrogen reduction, exchange by a strong electronegative atom (F) and reduction of the density of energetic ions bombarding the growing surface, would explain the non-linear increase of [F]/[C].

Deconvolution of C1s peak

The results of the C1s band analysis for the different spectra are shown in figure 5.6. Spectra are normalized in area according to the ratio of carbon over all detected elements and the energy offset is corrected by fixing the contamination O1s peak

[2]This experiment was performed at a higher pulsed-DC frequency because of measuring equipment limitations.

at 532.0 eV for all spectra. The contribution of the different peaks to the C1s band approximately correspond to those computed from the survey spectra. The main features of the spectra deconvolution follow.

C–C / C–H peak is divided in two parts: sp^2 and sp^3 hybridization. Electrons in atoms with sp^2 hybridization are about 0.9 eV less energetic than sp^3. This is due to the slightly shorter bond length of sp^2 sites than sp^3, so that the former experience a slightly deeper potential than the latter [Robertson, 2002]. In the current analysis, sp^2 peak corresponds to a binding energy of 284.3 ± 0.1 eV, while sp^3 peak is at 285.3 ± 0.1 eV. sp^3/sp^2 ratio for films deposited with $R^{gas}_{CHF_3} = 0$ is about 0.2, which, although being a reasonable value for hydrogenated a-C (see figure 2.1), it is lower than expected considering the measured wear resistance and roughness of the films deposited with pure methane. As will be discussed later, the amount of peaks close in energy approximately from 284 eV to 287 eV reduces the deconvolution reliability, what could account for this discrepancy.

C–O and C=O peaks appear at 286.5 eV and 288.0 eV (yellow and cyan in figure 5.6, respectively). Their position does not change with $R^{gas}_{CHF_3}$ because they are associated to contaminants and the effect of the chemical environment on these bonds is limited.

Regarding fluorinated bonds, $C - CF_x$ peak appears at 286.55 eV (green in figure 5.6) for $R^{gas}_{CHF_3} \gtrsim 0.25$. At $R^{gas}_{CHF_3} = 0.5$ is maximum, and from there on it decreases again. These bonds correspond to C–C bonds with a slightly fluorinated environment. CF_x peaks can be detected for films deposited with $R^{gas}_{CHF_3} = 0.5$ but at this flow ratio, only CF and CF_2 are significant (and still very small). For higher fluorination degrees CF_x peaks increase with $R^{gas}_{CHF_3}$. The positions of CF_3, CF_2 and CF peaks for $R^{gas}_{CHF_3} = 1$ are 292.0 eV, 289.8 eV and 287.8 eV. These positions, relative to C–C/C–H, are in agreement with reviewed XPS data of fluoropolymers [Nansé et al., 1997]. Compared to films deposited with pure CHF_3, for $R^{gas}_{CHF_3} = 0.96$, CF_x peaks experience a strong reduction in energy and then, for lower fluorination degree, a slow decrease until their presence is not significant (see dashed line in figure 5.6). This shift is probably associated to a deficient bond formation in the low fluorine content films or to the influence of a more fluorinated environment around the carbon bonds, which would increase their binding energy due to fluorine's high electronegativity. This hypothesis is confirmed in the literature by XPS studies of fluoropolymers where it was found that fluorine, due to its large electronegativity and small volume, presents important intermolecular neighbouring effects absent in the case of other atoms [Ferraria et al., 2003].

The high number of parameters needed to fit the spectra reduces the deconvolution reliability. However, fluorine electronegativity shifts C1s emission far more than oxygen or other elements, allowing to clearly distinguish the presence of CF_2 and CF_3 bonds, and providing good confidence about their evolution, if they are significant in the spectra. The strong increase of CF_3 between $R^{gas}_{CHF_3} = 0.96$ and 1 is in good agreement with the observed decrease in surface energy (see subsection 5.3.2). Also, the observed reduction of atomic fluorine in the plasma by OESA (see figure 5.9),

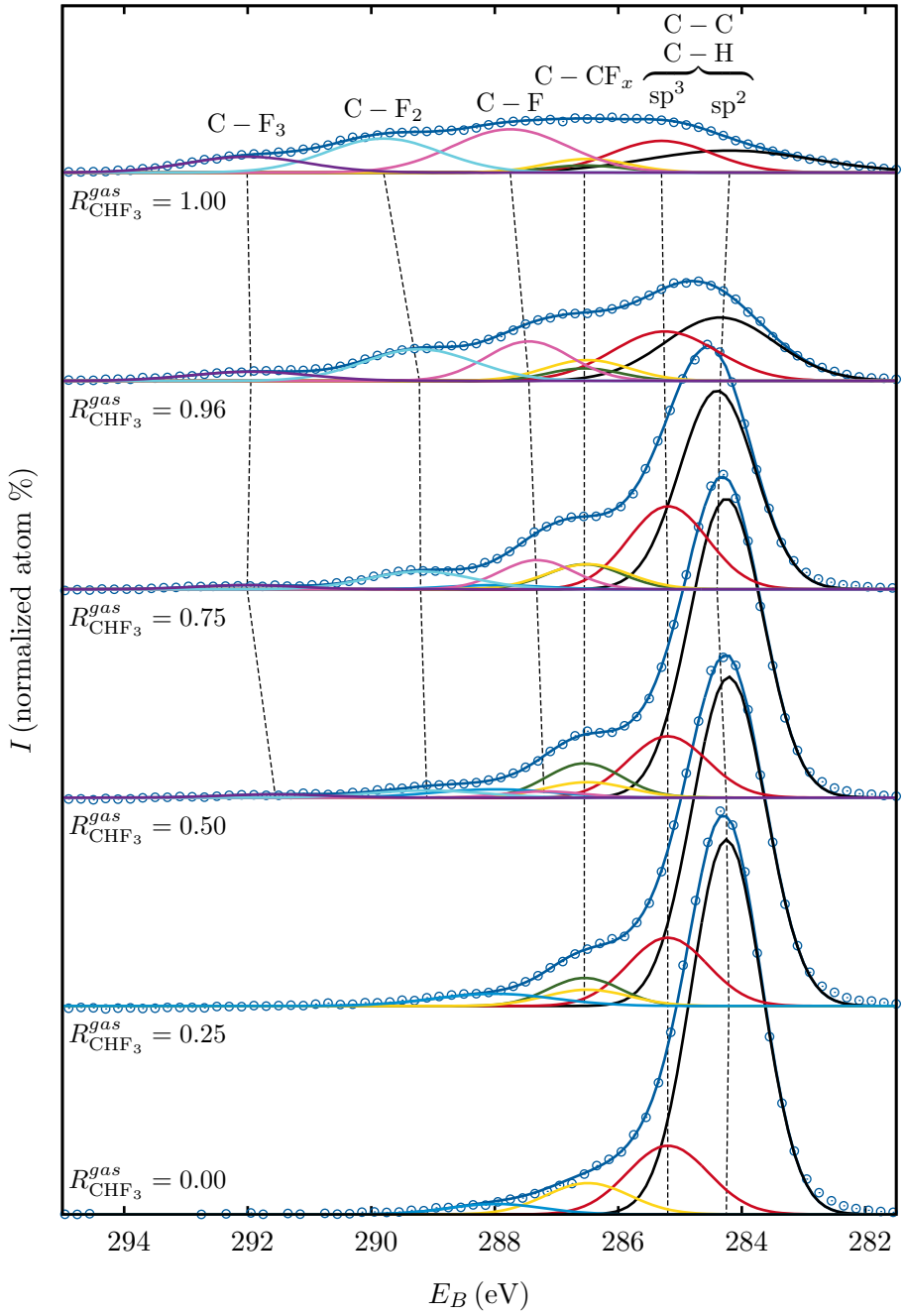

Figure 5.6.: C1s XPS spectra of films. Black: C–C/C–H sp^2, red: C–C/C–H sp^3, yellow C–O, blue C=O, green C – CF$_x$, pink CF, cyan CF$_2$ and violet CF$_3$.

probably caused by the reduction of hydrogen bombardment on the film, could be the cause of CF_3 bonds increase.

The total contribution of C–C/C–H (both sp^2 and sp^3) and $C - CF_x$ bonds to the film is reduced as more CHF_3 is used to grow the film. The degree of cross-linking in the film is related to these bonds, so that a reduction in cohesion of the DLC network is to be expected [Butter et al., 1997]. This is experimentally supported by the abrasive wear tests and surface energy calculations (see sections 5.3.2 and 5.3.4). Also, the reduction in cross-linking emerges as stress reduction (see section 5.1).

5.2.2. Plasma

In order to determine how the plasma's chemical composition is related to that of the film, optical emission spectroscopic actinometry (OESA) analysis were carried out for the same conditions as those for film deposition on eleven different CHF_3 concentrations. As detailed in section 4.7, actinometry requires the addition of a small quantity of inert gas to the plasma in order to refer the measured optical intensities to it. If the quantity of actinometer is too big, the plasma characteristics could change. On the other hand, the smaller the quantity introduced, the larger the error on the measurements, due to the reduced emission of Ar lines.

In order to have an idea of the extent of plasma modification with the introduction of Ar, the intensity of F, CF_2 and Ar lines were monitored for different Ar gas flows. The result of this experiment is shown in figure 5.7. Two different flows of Ar were added to the plasma, 0.5 sccm and 1.0 sccm, the former being the minimum flow provided by the MFCs. The addition of Ar to a mixture of CH_4 and CHF_3 did not add new lines to the emission spectrum, other than that of Ar, although a small increase in the emission intensity of CF_2 and CHF was observed. The main emission line of Ar did not increase significantly between both flows, so the minimum available was chosen (0.5 sccm).

Raw spectra for actinometry are shown in figure 5.8, while the evolutions of each line, referred to Ar, with respect to $R^{gas}_{CHF_3}$, is shown in figure 5.9.

In subsection 5.2.1, a qualitative model for film's growth and plasma processes is described. The dependence of I_F/I_{Ar} on CHF_3 supports this model. According to it, part of the already deposited fluorine is abstracted by atomic H and returned to the plasma as HF where it can be dissociated again. Note that emission of HF in the visible range has not been resolved. HF has been reported to emit a multi-line system on the UV ($200 - 267$ nm) and two bands at 669 nm and 867 nm, whereas HF^+ has a band on $358 - 483$ nm [Pearse and Gaydon, 1976]. No emission has been observed on the red range, although the UV and blue bands could be part of the big CF_2 band. Anyway, the absence of emission can be due to a number of reasons: low cross section, absence of electrons with suitable energy, low emission efficiency, fast dissociation of HF in the plasma or physisorption and return to the plasma once dissociated again.

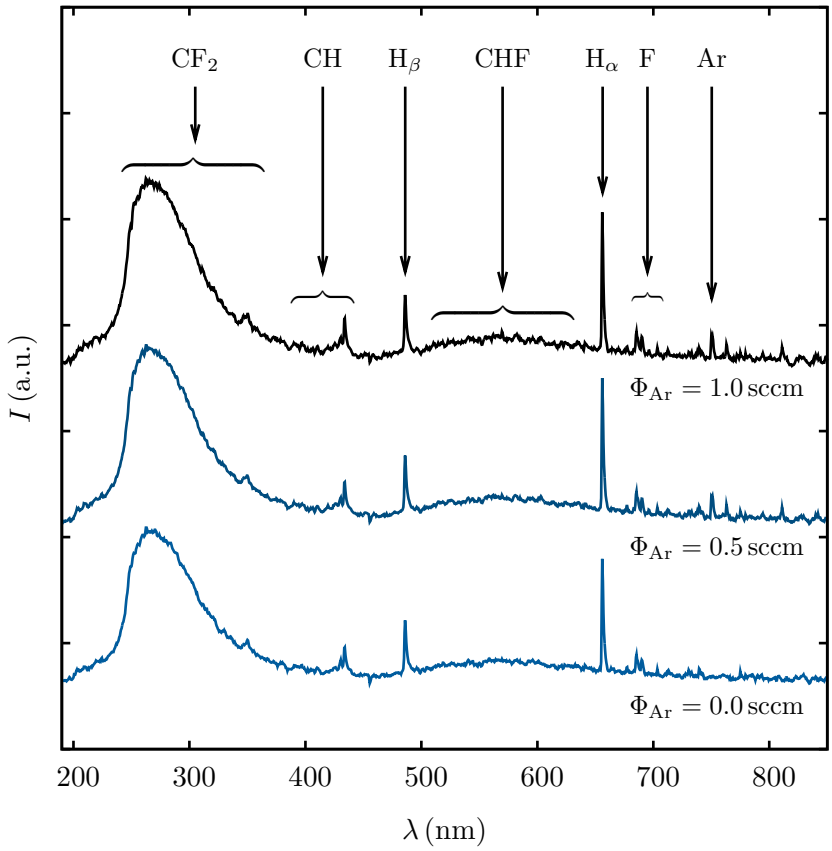

Figure 5.7.: Optical emission intensity of CF_2, Ar and F peaks as a function of absolute Ar flow. Ar does not significantly change the emission intensity of the other species.

Initially, total fluorine content in the plasma is low and hydrogen content high. According to actinometry results, atomic F (I_F/I_{Ar}) increases with $R^{gas}_{CHF_3}$ when methane is the main precursor. However, as more CHF_3 is introduced in the chamber, hydrogen content decreases and at some point (between $R^{gas}_{CHF_3} = 0.4$ and 0.7), atomic F starts to decrease, due to the reduced bombardment.

Atomic H_α line decreases linearly with $R^{gas}_{CHF_3}$. Fitting of a line to data, weighting points with their corresponding errors, results in the following expression:

$$\frac{I_H}{I_{Ar}} = 5\left(4.0 \pm 0.2 - (3.0 \pm 0.2) R^{gas}_{CHF_3}\right)$$

In addition, if actinometry is valid, this ratio of intensities should be proportional to the density of atomic H in the plasma. Considering that total hydrogen introduced

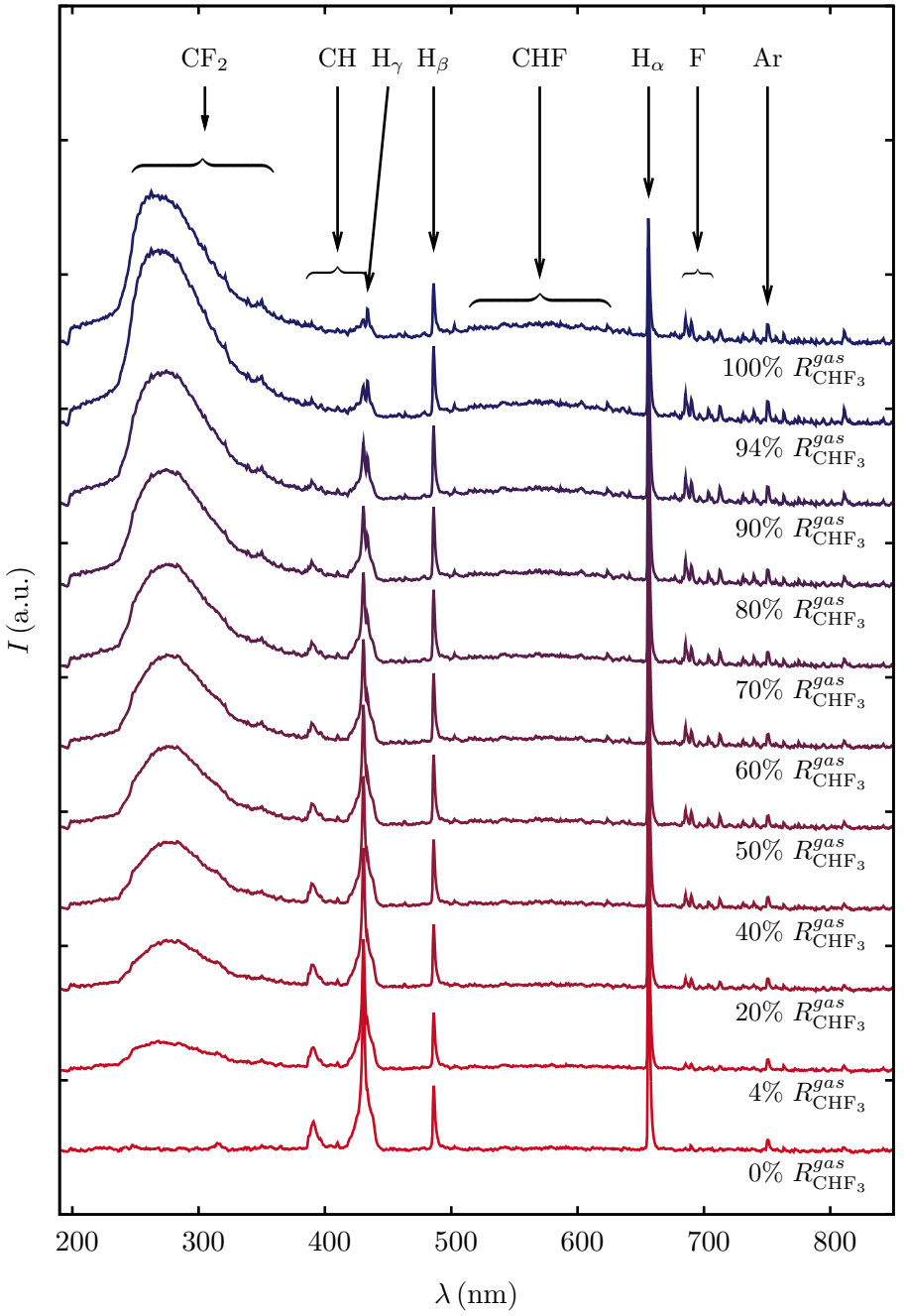

Figure 5.8.: Plasma's optical emission spectra with argon as actinometer

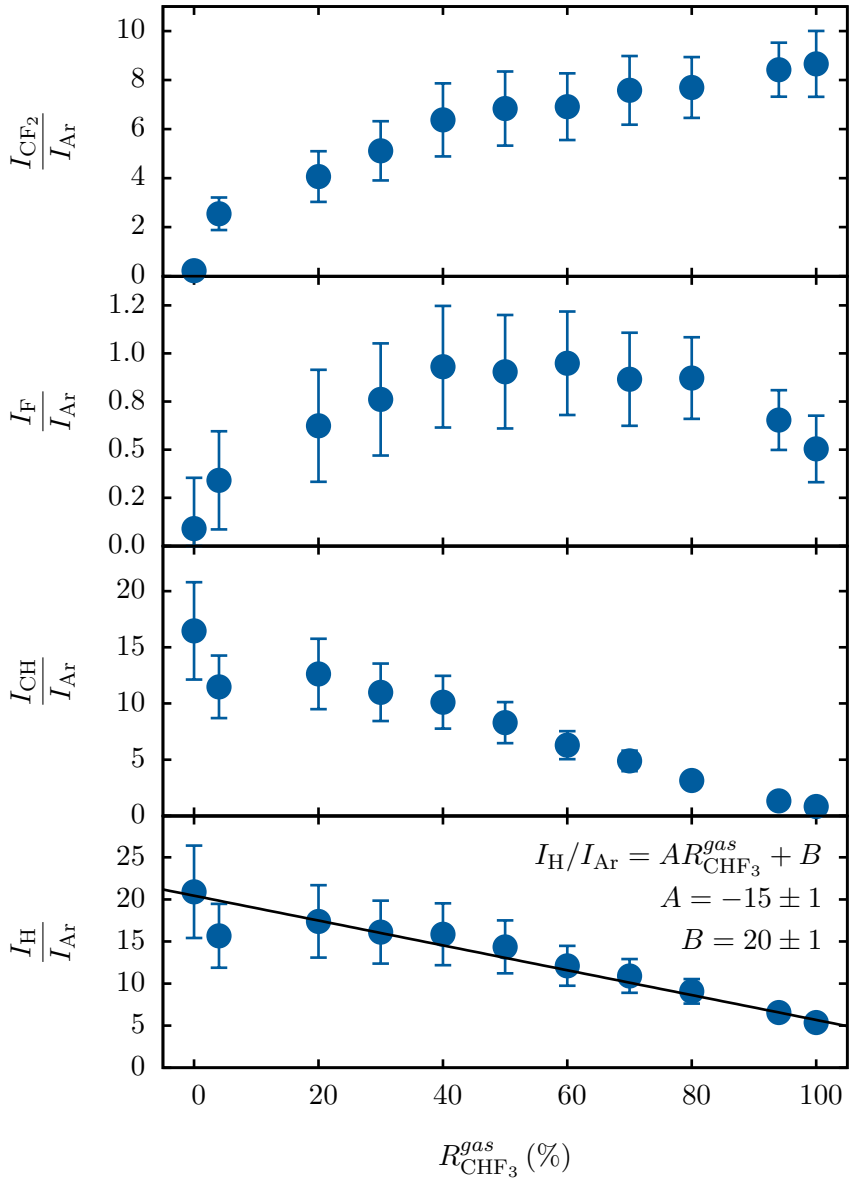

Figure 5.9.: Actinometry figures of CHF_3, F, CH and H. Concentration vs presence of CHF_3.

Dissociation	ΔH (eV)
$CHF_3 + e^- \rightleftharpoons CF_2 + HF + e^-$	2.4
$CF_3 + e^- \rightleftharpoons CF_2 + F + e^-$	3.8
$CHF_3 + e^- \rightleftharpoons CF_3 + H + e^-$	4.5
$CHF_3 + e^- \rightleftharpoons CHF_2 + F + e^-$	4.9

Table 5.2.: Dissociation energy for different reactions [Truesdale and Smolinsky, 1979]

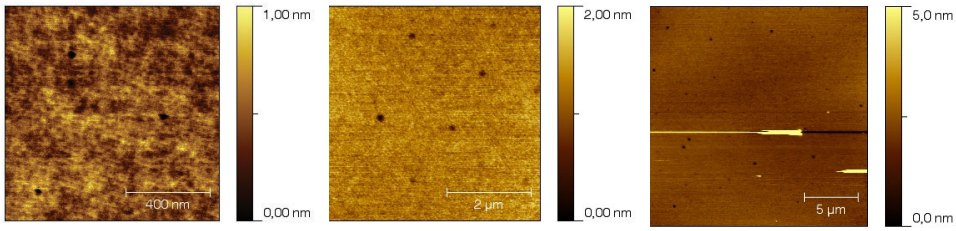

a) b) c)

Figure 5.10.: AFM topography images of sample 08G0201 at different scales

in the plasma is proportional to $4-3R^{gas}_{CHF_3}$, it follows that the fraction of all hydrogen that is in atomic form does not depend on the gas mixture.

On the other hand, CH line also presents a linear evolution, but in this case the value for $R^{gas}_{CHF_3} = 1$ is very close to zero. C–F bonds are stronger than C–H by approximately 45%, [Lide, 2005] so that dissociation of a fluorine atom from CHF_3 is less probable than a hydrogen atom. On every dissociation step, the accumulated probability of loosing the H atom increases. CH species are therefore only generated from methane.

5.3 Surface characteristics

5.3.1. Roughness

The RMS roughness of seven films was measured by statistical analysis on topography images taken by AFM. Each of the seven films were deposited using plasmas with varying concentrations of CHF_3 in CH_4. The images for the sample deposited in pure methane are shown in figure 5.10, while the roughness values are plotted in figure 5.11.

Roughness has been measured at different scales, ranging from 1 µm to 20 µm. In order to obtain the intrinsic value for the films, defects such as particles or dust

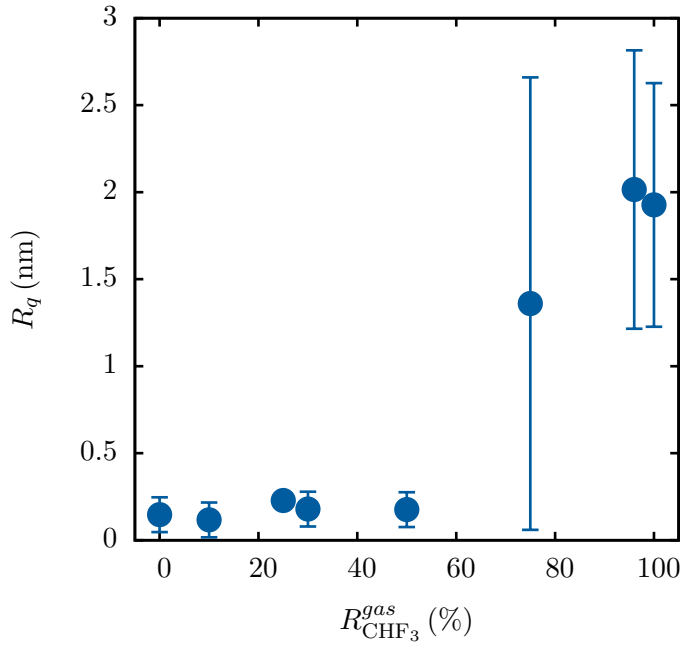

Figure 5.11.: RMS roughness (R_q) of films after removing eventual defects or dust.

have been excluded from the analysis. These defects are present in the surface of the film, maybe not because of the technique itself, but because its implementation and the available equipment in our laboratory. However, as more fluorine is present on the films, roughness increases and it is more difficult to distinguish such defects from the film. This is the reason to the increased deviation of measurements for films with more fluorine.

The measured roughness is low for films with a low fluorination degree, with values ranging from about 0.1 nm to 0.2 nm. On the other hand, for films deposited with $R^{gas}_{CHF_3} > 0.5$, roughness is highly increased to about an order of magnitude over the rest.

A smooth surface is a characteristic property of hard amorphous carbon films, which being amorphous (i.e.: no grain boundaries), meet the first important requirement. To obtain a smooth surface, the growing layer must nucleate everywhere on the substrate surface, and carbon species must have enough energy so that their mobility is low and they do not move to form islands, leaving parts of the surface uncovered. Therefore, a deposition flux with a high fraction of energetic species (> 10 eV) is needed, to overcome any nucleation barrier. Moreover, when the growth is subplanted, species cannot move over the surface to reduce surface energy [Robertson, 2002].

As discussed in subsection 5.2.1, there is evidence that ion energy could be decreasing as more CHF_3 is used in the precursor mixture, what would be consistent with the increase in roughness. Also, the substitution of hydrogen by fluorine in the precursor could result, not only in hydrogen's content reduction in the film, but also in a higher fraction of fluorine for $R^{gas}_{CHF_3} = 1$ than hydrogen was for $R^{gas}_{CHF_3} = 0$. That is, fluorine could incorporate more easily to the film when pure CHF_3 is used, than hydrogen for pure methane, due to the reduced ion bombardment. This would cause a loss of cross-linking and, maybe, a lower film density, which could induce nucleation and increase roughness.

5.3.2. Surface energy

Contact angles of different liquids were measured on almost all films. Time between deposition of film and measurement of wettability ranged from a few hours to some weeks for films deposited with up to $R^{gas}_{CHF_3} = 0.8$. No significant correlation was observed between these two parameters (no ageing), indicating a stable and probably highly cross-linked structure of the films that would reduce the mobility of surface groups.

Figure 5.12 shows all collected contact angles. All liquids experience lower wettability as $R^{gas}_{CHF_3}$ is increased, but from 0.8 on, the increase of contact angle is produced at a much faster pace.

The change of trend is even more distinguishable on surface energy (SFE, γ_s) calculated by solving equation (4.12) (see figure 5.13). Films deposited with CHF_3 over 80% show very low values, the most fluorinated film exhibiting slightly lower surface energy than PTFE: $17\,mJ/m^2$ on VOCG scale (figure 5.13a) and $14\,mJ/m^2$ on DVS (figure 5.13b), versus $18\,mJ/m^2$ for PTFE. Regarding the different components, Lifshitz-Van der Waals' is the dominant, due to the low value of acidic component (γ^+), as acid-base component is calculated as the geometric mean of acidic and basic interactions. This situation changes for the two most fluorinated films on VOCG scale, for which both acid-base components are little but significant and so they contribute to SFE. Basic component (γ^-), presents a clear decreasing evolution with $R^{gas}_{CHF_3}$ on both scales, becoming almost zero for high CHF_3 ratios.

Contact angle measurements and SFE calculation was also performed for bare polished silicon. No oxide-stripping procedure was carried out before the measurements so, according to contact angle sensitivity (about 5 nm), this data probably corresponds to a mixture of silicon and the native oxide layer (about 1.5 nm thick). According to calculations on the original VOCG scale, pure DLC (no fluorine) films' total surface energy is the same as of silicon. As more CHF_3 is used, film's total SFE decreases, as well as its LW and basic components. On the other hand, DVS scale provides a value for silicon's SFE closer to literature and $R^{gas}_{CHF_3} \gtrsim 0.8$ is needed in order to obtain films with less surface energy than silicon [Zhuang and Hansen, 2009]. However, both scales provide close values for total SFE, LW and acidic components,

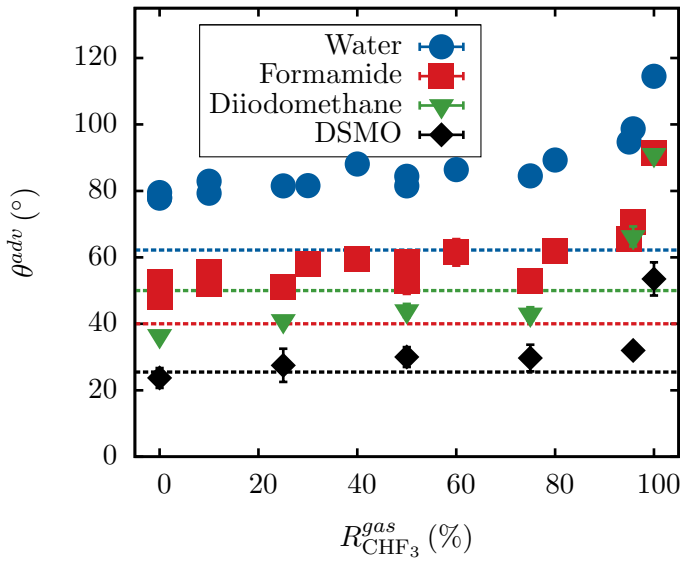

Figure 5.12.: Advancing contact angle values of different liquids. Dashed lines correspond to the liquids on bare silicon.

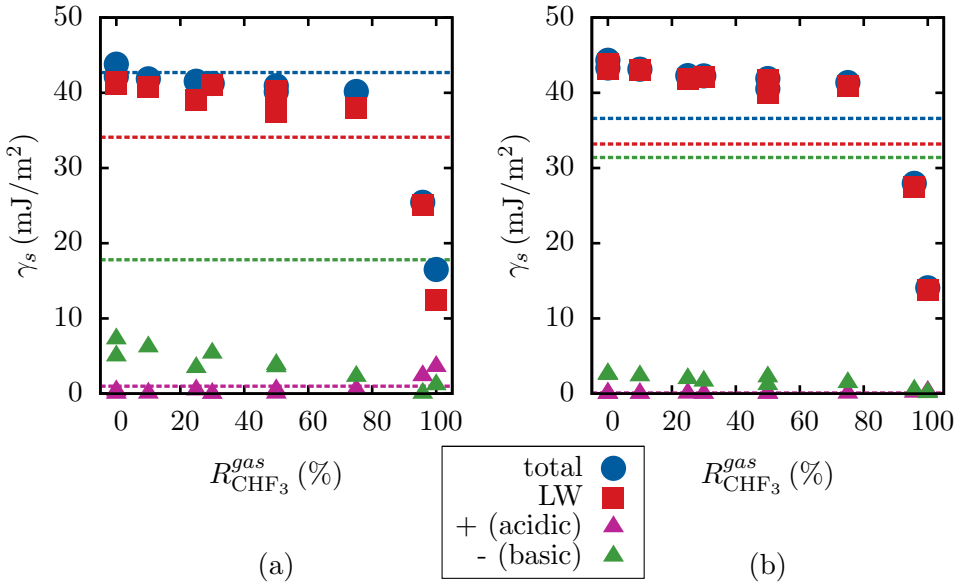

Figure 5.13.: Surface free energy calculations of films and silicon (dashed lines), according to VOCG theory with the original scale (a) and the alternative DVS scale (b).

Surface constitution	γ_s ($\frac{\text{mJ}}{\text{m}^2}$)
$-CF_3$	6
$-CF_2H$	15
$-CF_2-$	18
$-CH_3$ crystal	22
$-CH_3$ monolayer	24
$-CH_2-$	31

Table 5.3.: Critical surface tensions of selected groups [Zisman, 1964].

with similar evolution for basic component. This supports the basic characteristic of the surfaces.

Also both scales show that silicon has high basic component. Acid-base components are a measure of the surfaces' ability to create complexes with liquids. For UV-NIL applications, inert surfaces are sought, because UV light activates some reactions between mold and polymer. For example, siloxane bonds found in common mold's surface treatments based on $F_{13} - TCS$ (see section 1.4) react with most polymers when exposed to UV radiation [Houle et al., 2007].

Pure DLC has already been suggested as an alternative to self-assembled monolayers for this particular application, due to its inertness, absence of siloxane bonds and inherent smooth surface [Houle et al., 2007]. Fluorinated DLC would have similar advantages with even higher inertness, due to the reduction in acid-base, interactions. According to Wu [Wu, 1982], sharp interfaces of materials with low polar components and dispersive dominated SFE, provide low adhesion, whereas a diffuse interface would provide good adhesion. The high contribution of the LW component to the SFE should therefore be beneficial for the purposes of an anti-sticking coating.

For $R^{gas}_{CHF_3} \gtrsim 0.8$, films exhibit much lower SFE, due to the strong reduction in LW component, which is probably related to both a change in structural properties of the films and incorporation of low energy groups to the film. XPS results (subsection 5.2.2) have shown that the very low surface energy CF_3 groups (see table 5.3) are mainly incorporated in the film for $R^{gas}_{CHF_3} = 0.96$ and 1. On the other hand, a probable reduction in cross-linking degree occurs for high fluorination degrees ($R^{gas}_{CHF_3} \gtrsim 0.8$), which is supported by wear measurements, detailed in section 5.3.4.

According to Zisman's critical surface tension measurements (see tables 5.3 and 5.4), surfaces termination of the low fluorinated films should include more carbon atoms than hydrogen or fluorine. Surface energy of surfaces with only carbon, hydrogen and fluorine does not reach that of the deposited films. Therefore, adsorbed oxygen molecules could be playing some role, by acting as high energy groups. On

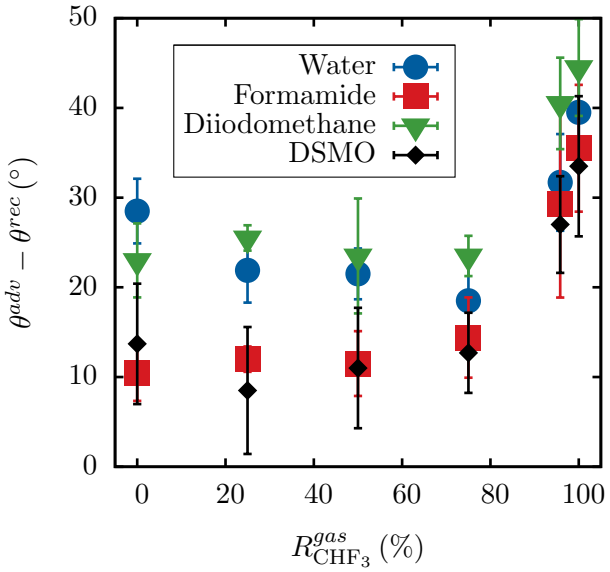

Figure 5.14.: Contact angle hysteresis for different liquids on the deposited films.

highly fluorinated films, XPS results showed that oxygen presence on the surface was lower. This reduction could account for the reduced surface energy. However, the same results indicated that approximately the same amount of fluorine and carbon was present on the most fluorinated film. According to table 5.4, there is no fluorinated polymer exhibiting such low energy with [C] = [F]. This could mean that the deposited films have higher fluorine content in the surface. Anyway, the deposited films have a low surface energy with a higher degree of cross-linking than polymers.

Figure 5.14 shows contact angle hysteresis values for different liquids on the films. Contact angle hysteresis is the measure of energy dissipation during the flow of the interface. The exact reasons for contact angle hysteresis are not known, although it is clear that it is related to surface heterogeneity and roughness at various scales. The dissipation may occur in the bulk of the liquid, in the solid/liquid interface (contact area) or in the liquid/solid/gas interface (triple line). The quasi-static case removes the dissipation in bulk, which is due to the liquid's viscosity. However, the contact area dissipation (due to the so-called adhesion hysteresis), and the triple line interactions (due to roughness) depend on the particular sample [Nosonovskii and Bhushan, 2008].

Roughness measurements shown in subsection 5.3.1 stated that the deposited samples are extremely smooth, with RMS values below 0.3 nm for films with a low fluorination degree. For this set, triple line interactions probably constitute a small but not negligible contribution to hysteresis, as defects, probably not inherent to the

Polymer	Structural formula	γ_s ($\frac{\text{mJ}}{\text{m}^2}$)
Polytetrafluoroethylene (PTFE)	$-\text{CF}_2-\text{CF}_2-$	18
Polytrifluoroethylene (PTrFE)	$-\text{CHF}-\text{CF}_2-$	22
Polyvinylidene fluoride (PVDF)	$-\text{CH}_2-\text{CF}_2-$	25
Polyvinyl fluoride (PVF)	$-\text{CH}_2-\text{CHF}-$	28
Polyethylene (PE)	$-\text{CH}_2-\text{CH}_2-$	31
Polyvinyl chloride (PVC)	$-\text{CH}_2-\text{CHCl}-$	39
Polyvinylidene chloride (PVDC)	$-\text{CH}_2-\text{CCl}_2-$	40

Table 5.4.: Critical surface tensions of halogenated polyethylenes [Zisman, 1964].

deposition technology, were ignored in roughness calculation. Therefore, adhesion hysteresis would probably be the dominant dissipation mechanism. However, for films deposited with $R^{gas}_{CHF_3} > 0.5$, and more importantly as $R^{gas}_{CHF_3}$ approaches 1, triple line interactions could overcome adhesion hysteresis. Also, the increased plasma instabilities and the reduced homogeneity (see section 5.1) would account for the increase of contact angle hysteresis at high $R^{gas}_{CHF_3}$.

5.3.3. Friction

Several factors influence the frictional behavior of DLC thin films [Erdemir and Donnet, 2006]: the degree of sp^2 or sp^3 carbon bonding, the amount of hydrogen in the film, the eventual alloying elements, the chemical, and mechanical interactions between film and ball, the ball composition or the film and ball roughness. Moreover, the sliding conditions of speed and load [Heimberg et al., 2001] or debris production can also determine the possible interactions in the experiment. The interpretation of friction data is therefore not straightforward.

Friction tests were carried out in ball-on-disk configuration, as detailed in section 4.2, during 6250 cycles in a $N + H_2O$ atmosphere, with a linear speed of 1 mm/s and applying 50 mN of normal load. These parameters resulted in a total track length of about 31 m. The selected sliding counterpart was a 3 mm in diameter ball of tungsten carbide. Relative humidity (RH) was controlled by means of the setup described in subsection 4.2.2. Raw data of friction tests on a film without fluorine are shown on figure 5.15.

Regarding debris production, a statistical analysis of 50× micrographs, taken after the tests, has been carried out to determine the extent of its influence in friction (see figure 5.16a). Only high friction tests have shown a clear relation with debris production, while for the rest, both macroscopic and molecular phenomena at different scales are coupled (tests with similar debris production have different frictions and the other way round) and must be taken into account. Also, as seen in subsection 5.3.1, roughness is sufficiently low so that it is a minor factor in friction phenomena for the tested $R^{gas}_{CHF_3}$ range), not producing interlocking and/or asperity-asperity interactions during sliding.

The most significant feature of friction, whose measurements are shown in figure 5.17, is the reduction of friction coefficient value for increasing relative humidity. The reduction takes place for humidities between 20% and 60%, whereas beyond that point, it does not suffer significant variation. Moreover, for high RH, friction does not seem to depend on the fluorination degree of the films.

Regarding the effect of fluorine introduction, non-fluorinated films provide, on average, the lowest friction, while films deposited with $R^{gas}_{CHF_3} = 10\%$ show the highest friction (0.4 for 20% RH). For higher F concentrations friction coefficient is reduced again. Low-fluorinated films see their friction more affected with humidity than non-fluorinated or highly-fluorinated DLC films.

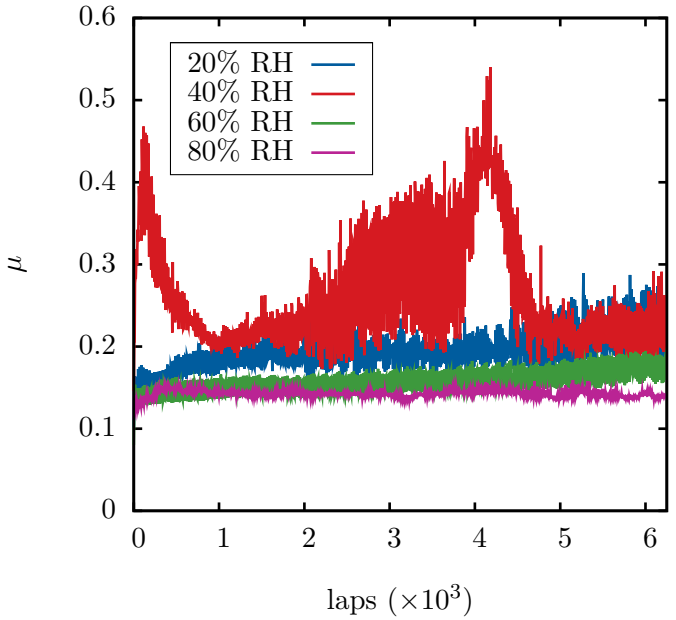

Figure 5.15.: Raw data of μ during the different tests for 08G0201 ($R^{gas}_{CHF_3} = 0$, 56 W, 100 kHz, $\tau_+ = 2016$ ns)

Optical microscope photographs (see figure 5.16b) show fiber-like debris particles at both sides of the sliding track. According to Erdemir and Donnet [Erdemir and Donnet, 2006], this phenomenon occurs when discontinuous wear is given contrary to what happens when a transfer layer is present between the sliding counterpart and the film surface.

Hydrogen terminated surfaces provide low friction characteristics due to the passivation of σ and π carbon bonds on the surface [Erdemir and Donnet, 2006]. As the WC ball slides over the surface, H atoms are mechanically removed from the film by strain effects [Li et al., 2005] thus leaving superficial dangling bonds. Depending on the experimental conditions, and specifically on the gas environment, hydrogen and hydroxyl groups originated from water will passivate these bonds again. In our experiment, for relative humidities between 20% and 60% the results would justify this casuistic, so that bonds would react with water to restore themselves to a low energy state. However, for higher presence of water (from 60% to 80%), friction is stabilized for all films and independently of humidity or fluorine content. For these values of RH, a layer of physisorbed water could be formed on the surface, as already suggested by other authors [Erdemir and Donnet, 2006; Erdemir, 2001], which would make friction independent of the films' variations.

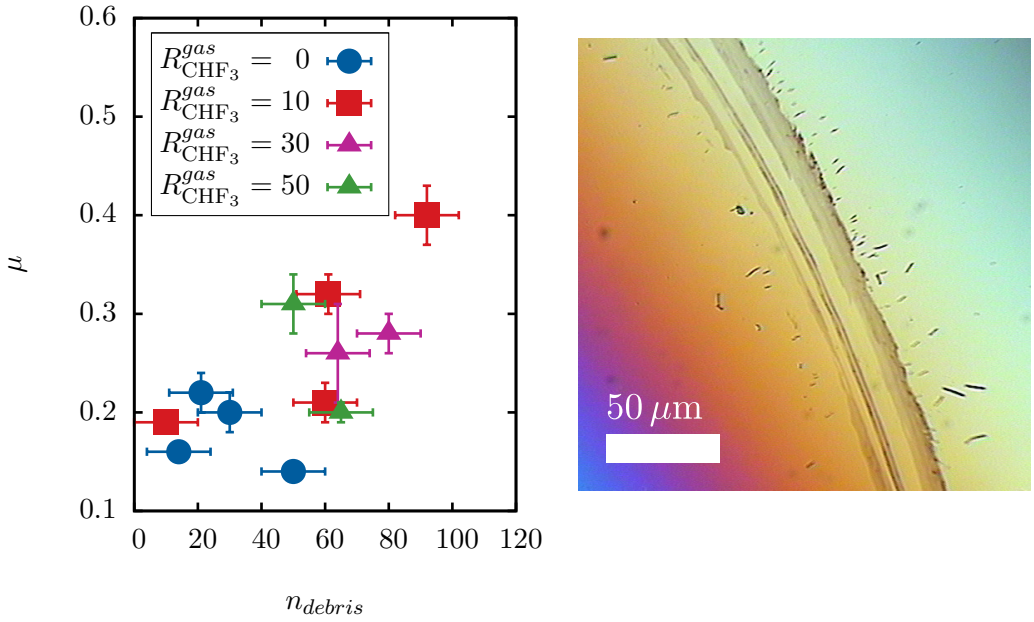

Figure 5.16.: a) Friction vs number of debris particles visible at 50× (200 × 200 µm). The dependence of friction with number of particles is only clear for high friction values; b) 50× optical microscope picture of a typical sliding track, corresponding to a film with $R^{gas}_{CHF_3} = 10\%$ measured at 60% RH. Fiber-like debris particles are present at both side of the sliding track.

Regarding the rather high friction values for $R^{gas}_{CHF_3} = 10\%$ in comparison to the rest, this behavior could be due to at least two competitive mechanisms. One of them would be the somewhat beneficial effect of F presence to reduce friction by reducing adhesion to the sliding counterpart and by passivating carbon with a high-energy bond. The other would be the disadvantageous effect of a lower C atomic density (F is bigger than H), the reduced reservoir of H inside the film that would otherwise relink dangling bonds on the surface, and the probable decrease of H in the film as expected from OES measurements (see subsection 5.2.2). The increase of friction with fluorine for humidity values below 40% is in agreement with other analogue works [Gilmore and Hauert, 2001].

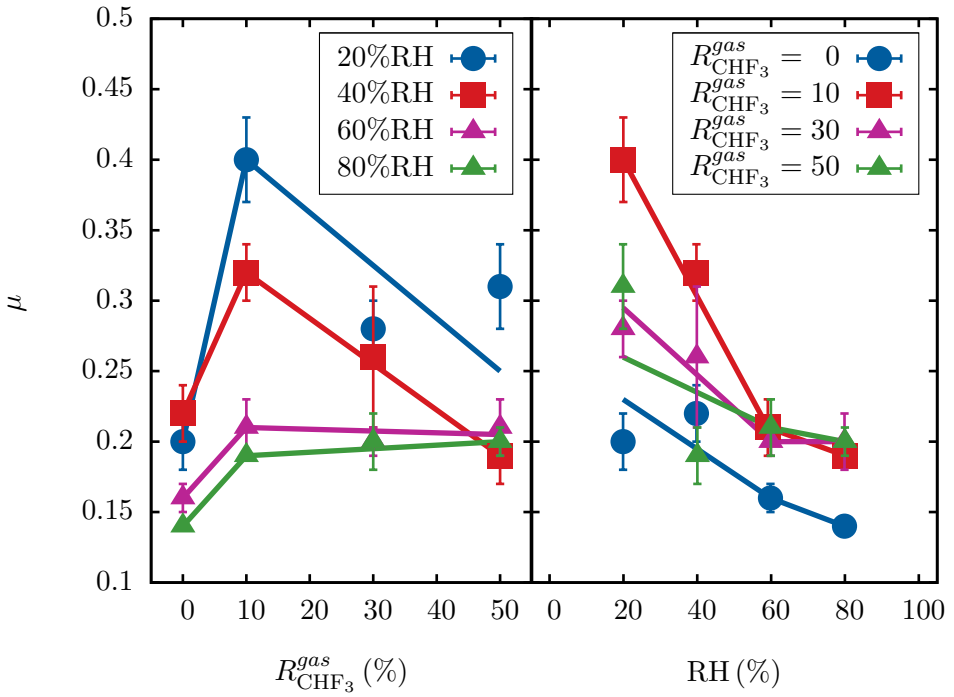

Figure 5.17.: Friction on increasingly humid environments

5.3.4. Wear resistance

Abrasive wear measurements were carried out with a 1:3 suspension of alumina particles 1 µm in diameter in glycerin. Such setup is highly hygroscopic and minimum changes in ambient humidity can affect the results. For this reason, all measurements were done during a short period of time, at 23°C and at relative humidity values about 33%. Two different balls with equal diameter were used to test the wear resistance: a steel ball applying a force of 0.54 N and a plastic (polyacetal) ball producing 0.092 N of normal load. Although both load (F) and time (through the sliding distance, s) are taken into account when calculating the wear rate (W):

$$W = \frac{V}{s\,F}$$

(see section 4.3 for more details), measurements showed an increase in the wear rate with test time, maybe due to the absorption of water by the suspension.

Figure 5.18 shows the measured values for different films, when tested for 6 min with a steel ball. The deposited films showed high wear resistance up to $R^{gas}_{CHF_3} = 0.8$, with values in the range of 0.2×10^3 µm^3/Nm to 0.4×10^3 µm^3/Nm, while for Si it was

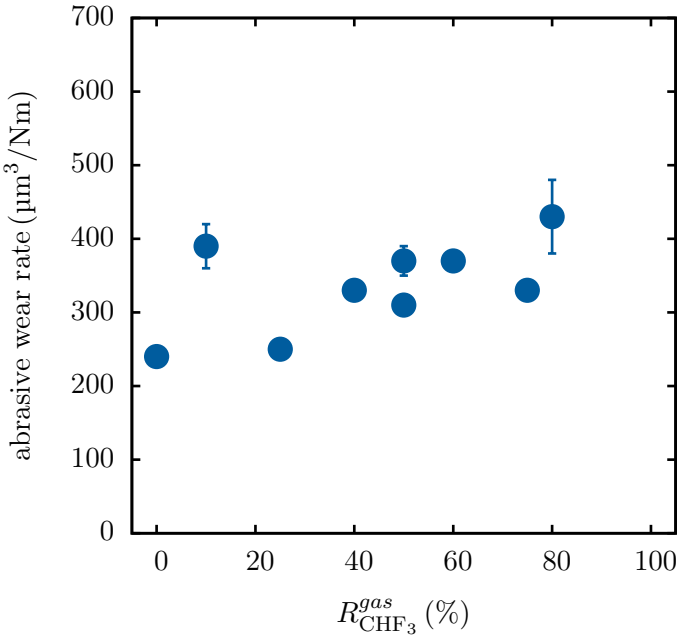

Figure 5.18.: Abrasive wear rate of the films after 6 min with a 1:3 suspension of alumina particles 1 µm in diamater in glycerin, with a load of 0.54 N.

was measured to be $(2.1 \pm 0.2) \times 10^3\,\mu m^3/Nm$; one order of magnitude less resistant than FDLC films. The wear resistance is slightly increased with fluorine content, consistent with the observed changes in composition and structure. It is worth noticing that data at $R^{gas}_{CHF_3} = 0.1$, 0.4, 0.6 and 0.8 correspond to films deposited in over two years before the test. This evidences the extraordinary stability of the films, also confirmed in surface energy experiments. For more fluorinated films, this worn the film too much, so that the wear could not be measured. This is probably a consequence of both the reduced cohesive forces of the films and a loss of adhesion between film and buffer layer.

When the plastic ball was used (for 3 min) the measured wear resistance for $R^{gas}_{CHF_3} = 0.96$ was $(8 \pm 2) \times 10^3\,\mu m^3/Nm$. Less fluorinated films ($R^{gas}_{CHF_3} \lesssim 0.8$), did not show any measurable wear with the reduced load during that time.

Monocrystalline silicon (100) samples, worn with plastic ball, but for 6 min, exhibited a wear rate of $(5 \pm 1) \times 10^3\,\mu m^3/Nm$. Silicon is therefore more wear resistant than films deposited with $R^{gas}_{CHF_3} = 0.96$, whereas for 0.8 films were about five times more resistant. This means that for $R^{gas}_{CHF_3} > 0.8$ either adhesion of the films to the buffer layer is dramatically reduced or the wear rate experiences a strong increase of about one order of magnitude.

In either case, it is clear that there is a strong structural and chemical change between $R^{gas}_{\mathrm{CHF_3}} = 0.8$ and $R^{gas}_{\mathrm{CHF_3}} = 0.96$, as evidenced by wear resistance measurements also by the films' surface energy.

5.4 Conclusions

Fluorinated amorphous carbon thin films have been deposited by pulsed-DC PECVD with different fluorine contents by progressively replacing CH_4 by CHF_3 as precursor gas. A number of experiments to characterize different aspects of the deposition process of fluorinated amorphous carbon thin films and the films themselves have been carried out. These experiments, as a whole, allow a better understanding of the incorporation of fluorine in the films, and the resulting film properties.

The resulting films have shown high abrasive wear resistance (between five and seven times higher than monocrystalline silicon) up to $R^{gas}_{\mathrm{CHF_3}} = 0.8$ combined with reduced acid-base surface energy components ($\gamma^+ \approx 0$ and $\gamma^- \approx 2\,\mathrm{mJ/m^2}$ in both VOCG and DVS scales) and slightly reduced total surface energy ($\gamma_s \approx 40\,\mathrm{mJ/m^2}$ vs $44\,\mathrm{mJ/m^2}$). Friction has remained almost as low as for pure DLC when tested in a high humidity environment ($\mu \approx 0.2$) and roughness has been kept at very low values ($R_q \approx 0.3\,\mathrm{nm}$).

For higher degrees of fluorination, films experience a strong structural and chemical change that increases roughness one order of magnitude and reduces surface energy to values similar to PTFE. Regarding its mechanical properties, these films probably experience a combination of loss of adhesion with the buffer and a lower number of cross-linking C–C bonds.

OESA measurements suggest that CH is exclusively produced by methane whereas atomic H is provided by both precursors in stoichiometric relation. On the other hand, atomic fluorine in the plasma experiences an increase for low $R^{gas}_{\mathrm{CHF_3}}$ and a subsequent reduction when high $R^{gas}_{\mathrm{CHF_3}}$ is used. This change of trend has been explained together with XPS results in terms of abstraction of F by atomic hydrogen from the film: For low $R^{gas}_{\mathrm{CHF_3}}$ the bombardment of positively charged species and reaction with neutral H would keep the still low amount of fluorine in the precursors from incorporating into the film by abstraction and reaction with H to form HF. Also C–H bonds would be etched, but for low $R^{gas}_{\mathrm{CHF_3}}$, these bonds are probably much more abundant than C–F. As $R^{gas}_{\mathrm{CHF_3}}$ is increased, the reduction of hydrogen in the feed gas and its substitution with a strongly electronegative atom, would reduce the bombardment caused by hydrogenated species such as atomic H and CH. This reduction would allow fluorine to remain in the film, explaining its reduction in the plasma and the strong structural and compositional change for $R^{gas}_{\mathrm{CHF_3}}$ close to 1, as evidenced from surface measurements (roughness, surface energy and wear) as well as XPS results.

6

Nanoimprint mold fabrication

In order to produce nanostructures in crystalline silicon substrates, the processes of reactive ion etching (RIE) and ion beam etching (IBE) have been studied and combined with different lithographic techniques: electron beam lithography (EBL) with RIE and colloidal lithography (CL) with IBE. Both techniques have been used to produce large-area structures that could eventually be applied as nanoimprint molds. DLC coatings have been applied to the CL-IBE samples to check the feasibility of mold coating.

The effects of mask-selection (Al or SiO_2) and feed gas composition on roughness, etching rate, selectivity and wall verticality have been studied on the RIE process. On IBE processes, the ion energy and etching rate have been correlated with the technological parameters and a model of etching mechanism has been proposed to explain the shape of the generated structures.

6.1 Sidewall passivated reactive ion etching

6.1.1. Mask selection

The first choice of mask material for the reactive ion etching processes was aluminum. As already explained in subsection 3.1.2, metals provide extreme selectivity to fluorinated chemicals, so that deep trenches can be achieved. Figure 6.1 shows a diagram of 16 crystalline silicon (100) samples etched using different proportions of SF_6, CHF_3 and O_2 with aluminum mask and 4 more using SiO_2 mask. For mask definition, a previous lithography with resist was performed, and then either a lift-off process (for evaporated Al) or a short CHF_3 etching at 3 Pa with 100 W RF (for thermally grown SiO_2) was carried out. The lift-off process consists on stripping out the resist off the substrate with a solvent, so that the Al over it is also removed. Regions without resist keep the metal.

In order to find a recipe providing good verticality and smooth surfaces, the so-called black-silicon method was considered [Jansen et al., 1995]. This method relies on the optical properties of the samples after the processes, depending on their roughness. The black silicon condition is related to a surface morphology composed of tall and thin pillars that capture light. The creation of such pillars from small

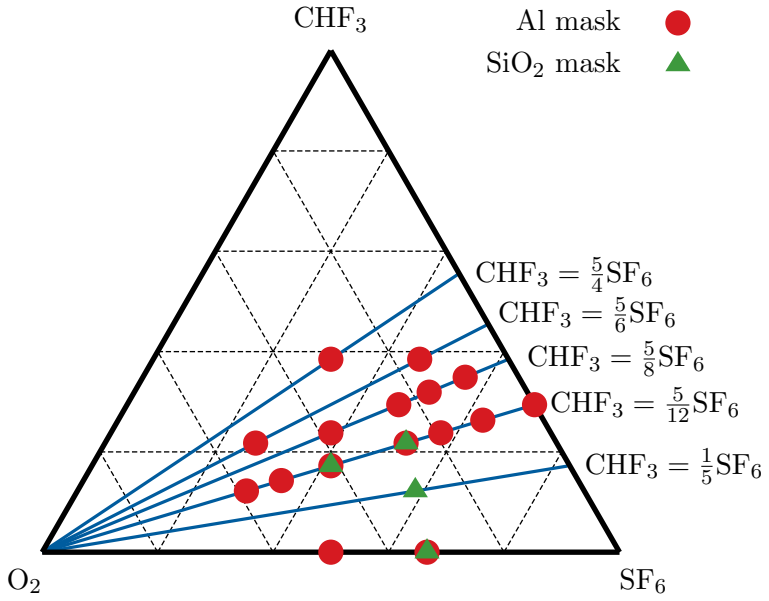

Figure 6.1.: Ternary diagram of etched crystalline silicon samples with different proportions of SF_6, CHF_3 and O_2.

micromasks requires a process of high verticality which can be obtained by using a SF_6/O_2 plasma. The addition of a small amount of CHF_3 eliminates the pillars and smoothens the surface but maintains wall verticality.

The use of aluminum mask, however, was found to be problematic. Although very resistant to this etching, the metal produced micromasking, as it is known in the literature [Glück and Höppner, 1990]. The aluminum mask generates particulates that massively act as micromasks and increase roughness. The relation between O_2 to SF_6 ratio and roughness is shown in figure 6.2. Roughness is shown as a percentage of the etched step, so that the differences in etching rate are considered. Despite the distortion that micromasking represents to roughness, it is apparent from this figure that it is reduced as oxygen proportion is increased. This behaviour can also be observed when representing roughness against Φ_{CHF_3}/Φ_{O_2}. Both dependencies are consistent with the sidewall passivating role of O_2 that allows the vertical wall regime and the beneficial effect of CHF_3 for the reduction of roughness.

Figure 6.3 shows SEM micrographs of steps etched with the same proportions of gases but different mask material: Al vs SiO_2. Besides the difference in the step itself, roughness of the etched part is greatly reduced for the SiO_2 mask (figure 6.3b is more magnified than 6.3a). This reduction was found to be consistent in all the other experiments with SiO_2 mask. This result proofs the micromask generation by aluminum masks.

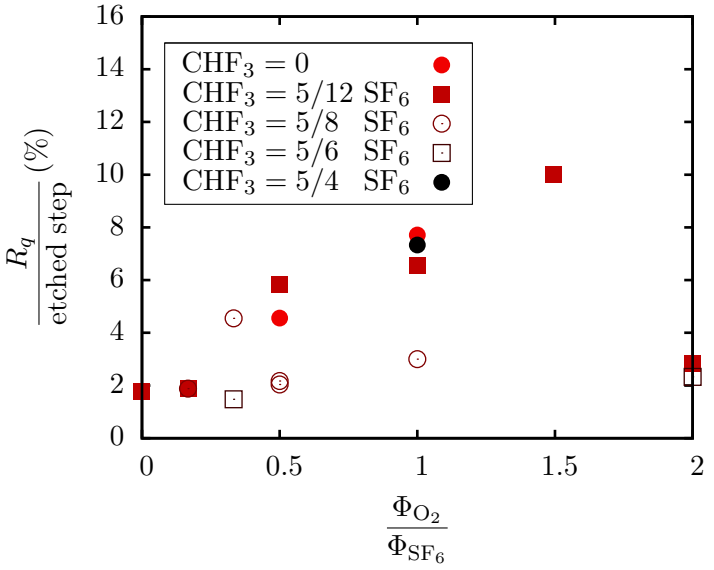

Figure 6.2.: Percentage of roughness to etched step on silicon samples as a function of O_2 to SF_6 flow (Φ) ratio.

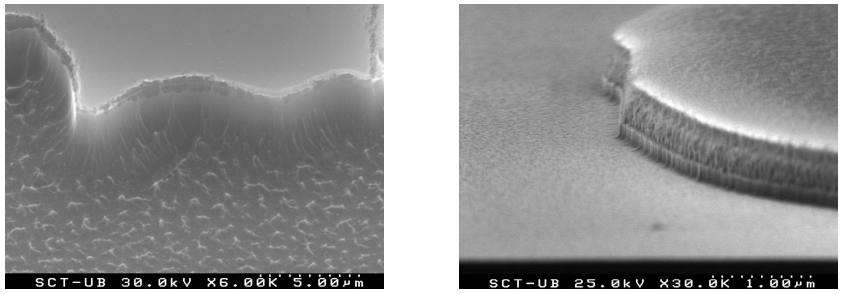

a) b)

Figure 6.3.: a) Step etched with Al mask; b) Step etched with SiO_2 mask.

6.1.2. Etching rate

Aluminum masks allow a convenient measurement of etching rate. Their high etching resistance makes possible to extend the process as long as needed, without risk of loosing the mask. The measured etching rates of silicon, when using Al masks are shown in figure 6.4. It is evident from it, that etching rate is reduced as O_2 to SF_6 ratio is increased. This dependence is not observed for any other pair of gases, so this confirms the etchant and inhibitor role of SF_6 and oxygen.

When SiO_2 mask is used, etching times must be much shorter than for Al, due to the reduced selectivity, because of the faster etch rate than that of Al. Therefore, the etching rate could only be accurately measured on a few samples. For $\Phi_{O_2}/\Phi_{SF_6} = 0.5$, the etching rate was estimated to be about $\sim 200\,\text{nm/min}$.

6.1.3. Wall verticality

Wall verticality is hard to quantify without cross-section images of etched profiles. However, the amount of underetch (etch under the mask; see figure 6.5) is an indicator of this characteristic, this being more important for less vertical and the other way round. It can be seen from figure 6.6 that the underetch is reduced as oxygen to SF_6 ratio is increased.

In this case, the aluminum mask presents the advantage of allowing to see the underetch, due to its high etching resistance. SiO_2 mask, on the other hand, is etched faster and this is never seen. With the latter, a depth corresponding to the resistance and selectivity of the mask is etched vertically and if the process is longer, a profile like that shown in figure 6.3b is produced, with a tapered part on top of the vertical wall due to the faster mask etching in the proximities of the border.

This behavior allows to measure the selectivity of SiO_2 to Si in this particular type of etching. The used oxide masks were 700 nm, 100 nm and 65 nm thick. With the latter, the obtained vertical wall was approximately 300 nm high. This results in a selectivity of about 4.5 times for the selected etching process: 10/2/5 ($SF_6/CHF_3/O_2$), 20 W RF, 13 Pa. This was the recipe chosen for mold fabrication, that represents a good compromise of wall-verticality, surface smoothness and etching rate.

6.1.4. Mold fabrication

A CRESTEC CABL-9500C equipment, installed in the Technological Center of the Optoelectronic Systems and Microtechnology Institute of the Universidad Politécnica de Madrid was used to produce a number of nanopatterns in $5 \times 5\,\text{mm}^2$ areas. Specifically, the following samples were patterned:

- 100 nm-wide lines every 200 nm, 300 nm and 500 nm
- 50 nm-wide lines every 250 nm
- 30 nm in diameter circles every 67 nm and 100 nm

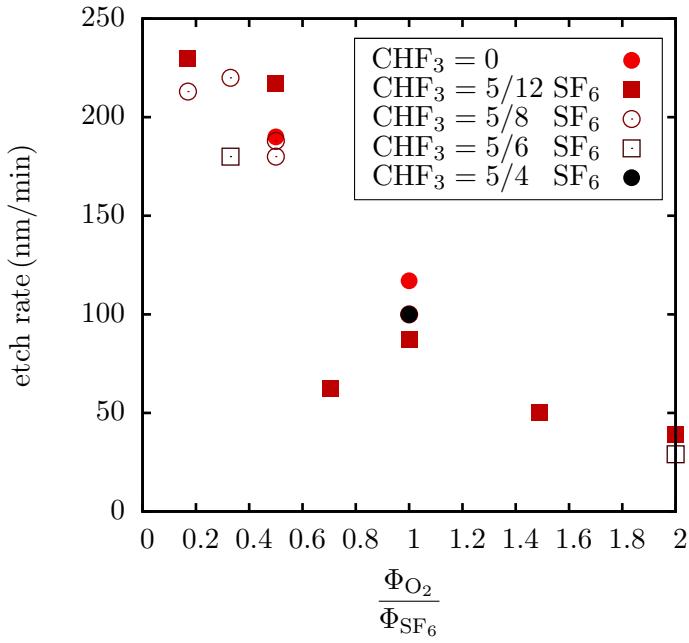

Figure 6.4.: Silicon etching rate dependence on O_2 to SF_6 ratio, from samples masked with Al.

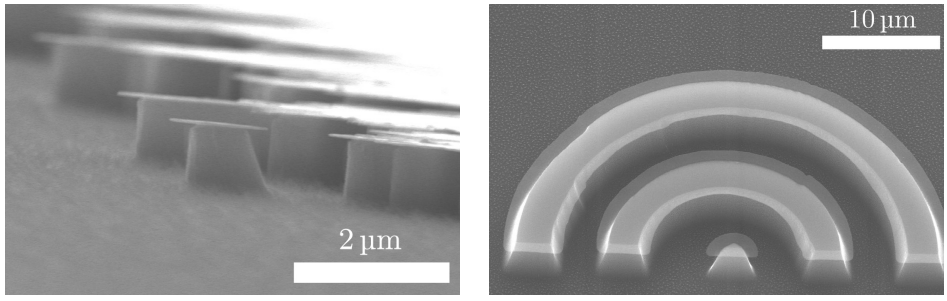

a) b)

Figure 6.5.: Examples of underetch: (a) grazing angle view of a pillar with its mask over the etched region. The whole image is distorted by electrostatic charging; (b) tapered profile that has been etched even being under the mask.

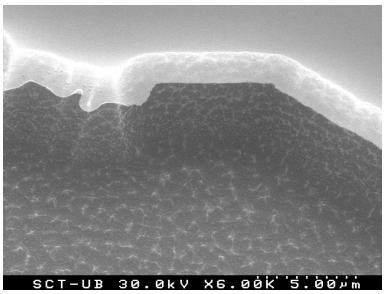

$\Phi_{O_2} = 0$

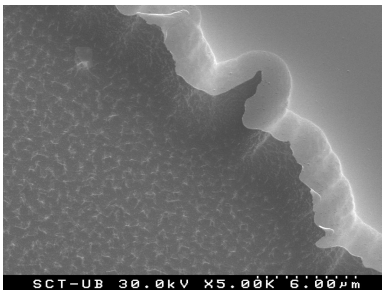

$\Phi_{O_2} = \frac{1}{5}\Phi_{SF_6}$

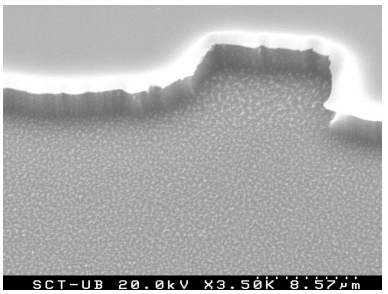

$\Phi_{O_2} = \frac{1}{3}\Phi_{SF_6}$

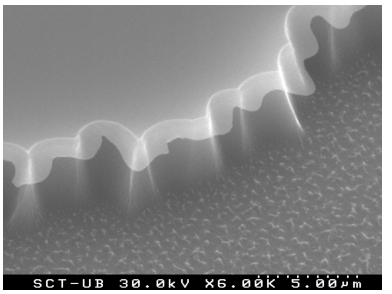

$\Phi_{O_2} = \frac{1}{2}\Phi_{SF_6}$

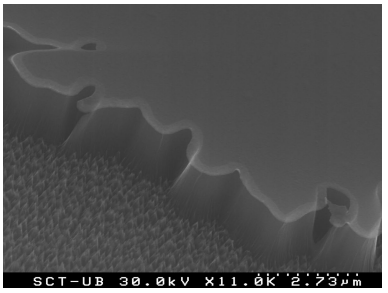

$\Phi_{O_2} = \Phi_{SF_6}$

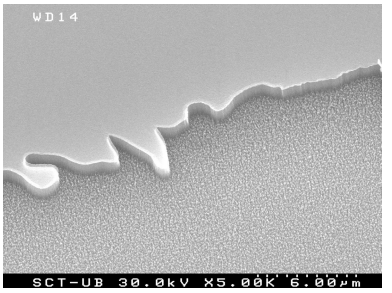

$\Phi_{O_2} = \frac{3}{2}\Phi_{SF_6}$

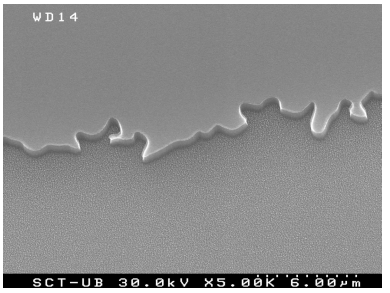

$\Phi_{O_2} = 2\Phi_{SF_6}$

Figure 6.6.: SEM micrographs of etched steps with different O_2 to SF_6 ratios.

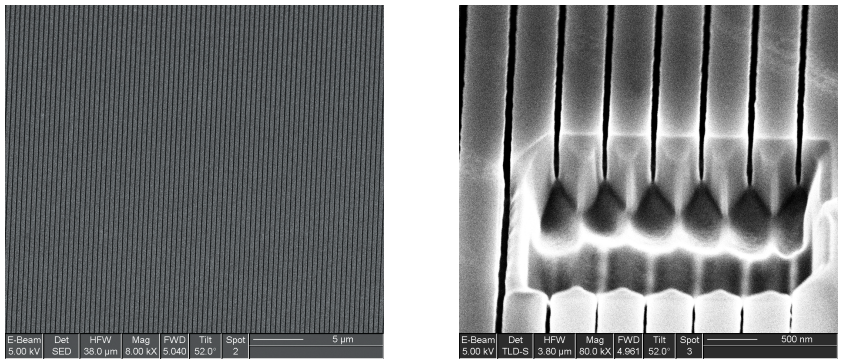

a) b)

Figure 6.7.: Large area ($5 \times 5\,\mathrm{mm}^2$) lithography of 80 nm wide lines every 500 nm. a) general view; b) Cross-section.

- 60 nm in diameter circles every 200 nm

The samples were patterned on ZEP520 resist, from Zeon Corp. This resist is specially designed to provide high RIE resistance while keeping state-of-the-art resolution. Compared to Novolak Resist O (a common UV resist for dry-etching processing of micropatterns), in $CF_4 + O_2$ plasmas ZEP520 is only a 17% less resistant [ZEP, 2001].

Large lithographies require extreme system stability. The equipment used to produce them was specially designed for this purpose, being totally thermally stabilized, and shielded against electromagnetic interferences in a big metal enclosure. Even with all these features, some precautions had to be taken into account to perform the pattern. The electron beam, which was never turned off, had to be set to the desired (low) current at least a day before use. Also, the sample had to be left thermalizing inside the system for a few hours after introduction and before use. These precautions were not critical for the small features but to get good sticking between the $\sim 100\,\mu\mathrm{m}$ writing fields forming the large area. With this system, patterns with features as small as 30 nm were patterned on $5 \times 5\,\mathrm{mm}^2$ areas.

The SEM micrographs shown in figure 6.7 were taken after a 150 s etching of the sample with 100 nm-wide lines every 500 nm. Using a focused ion beam (FIB) tool, a cross-section of the pattern was obtained (figure 6.7b). The width of the lines was measured to be 80 nm, from the cross-section images, while the depth was about 500 nm. The difference in linewidth after pattern transfer is a common problem in these type of structures for RIE processes. The narrower the structure, the harder it is for the chemically active species to get into the structure. Moreover, the combination of two processes for SiO_2 etching first and Si etching second can contribute to this effect. However, considering how narrow the structures were, high wall verticality and aspect ratio was obtained.

6.2 Ion beam etching

6.2.1. Ion source characterization

In order to study the possibility of large-area nanopatterning with colloidal lithography and the effects of changing the ion-beam incidence angle, the ion source described in subsection 3.1.2 has been used. As opposed to reactive ion etching, when using the ion source, the sample holder can be tilted at any angle between 0° and 90° so that the etching is not longer necessarily perpendicular to the sample plane. This possibility not only can be useful for certain nanoimprint mold designs, but also for other applications where anisotropy is desired.

By means of a Faraday cup, the ion current density and energy corresponding to different grid potentials was measured. The set up of the ion source and the Faraday cup is such that very few electrons can reach the cup. As described in subsection 3.1.2, the deep potential drop that charged particles find after the screen strongly reduces the number of electrons surpassing the acceleration grid. For this reason, the retarding aperture can be used to select the ion energy, and there is no need for biasing the collector.

The collected current (I_C) as a function of ion energy (E) has been fitted with Boltzmann functions:

$$I_C(E) = \frac{A_1 - A_2}{1 + e^{(E-E_0)/\sigma}} + A_2$$

where A_1 and A_2 are constants, E_0 is the average ion energy and σ is the FWHM of the energy dispersion.

Moreover, $I_C(E)$ will be such that:

$$I_C(E) = \int_E^\infty f(V)\, dV$$

where V is the retarding voltage and $f(V)$ is the incoming-ion energy distribution function (IEDF). Therefore, in order to obtain IEDF, the collected current must be differentiated. Figure 6.8a shows a typical IEDF from the experiments of this subsection. The energy dispersion for all of them is $9 \pm 1\,\text{eV}$, a bit higher than the nominal value of 7 eV provided by the manufacturer, which could be due to differences in the Ar pressure. A higher pressure would increase collisions from the source to the target, thereby increasing the energy dispersion. The mean free path for the experiments shown here is slightly shorter than the source-target distance.

The results shown in figure 6.8b and 6.9a confirm that the energy of the ions is mainly determined by the screen grid. On the other hand, the accelerator grid does not provide more energy to the ions but focuses the beam on a smaller or bigger spot (by reducing divergence).

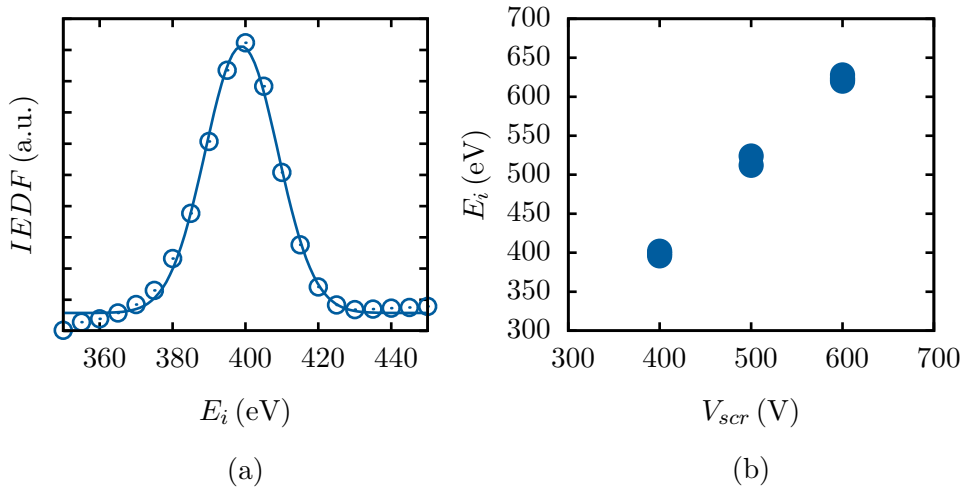

Figure 6.8.: Faraday cup measurements using $P = 40\,\mathrm{W}$ at $\sim 2 \times 10^{-4}\,\mathrm{Pa}$ of Ar. (a) Ion energy distribution function corresponding to $V_{scr} = 500\,\mathrm{V}$, $V_{acc} = -50\,\mathrm{V}$. The fitted Gaussian profile is centered at $398.9 \pm 0.2\,\mathrm{eV}$ with a FWHM $= 10.0 \pm 0.2\,\mathrm{eV}$; (b) Nine ion energy measurements for different screen and accelerator potentials. Only screen potential changes the ion energy so that some data is overlapped.

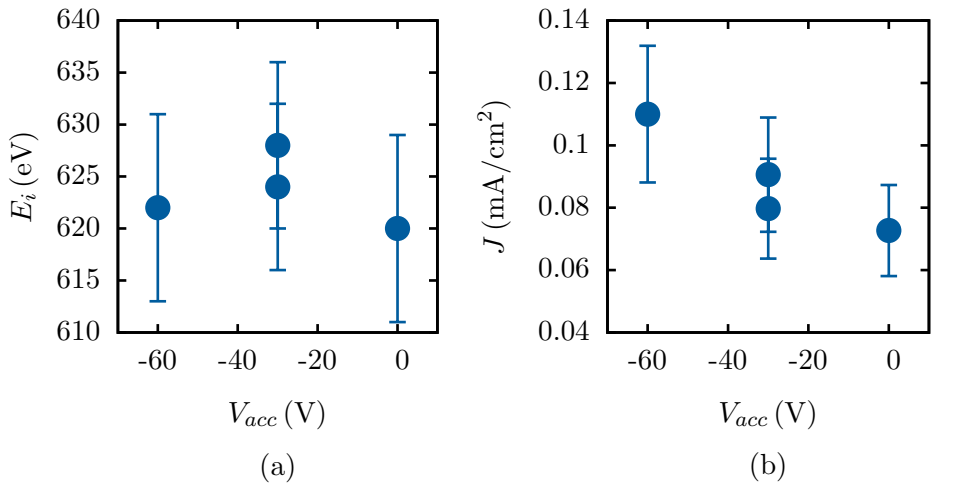

Figure 6.9.: Ion energy and current density measurements for different accelerator potentials

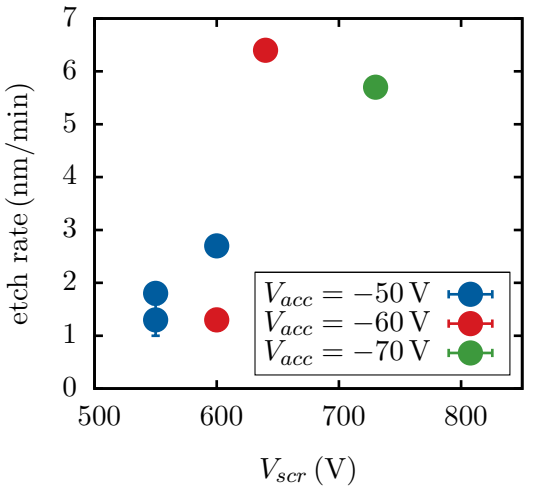

Figure 6.10.: Silicon ion etching rate for different screen potentials ($\sim$ ion energy).

Figure 6.9b shows that the ion current density J, in approximately the center of the beam, increases with the absolute value of the accelerator grid potential (V_{acc}). Specifically, when increased from 0 to -60 the current density changes to about 50% more. The error bars for J are calculated by combining the standard deviation of the different measurements and taking into account the hole's diameter deviation from the nominal value. The user's manual of the Faraday cup does not provide an estimation of such error, so it has been taken to be $0.50 \pm 0.05\,\mathrm{mm}$.

The change of spot size with V_{acc} represents a problem for examining the relationship between etching rate and ion energy, due to the changing ion current density. The ion source manufacturer does not recommend to overdrive the accelerator grid potential over a tenth of the screen potential ($V_{scr}/10$), so the accelerator has been kept close to the maximum: $V_{scr}/(10.5 \pm 0.5)$, for improved beam parallelity. Measurements of etching rate in these conditions (shown in figure 6.10) show a steep dependence of etching rate with V_{scr}, both globally for all data and by data sets of constant V_{acc}. This is not consistent with the ion energy dependence of physical sputtering yield (see figure 3.5) and suggests an increase of the current with V_{scr}. Therefore, neither $V_{acc} = V_{scr}/10$ nor constant V_{acc} guarantee constant spot size.

6.2.2. Mold fabrication

A much simpler alternative to EBL for large area patterning is Colloidal Lithography (CL). The technique consists on the arrangement of particles on a substrate so that they can be used as a template/mask for subsequent etching. This constitutes an alternative method to other techniques for the production of permanent periodic structures or to reproduce nanopatterns on a large-area surface. Although CL is

Figure 6.11.: SEM micrographs of sub-micron particle monolayer on glass before (a) and after (b) etching at 45° for 53 min.

less versatile than EBL or other lithographic techniques, regarding non-periodic patterns, the reduction of time and resources for the production of large-area periodic nanopatterns represents important advantages for certain applications or fields such as photonic crystals, [López, 2003] thermophotovoltaics [Mao and Ye, 2010] or optical biosensors [Dorfner et al., 2009]. The differences in the structuration produced by ion beam etching with different angles has been studied as a method for nanoimprint mold fabrication [Portal et al., 2009].

The silica sub-micron particles (SP) used as mask were produced by sol-gel process [Ebelmann, 1846; Brinker and Scherer, 1990] using the Stöber method [Stöber et al., 1968]. TEOS[1] was used as precursor, and hydrolysis and condensation reactions were initiated by the addition of water diluted in ethanol. A small concentration of ammonia (NH_4OH) in the solution fixed the pH to basic.

The subsequent arrangement in hexagonal compact structures, on monocrystalline silicon, was done by the Langmuir-Blodgett (LB) technique [Blodgett, 1934; Petty, 1996]. In order to use this technique, SPs were functionalized with APTS[2] and then diluted in a mixture of methanol and chloroform (1:3) before spreading them on the water surface for the LB process. Finally, the barriers of the LB setup were brought closer at a constant rate of 10 mm/min, up to a pressure of 5 mN/m. Then the substrate was lifted from the trough at 2 mm/min with constant pressure, dragging on its surface a monolayer of silica sub-micron particles.

Figure 6.11a shows an SEM picture of a typical obtained monolayer. The particles have a diameter of 310 ± 20 nm as measured from the microscopy images and according to AFM data, their surface is smooth. These layers exhibit an hexagonal compact structure. Defects in the form of lacunas or changes in the direction

[1] tetraethylorthosilicate
[2] 3-Aminopropyltriethoxysilane

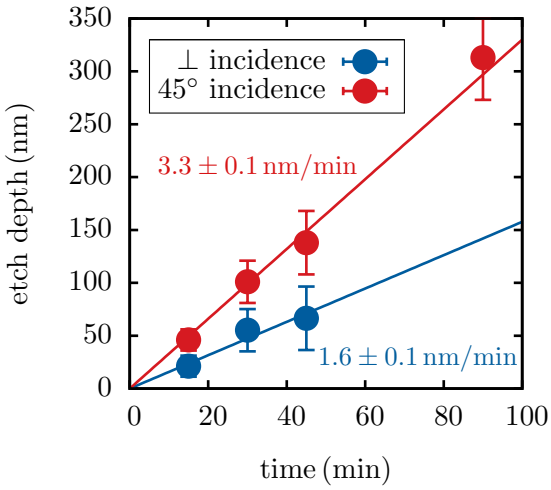

Figure 6.12.: Silicon ion etching depth for different times and incidence angles.

of the periodicity can be found, which usually correspond to inadequate surfactant concentration, impurities or to the dispersion in particle size.

Etchings of 15 min, 30 min, 45 min and 60 min were carried out for ion beam incidence perpendicular to the sample plane and 15 min, 30 min, 45 min, 60 min and 90 min for 45° incidence. The silicon etching depths for the different situations, shown in figure 6.12, reveal a constant etching rate with time, with values consistent with those exposed in the preceding subsection for perpendicular incidence (figure 6.10).

The higher etching rate for oblique incidence is well known and understood. At normal incidence the collision cascade of Ar ions is deeper into the target than for more oblique incidence, which results in an increased sputtering yield for the latter. For incidence angles greater than 70°, the interaction of the beam with the target is reduced, and the etching rate is reduced again [Giannuzzi and Stevie, 2005]. Figure 6.13 shows the anisotropy induced in the sample after etching with a certain angle. Large nanopatterns with in-plane anisotropies can be used for nanofluidic pumps or photonic crystals.

As expected, the mask (particles) is also etched with the ion beam. SEM observation of the samples after short etching processes show vertical or oblique silicon pillars with top-etched particles over them. After more etching time, the particles start to reduce their diameter and the top of the silicon pillar starts to be etched, as well. This happens for both incidence angles. A representation of the mechanism producing these structures is depicted in figure 6.14.

Due to the angle at which the SEM images where taken, the particle shape for oblique incidence could not be estimated except for the longest etching process, for

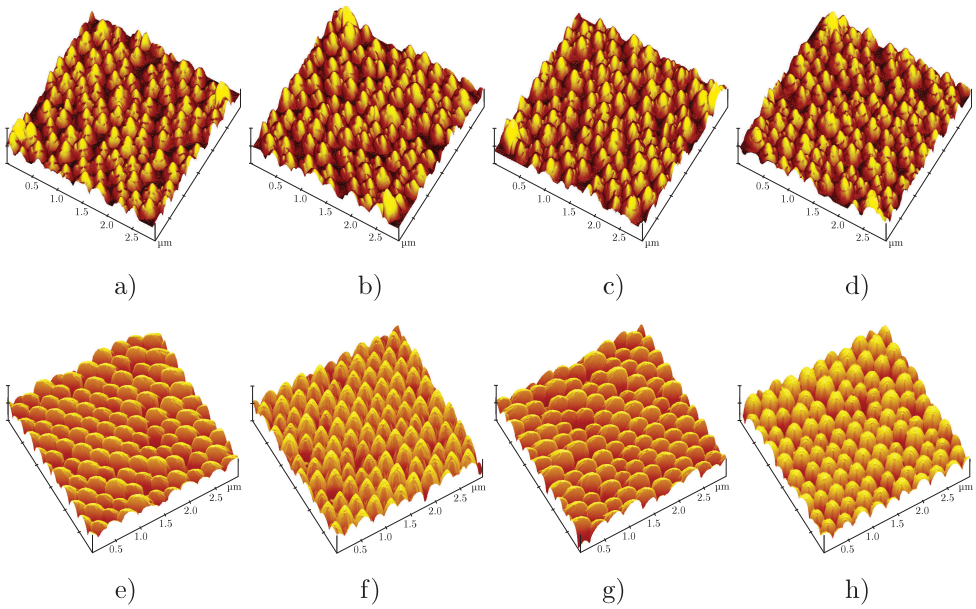

Figure 6.13.: AFM images of CL pattern etched with: (a) to (d) normal incidence; (e) to (h) oblique incidence. Each image has been taken by rotating the sample 90°.

which the particle was measured to be 70 nm in diameter. This would represent an etching rate of 2.6 nm/min. For perpendicular incidence, the diameter could be measured for all etching times providing an etching rate of 2.9 ± 0.4 nm/min. This is also consistent with the known higher physical etching rate of SiO_2 than Si [Lieberman and Lichtenberg, 1994].

6.2.3. Mold coating

In order to check the feasibility of mold coating with DLC using pulsed-DC PECVD, the samples etched by IBE after CL were coated with fluorine free DLC. This is a first step towards the deposition of fluorinated DLC and the study of its de-molding properties.

Figure 6.15 shows SEM images of 50 nm thick films deposited on Si molds etched for different times. The aspect ratio of the structures increases with etching duration up to 45 min, for which silica sub-micron particles cannot longer be removed maybe due to an ion induced silicon welding or implantation. For etching durations of 60 min, pillars are etched away.

The deposition process results in a conformal film which reproduces with moderate fidelity the underlying structure, to which no appreciable damage by the intense ion bombardment associated to diamond-like carbon deposition is observed. However,

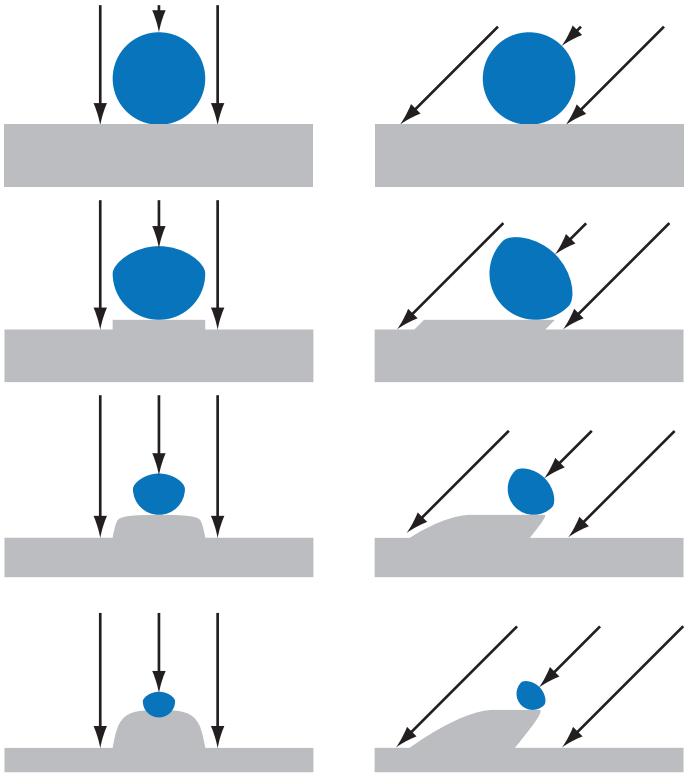

Figure 6.14.: Schematic representation of the etching mechanism when silica submicron particles are used as mask, for normal and oblique (45°) incidence.

due to the comparable film thickness and feature size, a visible smoothing of the pillars' edges is observed. The crater-like top surface of the pillars after DLC deposition, had already been detected by AFM characterization before DLC deposition, and is probably related to the redeposition of the etched silica particle.

The beneficial surface properties of DLC or FDLC for de-molding arise from the very first monolayers of the film. Therefore, for this application only thin layers are required, which would probably avoid most of the edge-smoothing and edge-induced faster deposition rate effects.

In order to continue the project, molds coated with DLC or FDLC should be tested in a real nanoimprint processes to check for improved de-molding characteristics versus bare silicon.

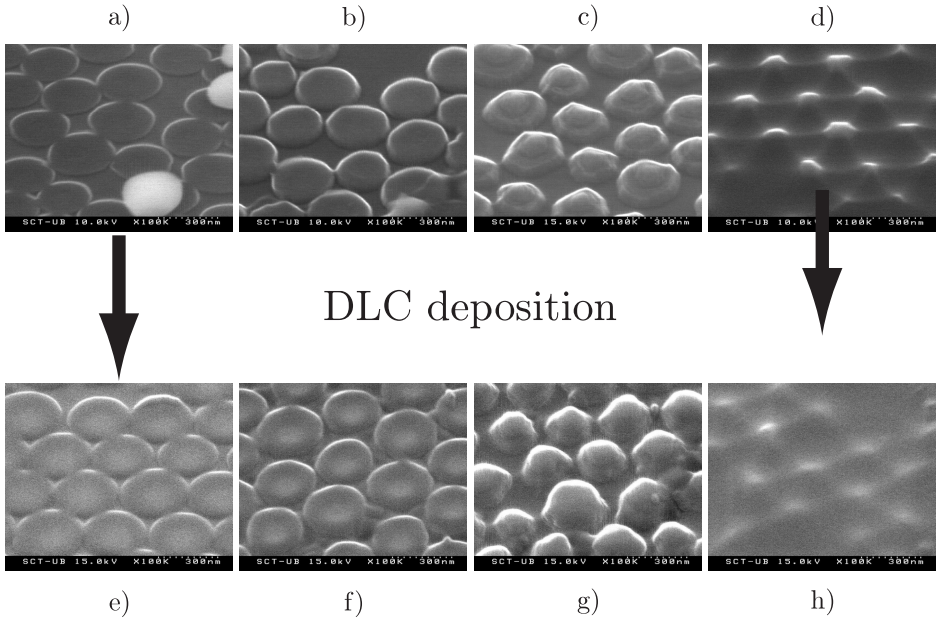

Figure 6.15.: SEM micrographs of nanostructured molds before and after DLC deposition. (a) and (e) 15 min of etching, (b) and (f) 30 min, (c) and (g) 45 min, (d) and (h) 60 min

6.3 Conclusions

Two different etching and lithographic techniques have been applied to silicon nanostructuration. With EBL, patterns with feature sizes as small as 30 nm in $5 \times 5\,\mathrm{mm}^2$ have been produced while for CL larger areas of about $20 \times 20\,\mathrm{mm}^2$ where patterned with sub-micron features ($\sim 300\,\mathrm{nm}$). The combination of the lithographic techniques in large-area with the etching capabilities opens the possibility of producing nanoimprint molds or nanostructured materials with modified macroscopic properties.

Regarding the sidewall passivated etching process, a recipe combining low surface roughness, high wall verticality and moderate selectivity has been obtained by combining the passivating and etching characteristics of different gases. The selected recipe provided a SiO_2 to Si selectivity of 4.5 with vertical walls and an etching rate of about $\sim 200\,\mathrm{nm/min}$. The micromask generation by aluminum has been confirmed by comparing with SiO_2 masks. Also, from the etching rate measurements, it can be determined that the etchant and inhibitor roles correspond to SF_6 and oxygen, respectively.

A better understanding of the HFQ1303-3's ion beam characteristic has been obtained by performing measurements with a Faraday cup. The ion energy distribution has been determined along with the technological parameters that determine it. Also, the etching rate of silicon for different ion energies has been measured, although a good control of the beam shape would require a careful calibration by accurately positioning the Faraday cup at different distances from the beam axis.

Angle-dependent ion beam etching experiments on samples covered with a submicron particle monolayer was essayed with an ion beam source and a tiltable sample holder. The results confirm both the higher etching rate of SiO_2 than Si and the angle dependence on the sputtering yield. A model explaining the different structures that arise, when different etching times are used, is proposed.

Conclusions

- Fluorinated amorphous carbon films have been deposited by pulsed-DC plasma enhanced chemical vapor deposition, by progressively replacing methane by trifluoromethane. The experimental device used for deposition has been designed and built to allow a number of multiple processes in the same reactor. The results of the study demonstrate the feasibility of this technique, of easy industrial implementation, for the deposition of this type of coatings.

- The characterization of both the active species in the plasma and the groups incorporated into the deposited films has helped to understand the process of fluorine incorporation, as well as the change in the surface properties that it entails.

- For trifluoromethane concentrations in methane below 80%:

  - The F:C ratio in the films shows a weak dependence with the fraction of fluorinated precursor and it increases slowly from zero up to a 1:4 ratio. The $C-F$ and $C-F_2$ bonds can be detected for trifluoromethane concentrations above 50% and increase with it.

  - Total surface energy suffers a slight reduction from $44\,mJ/m^2$ to $40\,mJ/m^2$, whereas the acid-base component is reduced linearly to zero for pure trifluoromethane.

  - Humidity plays a significant role in friction, by reducing it and finally stabilizing it at low values for high relative humidity. This behavior is explained in terms of superficial removal of hydrogen, and possibly fluorine, by the effect of friction, and the increase of hydrogen and hydroxyl groups' availability with humidity, to passivate the surface.

  - Abrasive wear resistance and roughness barely change. The former remains in the range of five to seven times that of silicon, while the latter remains at atomic level, as non-fluorinated amorphous carbon.

  - The combined properties in this range makes the films adequate as anti-adhesive and wear resistant coatings.

- For trifluoromethane concentrations above 80%, the films undergo a sudden and important structural and chemical change that:

  - Increases the F:C ratio in the film up to 1:1 along with a higher concentration of $C-F$, $C-F_2$ and $C-F_3$ bonds.

  - Rises roughness one order of magnitude and increases the number of defect in the film.

  - Reduces surface energy to values close to PTFE at $18\,mJ/m^2$ with barely any acid-base contribution.

  - Causes a combination of loss of adhesion to the buffer layer and reduction in cross-linking and internal cohesion, with abrasive wear rates that could be one order of magnitude higher than those for non-fluorinated films.

- The mixture of trifluoromethane and methane has shown to increase the deposition rate and reduce the compressive intrinsic stress of the films. Both phenomena could be related with a mass density reduction of the films and a progressive loss of cohesion.

- Optical emission spectroscopic actinometry measurements have revealed that CH species are exclusively produced by methane, while atomic hydrogen in the plasma, is produced by both precursors in stoichiometric ratio. In addition to these species, the measurements have shown the presence of CF_2, CHF and atomic fluorine in the plasma.

- Based on the characterization of the active species in the plasma and the composition of the deposited films, a descriptive model of the mechanisms controlling fluorine incorporation has been developed, based on the commonly agreed mechanisms by the scientific community, for non-fluorinated films.
  For low trifluoromethane concentrations, the bombardment of the film with cations and the reaction with neutral hydrogen atoms keeps the still low amount of fluorine in the precursors from incorporating into the film by abstraction and reaction with H to form HF. This mechanism would also affect C–H bonds, by forming molecular hydrogen, but to a lesser extent because these bonds are probably much more abundant than C–F.
  As trifluoromethane quantity is increased, the reduction of hydrogen in the feed gas and its substitution with a strongly electronegative atom, reduces the bombardment caused by hydrogenated species such as atomic H and CH. This reduction, in turn, allows fluorine to remain in the film, explaining the reduction of emission in the plasma and the strong structural and compositional change when methane fraction is close to zero, as evidenced by the analyzed surface properties: roughness, surface energy and wear, as well as XPS results.

- Regarding the fabrication of nanoimprint lithography molds, two different techniques have been explored, in adequate setups for large-area structuration. This way, one of the thesis and the SURFaC project goals is completed. With electron beam lithography structures as small as 30 nm in diameter separated every 67 nm and in a $5 \times 5\,mm^2$ area, have been produced. On the other hand, colloidal lithography has allowed the production of periodic structures with features of about 300 nm in $20 \times 20\,mm^2$ areas. The combination of large-area lithographic techniques with the capability of deep or directional ion etching opens up the possibility of producing both nanoimprint molds as other nanostructured materials with observable macroscopic properties.

- The deep etch technique has been optimized to obtain low roughness along with high wall verticality and moderate selectivity. Specifically, etching rates of about 200 nm/min, selectivities of 4.5 and totally vertical walls have been combined in a single process.

- Ion etchings at different incidence angles and for different times have been carried out with the ion gun on sub-micron particles monolayers. The different stages of the processes have been described and explained considering the simultaneous etching of mask and substrate. The anisotropic transfer of patterns to the substrate, opens up the possibility of fabricating nanofluidic devices or photonic crystals.

- Globally, the properties of the deposited films suggest their usefulness to coat surfaces requiring low surface energy combined with high mechanical resistance. Moreover, the conformal coating of the nanostructures opens up the possibility of using these films in nanopatterned mold for applications like nanoimprint lithography.

- As future prospects, also within the framework of the SURFaC project, it would be interesting to investigate deeper the deposition of films with trifluoromethane concentrations above 80%, for which adhesion between buffer layer and film should be improved.

Publications and communications

The following sections contain a list of the published articles and conferences' contributions of the author, both for this thesis and other scientific activities.

Regular journals

- "Structured epitaxial graphene growth on SiC by selective graphitization using a patterned AlN cap", M. Rubio-Roy, F. Zaman, Y. Hu, C. Berger, M.W. Moseley, J.D. Meindl, W.A. de Heer, Applied Physics Letters (submitted) (2009)

- "Surface structuring of diamond-like carbon films by colloidal lithography with silica sub-micron particles", C. Corbella, S. Portal, M. Rubio-Roy, M.A. Vallvé, J. Ignes-Mullol, E. Bertran, J.L. Andújar, Diamond and Related Materials (submitted) (2009)

- "Influence of incident ion beam angle on dry etching of silica sub-micron particles deposited on Si substrates", S. Portal, M. Rubio-Roy, C. Corbella, M.A. Vallvé, J. Ignes-Mullol, E. Bertran, Thin Solid Films, 518 (2009) 1543

- "Plasma parameters of pulsed-dc discharges in methane used to deposit diamondlike carbon films", C. Corbella, M. Rubio-Roy, E. Bertran, J.L. Andújar, Journal of Applied Physics, 106 (2009) 033302

- "Effects of environmental conditions on fluorinated diamond-like carbon tribology", M. Rubio-Roy, C. Corbella, E. Bertran, S. Portal, M.C. Polo, E. Pascual, J.L. Andújar, Diamond and Related Materials, 18 (2009) 923

- "Low friction and protective diamond-like carbon coatings deposited by asymmetric bipolar pulsed plasma", C. Corbella, M. Rubio-Roy, E. Bertran, M.C. Polo, E. Pascual, J.L. Andújar, Diamond and Related Materials, 18 (2009) 1035

- "Magnetic domain wall pinning by focused ion beam milling of permalloy layers", A. Olziersky, A. Vilà, M. Rubio-Roy, E. Bertran, J. Fontcuberta, Microelectronic Engineering, 86 (2009) 878

- "Electrical measurements of pulsed-DC plasmas used for diamond-like carbon film deposition", C. Corbella, M. Rubio-Roy, M.C. Polo, E. Pascual, J.L. Andújar, E. Bertran, Metallurgical Analysis, 28 (2008) 1190

- "Fluorinated DLC deposited by pulsed-DC plasma for antisticking surface applications", M. Rubio-Roy, E. Bertran, E. Pascual, M.C. Polo, J.L. Andújar, Diamond and Related Materials, 17 (2008) 1728

- "Structural and optical properties of diamond like thin films deposited by asymmetric bipolar pulsed DC reactive magnetron sputtering", M. Rubio-Roy, E. Pascual, M.C. Polo, J.L. Andújar, E. Bertran, Surface and Coatings Technology, 202 (2007) 2354

- "Carbon nanotubes grown by asymmetric bipolar Pulsed-DC PECVD", J. García-Céspedes, M. Rubio-Roy, M.C. Polo, E. Pascual, J.L. Andújar, E. Bertran, Diamond and Related Materials, 16 (2007) 1131

- "Diamond like carbon films deposited from graphite target by asymmetric bipolar pulsed-DC magnetron sputtering", M. Rubio-Roy, C. Corbella, J. Garcia-Céspedes, M.C. Polo, E. Pascual, J.L. Andújar, E. Bertran, Diamond and Related Materials, 16 (2007) 1286

Proceedings books

- "Peak voltage variation in a bipolar pulsed-DC methane discharge aimed to the deposition of DLC films", C. Corbella, M. Rubio-Roy, M.C. Polo, E. Pascual, E. Bertran, J.L. Andújar, Proceedings of the 19th International Symposium on Plasma Chemistry - Topic 7: Plasma deposition of inorganic films and hard coatings

- "Self-assembling submicroparticles on a patterned surface", S. Portal, M.A. Vallvé, E. Prats-Miralles, J. Ignes-Mullol, E. Pascual, M. Rubio-Roy, E. Bertran, Proceedings of the X Congreso Nacional de Materiales, 1 (2008) 561

- "Depósito y caracterización de capas de carbono amorfo de baja energía superficial", M. Rubio-Roy, S. Portal, M.C. Polo, E. Pascual, E. Bertran, J.L. Andújar, Proceedings of the X Congreso Nacional de Materiales, 1 (2008) 393

- "Fluorination effects on tribological characteristics of hydrogenated amorphous carbon thin films", M. Rubio-Roy, S. Portal, M.C. Polo, E. Pascual, E. Bertran, J.L. Andújar, NSTI Nanotech 2008 Technical Proceedings - Materials, Fabrication, Particles and Characterization, 1 (2008) 479

Books

- "Industrial Plasma Technology", Y. Kawai, H. Ikegami, N. Sato, A. Matsuda, K. Uchino, M. Kuzuya and A. Mizuno Editors. Wiley-VCH, 2010. ISBN 978-3527325443
  Chapter 27: "Diamond-Like Carbon Thin Films Grown in Pulsed-DC Plasmas" E. Bertran, M. Rubio-Roy, C. Corbella, and J.L. Andújar

Congresses

2010

- The 37th International Conference on Metallurgical Coatings and Thin Films, ICMCTF-37
  Accepted oral contribution: Anisotropic Texturing of Diamond-Like Carbon Films by Colloidal Lithography with Sub-Micron Spheres
  C. Corbella, S. Portal, M. Rubio-Roy, M.A. Vallvé, J. Ignes-Mullol, E. Bertran, J.L. Andújar

- American Physical Society March Meeting 2010
  Portland (United States of America)
  Accepted oral contribution: Selective Graphitization of Silicon Carbide: Effect of Argon Background Pressure and Transport Measurements on the Epitaxial Graphene
  F. Zaman, M. Rubio-Roy, Y. Hu, C. Berger, M.W. Moseley, J.D. Meindl, W.A. de Heer

2009

- 20th European Conference on Diamond, Diamond-like Materials, Carbon Nanotubes and Nitrides
  Athens (Greece)
  Poster: Ion energy distribution during plasma-enhanced chemical vapour deposition of diamond-like carbon films
  C. Corbella, M. Rubio-Roy, E. Bertran, S. Portal, E. Pascual, M.C. Polo, J.L. Andújar

- The 19th International Symposium on Plasma Chemistry, ISPC-19
  Bochum (Germany)
  Poster: Peak voltage variation in a bipolar pulsed-DC methane discharge aimed to the deposition of DLC films
  C. Corbella, M. Rubio-Roy, M.C. Polo, E. Pascual, E. Bertran, J.L. Andújar

- The 36th International Conference on Metallurgical Coatings and Thin Films, ICMCTF-36
  San Diego (United States of America)
  Oral contribution: Nanostructured surfaces of DLC thin films deposited by pulsed-DC discharges
  C. Corbella, S. Portal, M. Rubio-Roy, E. Bertran, M.A. Vallvé, J. Ignes-Mullol, M.C. Polo, E. Pascual, J.L. Andújar
  Oral contribution: Shape modification of silica submicroparticles assembled in compact monolayer by dry etching
  S. Portal, M.A. Vallvé, M. Rubio-Roy, C. Corbella, J. Ignes-Mullol, E. Bertran

2008

- Materials Research Society Meeting - Fall 2008
  Boston (United States of America)
  Oral contribution: Magnetic domain walls in permalloy nanostructures made by FIB
  A. Vilà, A. Olziersky, M. Rubio-Roy, E. Bertran, J. Fontcuberta

- International Conference and Exhibition on Analysis & Testing of Materials, ICASI'2008, CCATM'2008
  Beijing (China)
  Invited conference: Electrical measurements of pulsed-DC plasmas used for diamond-like carbon film deposition
  C. Corbella, M. Rubio-Roy, M.C. Polo, E. Pascual, J.L. Andújar, E. Bertran

- 3rd International Conference on Surface, Coatings and Nanostructured Materials, NanoSMat 2008
  Barcelona (Spain)
  Invited conference: Carbon nanotube based electrodes for energy applications
  E. Bertran, J. García-Céspedes, J.L. Castaño, M. Rubio-Roy, N. Aguiló, E. Jover, E. Pascual, F.J. del Campo, F.X. Muñoz

- 19th European Conference on Diamond, Diamond-Like Materials, Carbon Nanotubes, and Nitrides
  Sitges (Spain)
  Poster: Low friction and protective diamond-like carbon coatings deposited by asymmetric bipolar pulsed plasma
  C. Corbella, M. Rubio-Roy, E. Bertran, M.C. Polo, E. Pascual, J.L. Andújar
  Poster: Effects of environmental conditions on fluorinated diamond-like carbon tribology
  M. Rubio-Roy, C. Corbella, E. Bertran, S. Portal, M.C. Polo, E. Pascual, J.L. Andújar

- 3rd International School of Advanced Plasma Technology
  Villa Monastero (Italy)
  Invited conference: DLC thin films grow in pulsed-DC plasmas
  E. Bertran, M. Rubio-Roy, C. Corbella, J.L. Andújar

- NSTI Nanotechnology Conference, Nanotech 2008
  Boston (United States of America)
  Poster: Fluorination effects on tribological characteristics of hydrogenated amorphous carbon thin films
  M. Rubio-Roy, S. Portal, M.C. Polo, E. Pascual, E. Bertran, J.L. Andújar

- X Congreso Nacional de Materiales
  San Sebastián (Spain)

Poster: Self-assembling submicroparticles on a patterned surface
S. Portal, M.A. Vallvé, E. Prats-Miralles, J. Ignes-Mullol, E. Pascual, M. Rubio-Roy, E. Bertran
Poster: Depósito y caracterización de capas de carbono amorfo de baja energía superficial
M. Rubio-Roy, S. Portal, M.C. Polo, E. Pascual, E. Bertran, J.L. Andújar

- 34th International Conference on Micro- and Nano-Engineering, MNE2008
  Athens (Greece)
  Oral contribution: Magnetic domain wall pinning by focused ion beam milling of permalloy layers
  A. Olziersky, A. Vilà, M. Rubio-Roy, E. Bertran, J. Fontcuberta

2007

- 18th European Conference on Diamond, Diamond-Like Materials, Carbon Nanotubes, and Nitrides
  Berlin (Germany)
  Poster: Fluorinated DLC deposited by pulsed-DC plasma for antisticking surface applications
  M. Rubio-Roy, E. Bertran, E. Pascual, M.C. Polo, J.L. Andújar

- European Materials Research Society, E-MRS 2007
  Strasbourg (France)
  Oral contribution: Structural and optical properties of diamond like thin films deposited by asymmetric bipolar pulsed DC reactive magnetron sputtering
  M. Rubio-Roy, E. Pascual, M.C. Polo, J.L. Andújar, E. Bertran

2006

- 17th European Conference on Diamond, Diamond-Like Materials, Carbon Nanotubes, and Nitrides
  Estoril (Portugal)
  Poster: Diamond like carbon films deposited from graphite target by asymmetric bipolar pulsed-DC magnetron sputtering
  M. Rubio-Roy, C. Corbella, J. Garcia-Céspedes, M.C. Polo, E. Pascual, J.L. Andújar, E. Bertran
  Poster: Carbon nanotubes grown by asymmetric bipolar Pulsed-DC PECVD
  J. García-Céspedes, M. Rubio-Roy, M.C. Polo, E. Pascual, J.L. Andújar, E. Bertran

- IV Reunión del Grupo Especializado en Física del Estado Sólido (GEFES)
  Alicante (Spain)
  Poster: Electron beam lithography for manganite-based magnetic tunnel junctions

M. Rubio-Roy, I.C. Infante, M.C. Polo, F. Sánchez, V. Laukhin, E. Bertran, M. Varela, J. Fontcuberta

2005

- 16th European Conference on Diamond, Diamond-Like Materials, Carbon Nanotubes, Nitrides and Silicon Carbide, Diamond 2005
  Aveiro (Portugal)
  Poster: Growth kinetics of carbon nanotubes with heterojunctions of curly and straight segments prepared by pulsed RF PECVD
  J. García-Céspedes, M. Rubio, C. Corbella, E. Pascual, M. Galán, G. Viera, E. Bertran

- Trends in Nanotechnology 2005, TNT2005
  Oviedo (Spain)
  Poster: Growth of carbon nanotubes from nickel dots prepared by electron-beam lithography and magnetron sputtering
  M. Rubio-Roy, J. García Céspedes, R. Fontarnau, M.C. Polo, E. Bertran

Bibliography

Zep520. Technical report, Zeon Corporation, Specialty Materials Division, 2001.

S. Aisenberg and R. Chabot. Ion-beam deposition of thin films of diamondlike carbon. *Journal of Applied Physics*, 42(7):2953–2958, 1971. doi: 10.1063/1.1660654.

I. Aksenov, S. Vakula, V. Padalka, and V. Strelnitskii. *Soviet Physics - Technical Physics*, 25:1164, 1980.

A. O. Altun, J. H. Jeong, J. J. Rha, D. G. Choi, K. D. Kim, and E. S. Lee. Fabrication of fluorine-doped diamond-like carbon stamps for uv nanoimprint lithography. *Nanotechnology*, 17(18):4659–4663, 2006. doi: 10.1088/0957-4484/17/18/022.

J. L. Andújar, M. Vives, C. Corbella, and E. Bertran. Growth of hydrogenated amorphous carbon films in pulsed d.c. methane discharges. *Diamond and Related Materials*, 12(2):98–104, 2003. doi: 10.1016/S0925-9635(03)00009-8.

R. Bahl, M. Vedawyas, D. Patel, A. Kumar, and M. Shamsuzzoha. Evaluation of mechanical properties of dlc-tic microlaminate coatings. In R. Vinci, O. Kraft, N. Moody, P. Besser, and E. Shaffer, editors, *Thin Films-Stresses and Mechanical Properties VIII*, volume 594 of *Materials Research Society Symposium Proceedings*, pages 331–336. Materials Research Society, 2000. Symposium V held at the 1999 MRS Fall Meeting.

F. Banhart. Irradiation effects in carbon nanostructures. *Reports on Progress in Physics*, 62(8):1181, 1999. doi: 10.1088/0034-4885/62/8/201.

T. Barr. *Modern ESCA: the principles and practice of X-Ray photoelectron spectroscopy*. CRC Press, 1994. ISBN 0849386535.

M. Beck, M. Graczyk, I. Maximov, E. L. Sarwe, T. G. I. Ling, M. Keil, and L. Montelius. Improving stamps for 10 nm level wafer scale nanoimprint lithography. *Microelectronic Engineering*, 61-62:441–448, 2002. doi: 10.1016/S0167-9317(02)00464-1.

J. C. Berg, editor. *Wettability*. Marcel Dekker, Inc., 1993. ISBN 0824790464.

K. B. Blodgett. Monomolecular films of fatty acids on glass. *Journal of the American Chemical Society*, 56(2):495–495, 1934. doi: 10.1021/ja01317a513.

D. Briggs. *Surface analysis of polymers by XPS and static SIMS*. Cambridge University Press, 1998. ISBN 0521352223.

C. J. Brinker and G. W. Scherer. *Sol-Gel Science: The Physics and Chemistry of Sol-Gel Processing*. Academic Press, Inc., 1990. ISBN 978-0-12-134970-7.

A. Bubenzer, B. Dischler, G. Brandt, and P. Koidl. rf-plasma deposited amorphous hydrogenated hard carbon thin films: Preparation, properties, and applications. *Journal of Applied Physics*, 54(8):4590–4595, 1983. doi: 10.1063/1.332613.

L. Businaro. *Fabrication and characterization of photonic band gap materials*. PhD thesis, Università degli studi di Catania, 2005. URL `http://www.tasc.infm.it/research/amd/theses/Businaro.pdf`.

R. S. Butter, D. R. Waterman, A. H. Lettington, R. T. Ramos, and E. J. Fordham. Production and wetting properties of fluorinated diamond-like carbon coatings. *Thin Solid Films*, 311(1-2):107–113, 1997. doi: 10.1016/S0040-6090(97)00337-4.

H. Cao, Z. Yu, J. Wang, J. O. Tegenfeldt, R. H. Austin, E. Chen, W. Wu, and S. Y. Chou. Fabrication of 10 nm enclosed nanofluidic channels. *Applied Physics Letters*, 81(1):174–176, 2002. doi: 10.1063/1.1489102.

C. Casiraghi, A. C. Ferrari, R. Ohr, D. Chu, and J. Robertson. Surface properties of ultra-thin tetrahedral amorphous carbon films for magnetic storage technology. *Diamond and Related Materials*, 13(4-8):1416 – 1421, 2004. doi: 10.1016/j.diamond.2003.10.086. 14th European Conference on Diamond, Diamond-Like Materials, Carbon Nanotubes, Nitrides and Silicon Carbide.

Y. Catherine and P. Couderc. Electrical characteristics and growth kinetics in discharges used for plasma deposition of amorphous carbon. *Thin Solid Films*, 144 (2):265 – 280, 1986. doi: 10.1016/0040-6090(86)90419-0.

C.-Y. Chao, W. Fung, and L. Guo. Polymer microring resonators for biochemical sensing applications. *Selected Topics in Quantum Electronics, IEEE Journal of*, 12(1):134–142, 2006. doi: 10.1109/JSTQE.2005.862945.

J. F. Chen, T. L. Laidig, K. E. Wampler, and R. F. Caldwell. Practical method for full-chip optical proximity correction. volume 3051, pages 790–803. SPIE, 1997. doi: 10.1117/12.276060.

J. S. Chen, S. P. Lau, Z. Sun, G. Y. Chen, Y. J. Li, B. K. Tay, and J. W. Chai. Metal-containing amorphous carbon films for hydrophobic application. *Thin Solid Films*, 398-399:110 – 115, 2001. doi: 10.1016/S0040-6090(01)01455-9.

S. Y. Chou and P. R. Krauss. Imprint lithography with sub-10 nm feature size and high throughput. *Microelectronic Engineering*, 35(1-4):237–240, 1997. doi: 10.1016/S0167-9317(96)00097-4.

S. Y. Chou, P. R. Krauss, W. Zhang, L. Guo, and L. Zhuang. Sub-10 nm imprint lithography and applications. volume 15, pages 2897–2904. AVS, 1997. doi: 10.1116/1.589752.

J. W. Coburn and M. Chen. Optical emission spectroscopy of reactive plasmas: A method for correlating emission intensities to reactive particle density. *Journal of Applied Physics*, 51(6):3134–3136, 1980. doi: 10.1063/1.328060.

J. W. Coburn and H. F. Winters. Ion- and electron-assisted gas-surface chemistry—an important effect in plasma etching. *Journal of Applied Physics*, 50(5):3189–3196, 1979. doi: 10.1063/1.326355.

C. Corbella. *Thin film structures of diamond-like carbon prepared by pulsed plasma techniques*. PhD thesis, University of Barcelona, 2006. URL `http://www.tesisenxarxa.net/TDX-0515106-134413`.

C. Corbella. Retarding field ion energy analysis of chf_3+ch_4 plasmas. Internal comunication, 2009.

C. Corbella, M. Vives, G. Oncins, C. Canal, J. L. Andújar, and E. Bertran. Characterization of dlc films obtained at room temperature by pulsed-dc pecvd. *Diamond and Related Materials*, 13(4-8):1494 – 1499, 2004a. doi: 10.1016/j.diamond.2003.10.079. 14th European Conference on Diamond, Diamond-Like Materials, Carbon Nanotubes, Nitrides and Silicon Carbide.

C. Corbella, M. Vives, A. Pinyol, E. Bertran, C. Canal, M. C. Polo, and J. L. Andújar. Preparation of metal (w, mo, nb, ti) containing a-c:h films by reactive magnetron sputtering. *Surface and Coatings Technology*, 177-178:409 – 414, 2004b. doi: 10.1016/j.surfcoat.2003.09.017. Proceedings of the 30th International Conference on Metallurgical Coatings and Thin Films.

C. Corbella, E. Pascual, M. A. Gómez, M. C. Polo, J. García-Céspedes, J. L. Andújar, and E. Bertran. Characterization of diamond-like carbon thin films produced by pulsed-dc low pressure plasma monitored by a langmuir probe in time-resolved mode. *Diamond and Related Materials*, 14(3-7):1062–1066, 2005. doi: 10.1016/j.diamond.2004.12.059.

J. J. Cuomo, J. P. Doyle, J. Bruley, and J. C. Liu. Sputter deposition of dense diamond-like carbon films at low temperature. *Applied Physics Letters*, 58(5):466–468, 1991. doi: 10.1063/1.104609.

C. Della Volpe and S. Siboni. Acidbase surface free energies of solids and the definition of scales in the goodvan osschaudhury theory. *Journal of Adhesion Science and Technology*, 14:235–272(38), 2000. doi: 10.1163/156856100742546.

C. Della Volpe, D. Maniglio, M. Brugnara, S. Siboni, and M. Morra. The solid surface free energy calculation: I. in defense of the multicomponent approach. *Journal of Colloid and Interface Science*, 271(2):434 – 453, 2004. doi: 10.1016/j.jcis.2003.09.049.

C. Donnet. Recent progress on the tribology of doped diamond-like and carbon alloy coatings: a review. *Surface and Coatings Technology*, 100-101:180 – 186, 1998. doi: 10.1016/S0257-8972(97)00611-7.

D. Dorfner, T. Zabel, T. Hürlimann, N. Hauke, L. Frandsen, U. Rant, G. Abstreiter, and J. Finley. Photonic crystal nanostructures for optical biosensing applications. *Biosensors and Bioelectronics*, 24(12):3688 – 3692, 2009. doi: 10.1016/j.bios.2009.05.014.

M. Ebelmann. *Annales des Chimie et des Physique*, 16:129, 1846.

K. Endo and T. Tatsumi. Fluorinated amorphous carbon thin films grown by plasma enhanced chemical vapor deposition for low dielectric constant interlayer dielectrics. *Journal of Applied Physics*, 78(2):1370–1372, 1995. doi: 10.1063/1.360313.

A. Erdemir. The role of hydrogen in tribological properties of diamond-like carbon films. *Surface and Coatings Technology*, 146-147:292–297, 2001. doi: 10.1016/S0257-8972(01)01417-7.

A. Erdemir and C. Donnet. Tribology of diamond-like carbon films: recent progress and future prospects. *Journal of Physics D: Applied Physics*, 39(18):R311, 2006. doi: 10.1088/0022-3727/39/18/R01.

P. J. Fallon, V. S. Veerasamy, C. A. Davis, J. Robertson, G. A. J. Amaratunga, W. I. Milne, and J. Koskinen. Properties of filtered-ion-beam-deposited diamondlike carbon as a function of ion energy. *Phys. Rev. B*, 48(7):4777–4782, 1993. doi: 10.1103/PhysRevB.48.4777.

A. C. Ferrari and J. Robertson. Interpretation of raman spectra of disordered and amorphous carbon. *Phys. Rev. B*, 61(20):14095–14107, 2000. doi: 10.1103/PhysRevB.61.14095.

A. C. Ferrari, S. E. Rodil, J. Robertson, and W. I. Milne. Is stress necessary to stabilise sp3 bonding in diamond-like carbon? *Diamond and Related Materials*, 11(3-6):994 – 999, 2002. doi: 10.1016/S0925-9635(01)00705-1.

A. M. Ferraria, J. Lopes da Silva, and A. M. Botelho do Rego. Xps studies of directly fluorinated hdpe: problems and solutions. *Polymer*, 44(23):7241–7249, 2003. doi: 10.1016/j.polymer.2003.08.038.

D. G. Flagello, B. Arnold, S. Hansen, M. Dusa, R. J. Socha, J. Mulkens, and R. Garreis. Optical lithography in the sub-50-nm regime. volume 5377, pages 21–33. SPIE, 2004. doi: 10.1117/12.535432.

F. M. Fowkes. Determination of interfacial tensions, contact angles, and dispersion forces in surfaces by assuming additivity of intermolecular interactions

in surfaces. *The Journal of Physical Chemistry*, 66(2):382–382, 1962. doi: 10.1021/j100808a524.

F. M. Fowkes. Role of acid-base interfacial bonding in adhesion. *Journal of Adhesion Science and Technology*, 1:7–27(21), 1987. doi: 10.1163/156856187X00049.

R. Gåhlin, M. Larsson, and P. Hedenqvist. Me-c:h coatings in motor vehicles. *Wear*, 249(3-4):302 – 309, 2001. doi: 10.1016/S0043-1648(01)00565-8.

J. E. Gentle. *Numerical Linear Algebra for Applications in Statistics*. Springer, 1998. ISBN 0-387-98542-5.

L. A. Giannuzzi and F. A. Stevie, editors. *Introduction to Focused Ion Beam: Instrumentation, Theory, Techniques and Practice*. Springer-Verlag, 2005. ISBN 0-387-23116-1.

R. Gilmore and R. Hauert. Control of the tribological moisture sensitivity of diamond-like carbon films by alloying with f, ti or si. *Thin Solid Films*, 398-399: 199–204, 2001. doi: 10.1016/S0040-6090(01)01437-7.

B. Glück and W. Höppner. Etching of silicon trenches in cf_4 plasma using photoresist/aluminium masks. *Crystal Research and Technology*, 25(3):277–283, 1990. doi: 10.1002/crat.2170250309.

P. R. Goglia, J. Berkowitz, J. Hoehn, A. Xidis, and L. Stover. Diamond-like carbon applications in high density hard disc recording heads. *Diamond and Related Materials*, 10(2):271 – 277, 2001. doi: 10.1016/S0925-9635(00)00589-6.

J. I. Goldstein, D. E. Newbury, P. Echlin, D. C. Joy, C. Fiori, and E. Lifshin. *Scanning Electron Microscopy and X-Ray Microanalysis*. Plenum Press, 1992. ISBN 0-306-44175-6.

P. Gonon and A. Sylvestre. Dielectric properties of fluorocarbon thin films deposited by radio frequency sputtering of polytetrafluoroethylene. *Journal of Applied Physics*, 92(8):4584–4589, 2002. doi: 10.1063/1.1505983.

R. J. Good and A. K. Hawa. Acid/base components in the molecular theory of adhesion. *The Journal of Adhesion*, 63(1):5 – 13, 1997. doi: 10.1080/00218469708015210.

A. Grill. Diamond-like carbon: state of the art. *Diamond and Related Materials*, 8 (2-5):428 – 434, 1999. doi: 10.1016/S0925-9635(98)00262-3.

M. Grischke, K. Bewilogua, K. Trojan, and H. Dimigen. Application-oriented modifications of deposition processes for diamond-like-carbon-based coatings. *Surface and Coatings Technology*, 74-75(Part 2):739 – 745, 1995. doi: 10.1016/0257-8972(94)08201-4. Fourth International Conference on Plasma Surface Engineering Part 2.

M. Guerino, M. Massi, and R. Mansano. The influence of nitrogen and fluorine on the dielectric constant of hydrogenated amorphous carbon (a-c:h) films. *Microelectronics Journal*, 38(8-9):915 – 918, 2007. doi: 10.1016/j.mejo.2007.04.003.

R. Haerle, E. Riedo, A. Pasquarello, and A. Baldereschi. sp^2/sp^3 hybridization ratio in amorphous carbon from c1s core-level shifts: X-ray photoelectron spectroscopy and first-principles calculation. *Phys. Rev. B*, 65(4):045101, 2001. doi: 10.1103/PhysRevB.65.045101.

J. Han and H. G. Craighead. Separation of Long DNA Molecules in a Microfabricated Entropic Trap Array. *Science*, 288(5468):1026–1029, 2000. doi: 10.1126/science.288.5468.1026.

R. Hauert. An overview on the tribological behavior of diamond-like carbon in technical and medical applications. *Tribology International*, 37(11-12):991 – 1003, 2004. doi: 10.1016/j.triboint.2004.07.017. Novel Carbons in Tribolgy.

R. D. Heidenreich, L. F. Thompson, E. D. Feit, and C. M. Melliar-Smith. Fundamental aspects of electron beam lithography. i. depth-dose response of polymeric electron beam resists. *Journal of Applied Physics*, 44(9):4039–4047, 1973. doi: 10.1063/1.1662892.

J. A. Heimberg, K. J. Wahl, I. L. Singer, and A. Erdemir. Superlow friction behavior of diamond-like carbon coatings: Time and speed effects. *Applied Physics Letters*, 78(17):2449–2451, 2001. doi: 10.1063/1.1366649.

H. Hofsäss, H. Binder, T. Klumpp, and E. Recknagel. Doping and growth of diamond-like carbon films by ion beam deposition. *Diamond and Related Materials*, 3(1-2):137 – 142, 1994. doi: 10.1016/0925-9635(94)90045-0.

L. Holland and S. Ojha. Deposition of hard and insulating carbonaceous films on an r.f. target in a butane plasma. *Thin Solid Films*, 38(2):L17 – L19, 1976. doi: 10.1016/0040-6090(76)90214-5.

F. A. Houle, C. T. Rettner, D. C. Miller, and R. Sooriyakumaran. Antiadhesion considerations for uv nanoimprint lithography. *Applied Physics Letters*, 90(21):213103, 2007. doi: 10.1063/1.2740578.

L. G. Jacobsohn, D. F. Franceschini, M. E. H. M. da Costa, and J. F. L. Freire. Structural and mechanical characterization of fluorinated amorphous-carbon films deposited by plasma decomposition of cf_4–ch_4 gas mixtures. *Journal of Vacuum Science & Technology A: Vacuum, Surfaces, and Films*, 18(5):2230–2238, 2000. doi: 10.1116/1.1289540.

L. G. Jacobsohn, M. E. H. Maia da Costa, V. J. Trava-Airoldi, and F. L. Freire. Hard amorphous carbon-fluorine films deposited by pecvd using c2h2-cf4 gas mixtures

as precursor atmospheres. *Diamond and Related Materials*, 12(10-11):2037–2041, 2003. doi: 10.1016/S0925-9635(03)00200-0.

F. Jansen, M. Machonkin, S. Kaplan, and S. Hark. The effects of hydrogenation on the properties of ion beam sputter deposited amorphous carbon. *Journal of Vacuum Science & Technology A: Vacuum, Surfaces, and Films*, 3(3):605–609, 1985. doi: 10.1116/1.572960.

H. Jansen, M. de Boer, R. Legtenberg, and M. Elwenspoek. The black silicon method: a universal method for determining the parameter setting of a fluorine-based reactive ion etcher in deep silicon trench etching with profile control. *Journal of Micromechanics and Microengineering*, 5(2):115, 1995. doi: 10.1088/0960-1317/5/2/015.

R. W. Jaszewski, H. Schift, P. Gröning, and G. Margaritondo. Properties of thin anti-adhesive films used for the replication of microstructures in polymers. *Microelectronic Engineering*, 35(1-4):381–384, 1997. doi: 10.1016/S0167-9317(96)00203-1.

R. W. Jaszewski, H. Schift, B. Schnyder, A. Schneuwly, and P. Gröning. The deposition of anti-adhesive ultra-thin teflon-like films and their interaction with polymers during hot embossing. *Applied Surface Science*, 143(1-4):301–308, 1999. doi: 10.1016/S0169-4332(99)00014-8.

M. Jiang and Z. Ning. Influence of deposition pressure on the structure and properties of fluorinated diamond-like carbon films prepared by rf reactive magnetron sputtering. *Surface and Coatings Technology*, 200(12-13):3682 – 3686, 2006. doi: 10.1016/j.surfcoat.2005.03.023.

M.-G. Kang, M.-S. Kim, J. Kim, and L. J. Guo. Organic solar cells using nanoimprinted transparent metal electrodes. *Advanced Materials*, 20(23):4408–4413, 2008. doi: 10.1002/adma.200800750.

H. R. Kaufman. Technology of ion beam sources used in sputtering. *Journal of Vacuum Science and Technology*, 15(2):272–276, 1978. doi: 10.1116/1.569569.

H.-P. Kaukonen and R. M. Nieminen. Molecular-dynamics simulation of the growth of diamondlike films by energetic carbon-atom beams. *Phys. Rev. Lett.*, 68(5): 620–623, 1992. doi: 10.1103/PhysRevLett.68.620.

D. Kawasaki, D. Tsuchimura, W. Choi, Y. Iseri, T. Ando, and H. Tomokage. Scanning probe field emission current measurements on diamond-like carbon films treated by reactive ion etching. *Journal of Physics: Condensed Matter*, 16(2): S301, 2004. doi: 10.1088/0953-8984/16/2/036.

M. Keil, M. Beck, G. Frennesson, E. Theander, E. Bolmsjö, L. Montelius, and B. Heidari. Process development and characterization of antisticking layers on

nickel-based stamps designed for nanoimprint lithography. volume 22, pages 3283–3287. AVS, 2004. doi: 10.1116/1.1824051.

R. Kelsall, I. W. Hamley, and M. Geoghegan, editors. *Nanoscale Science and Technology*. John Wiley & Sons Ltd., 2005. ISBN 0-470-85086-8.

W. M. M. Kessels, J. W. A. M. Gielen, M. C. M. V. de Sanden, L. J. V. Ijzendoorn, E. H. A. Dekempeneer, and D. C. Schram. A model for the deposition of a-c:h using an expanding thermal arc. *Surface and Coatings Technology*, 98(1-3):1584 – 1589, 1998. doi: 10.1016/S0257-8972(97)00358-7.

H. Kim, J.-K. Shin, D.-H. Kwon, H.-I. Seo, and G. S. Lee. Plasma-enhanced chemical vapor deposition growth of fluorinated amorphous carbon thin films using c_4f_8 and si_2h_6/he for low-dielectric-constant intermetallic-layer dielectrics. *Japanese Journal of Applied Physics*, 44(7A):4886–4890, 2005. doi: 10.1143/JJAP.44.4886.

J. Y. Kim, D.-G. Choi, J.-H. Jeong, and E.-S. Lee. Uv-curable nanoimprint resin with enhanced anti-sticking property. *Applied Surface Science*, 254(15):4793 – 4796, 2008. doi: 10.1016/j.apsusc.2008.01.095.

M.-S. Kim, J.-S. Kim, J. C. Cho, M. Shtein, L. J. Guo, and J. Kim. Flexible conjugated polymer photovoltaic cells with controlled heterojunctions fabricated using nanoimprint lithography. *Applied Physics Letters*, 90(12):123113, 2007. doi: 10.1063/1.2715036.

L. D. B. Kiss, J.-P. Nicolai, W. T. Conner, and H. H. Sawin. Cf and cf_2 actinometry in a cf_4/ar plasma. *Journal of Applied Physics*, 71(7):3186–3192, 1992. doi: 10.1063/1.350961.

M. Kiuru, E. Alakoski, V.-M. Tiainen, R. Lappalainen, and A. Anttila. Tantalum as a buffer layer in diamond-like carbon coated artificial hip joints. *Journal of Biomedical Materials Research Part B: Applied Biomaterials*, 66B(1):425–428, 2003. doi: 10.1002/jbm.b.10029.

P. Koidl, C. Wild, B. Dischler, J. Wagner, and M. Ramsteiner. Plasma deposition, properties and structure of amorphous hydrogenated carbon films. *Materials Science Forum*, 52:41–70, 1990. doi: 10.4028/www.scientific.net/MSF.52-53.41.

J. Koike, D. M. Parkin, and T. E. Mitchell. Displacement threshold energy for type iia diamond. *Applied Physics Letters*, 60(12):1450–1452, 1992. doi: 10.1063/1.107267.

R. Korotkov, T. Goff, and P. Ricou. Fluorination of polymethylmethacrylate with sf6 and hexafluoropropylene using dielectric barrier discharge system at atmospheric pressure. *Surface and Coatings Technology*, 201(16-17):7207 – 7215, 2007. doi: 10.1016/j.surfcoat.2007.01.028.

K.-R. Lee, K. Y. Eun, I. Kim, and J. Kim. Design of w buffer layer for adhesion improvement of dlc films on tool steels. *Thin Solid Films*, 377-378:261 – 268, 2000. doi: 10.1016/S0040-6090(00)01429-2.

R. Legtenberg, H. Jansen, M. de Boer, and M. Elwenspoek. Anisotropic reactive ion etching of silicon using $sf_6/o_2/chf_3$ gas mixtures. *Journal of The Electrochemical Society*, 142(6):2020–2028, 1995. doi: 10.1149/1.2044234.

G. Leroy, D. Temsamani, M. Sana, and C. Wilante. Refinement and extension of the table of standard energies for bonds involving hydrogen and various atoms of groups iv to vii of the periodic table. *Journal of Molecular Structure*, 300:373 – 383, 1993. doi: 10.1016/0022-2860(93)87032-5.

M. D. Levenson, N. S. Viswanathan, and R. A. Simpson. Improving resolution in photolithography with a phase-shifting mask. *IEEE Transactions on Electron Devices*, 29(12):1828–1836, 1982.

K. Y. Li, Z. F. Zhou, I. Bello, C. S. Lee, and S. T. Lee. Study of tribological performance of ecr-cvd diamond-like carbon coatings on steel substrates: Part 1. the effect of processing parameters and operating conditions. *Wear*, 258(10): 1577–1588, 2005. doi: 10.1016/j.wear.2004.10.006.

D. R. Lide, editor. *CRC Handbook of Chemistry and Physics, Internet Version 2005.* CRC Press, Boca Raton, FL, USA, 2005. ISBN 978-0849304859.

M. A. Lieberman and A. J. Lichtenberg. *Principles of plasma discharges and materials processing.* Wiley, 1994.

E. M. Lifshitz. The theory of molecular attractive forces between solids. *Soviet Physics - Journal of Experimental and Theoretical Physics - USSR*, 2(1):73–83, 1956.

Y. Lifshitz. Hydrogen-free amorphous carbon films: correlation between growth conditions and properties. *Diamond and Related Materials*, 5(3-5):388 – 400, 1996. doi: 10.1016/0925-9635(95)00445-9. International Journal on the Science and Technology of Diamond and Related Materials.

Y. Lifshitz. Diamond-like carbon – present status. *Diamond and Related Materials*, 8(8-9):1659 – 1676, 1999. doi: 10.1016/S0925-9635(99)00087-4.

Y. Lifshitz, S. R. Kasi, and J. W. Rabalais. Subplantation model for film growth from hyperthermal species: Application to diamond. *Phys. Rev. Lett.*, 62(11): 1290–1293, 1989. doi: 10.1103/PhysRevLett.62.1290.

Y. Lifshitz, S. R. Kasi, J. W. Rabalais, and W. Eckstein. Subplantation model for film growth from hyperthermal species. *Phys. Rev. B*, 41(15):10468–10480, 1990. doi: 10.1103/PhysRevB.41.10468.

Y. Lifshitz, G. D. Lempert, and E. Grossman. Substantiation of subplantation model for diamondlike film growth by atomic force microscopy. *Phys. Rev. Lett.*, 72(17): 2753–2756, 1994. doi: 10.1103/PhysRevLett.72.2753.

A.-S. Loir, F. Garrelie, C. Donnet, J.-L. Subtil, M. Belin, B. Forest, F. Rogemond, and P. Laporte. Mechanical and tribological characterization of tetrahedral diamond-like carbon deposited by femtosecond pulsed laser deposition on pre-treated orthopaedic biomaterials. *Applied Surface Science*, 247(1-4):225 – 231, 2005. doi: 10.1016/j.apsusc.2005.01.129. Proceedings of the European Materials Research Society 2004 - Symposium N.

C. López. Materials aspects of photonic crystals. *Advanced Materials*, 15(20):1679–1704, 2003. doi: 10.1002/adma.200300386.

L. Mao and H. Ye. New development of one-dimensional si/sio2 photonic crystals filter for thermophotovoltaic applications. *Renewable Energy*, 35(1):249–256, 1 2010. doi: 10.1016/j.renene.2009.06.013.

P. J. Martin, S. W. Filipczuk, R. P. Netterfield, J. S. Field, D. F. Whitnall, and D. R. McKenzie. Structure and hardness of diamond-like carbon films prepared by arc evaporation. *Journal of Materials Science Letters*, 7(4):410–412, 1988. doi: 10.1007/BF01730760.

L. Martinu and D. Poitras. Plasma deposition of optical films and coatings: A review. *Journal of Vacuum Science & Technology A: Vacuum, Surfaces, and Films*, 18(6): 2619–2645, 2000. doi: 10.1116/1.1314395.

D. R. McKenzie. Generation and applications of compressive stress induced by low energy ion beam bombardment. volume 11, pages 1928–1935. AVS, 1993. doi: 10.1116/1.586524. Proceedings of the Topical Conference on Energetic Condensation.

D. R. McKenzie. Tetrahedral bonding in amorphous carbon. *Reports on Progress in Physics*, 59(12):1611, 1996. doi: 10.1088/0034-4885/59/12/002.

D. R. McKenzie, D. Muller, and B. A. Pailthorpe. Compressive-stress-induced formation of thin-film tetrahedral amorphous carbon. *Phys. Rev. Lett.*, 67(6):773–776, 1991. doi: 10.1103/PhysRevLett.67.773.

T. Michler, M. Grischke, I. Traus, K. Bewilogua, and H. Dimigen. Dlc films deposited by bipolar pulsed dc pacvd. *Diamond and Related Materials*, 7(2-5):459–462, 1998. doi: 10.1016/S0925-9635(97)00236-7.

K. Mittal, editor. *Acid-Base Interactions: Relevance to Adhesion Science and Technology*, volume 2. VSP, 2000.

S. Miyagawa, S. Nakao, M. Ikeyama, and Y. Miyagawa. Deposition of diamond-like carbon films using plasma based ion implantation with bipolar pulses. *Surface*

and Coatings Technology, 156(1-3):322 – 327, 2002. doi: 10.1016/S0257-8972(02)00101-9.

T. Miyamoto, R. Kaneko, and S. Miyake. Tribological characteristics of amorphous carbon films investigated by point contact microscopy. volume 9, pages 1336–1339. AVS, 1991. doi: 10.1116/1.585191.

T. Miyazawa, S. Misawa, S. Yoshida, and S. ichi Gonda. Preparation and structure of carbon film deposited by a mass-separated c^+ ion beam. *Journal of Applied Physics*, 55(1):188–193, 1984. doi: 10.1063/1.332862.

T. Mori and Y. Namba. Hard diamondlike carbon films deposited by ionized deposition of methane gas. *Journal of Vacuum Science & Technology A: Vacuum, Surfaces, and Films*, 1(1):23–27, 1983. doi: 10.1116/1.572304.

N. A. Morrison, S. E. Rodil, A. C. Ferrari, J. Robertson, and W. I. Milne. High rate deposition of ta-c:h using an electron cyclotron wave resonance plasma source. *Thin Solid Films*, 337(1-2):71 – 73, 1999. doi: 10.1016/S0040-6090(98)01187-0.

T. W. Mountsier and J. A. Samuels. Precursor selection for plasma deposited fluorinated amorphous carbon films. *Thin Solid Films*, 332(1-2):362 – 368, 1998. doi: 10.1016/S0040-6090(98)01202-4.

M. Murakawa, T. Komori, S. Takeuchi, and K. Miyoshi. Performance of a rotating gear pair coated with an amorphous carbon film under a loss-of-lubrication condition. *Surface and Coatings Technology*, 120-121:646 – 652, 1999. doi: 10.1016/S0257-8972(99)00437-5.

K. Nakamatsu, N. Yamada, K. Kanda, Y. Haruyama, and S. Matsui. Fluorinated diamond-like carbon coating as antisticking layer on nanoimprint mold. *Japanese Journal of Applied Physics*, 45(35):L954–L956, 2006. doi: 10.1143/JJAP.45.L954.

G. Nansé, E. Papirer, P. Fioux, F. Moguet, and A. Tressaud. Fluorination of carbon blacks: An x-ray photoelectron spectroscopy study: I. a literature review of xps studies of fluorinated carbons. xps investigation of some reference compounds. *Carbon*, 35(2):175–194, 1997. doi: 10.1016/S0008-6223(96)00095-4.

M. Nosonovskii and B. Bhushan. *Multiscale dissipative mechanisms and hierarchical surfaces : friction, superhydrophobicity, and biomimetics*. Springer, Berlin, 2008. ISBN 9783540784241 3540784241.

F. E. M. O'Brien. The control of humidity by saturated salt solutions. *Journal of Scientific Instruments*, 25(3):73–76, 1948. doi: 10.1088/0950-7671/25/3/305.

M. Ohring. *Materials Science of Thin Films*. Academic Press London, 2002.

S. Ojha and L. Holland. Some characteristics of hard carbonaceous films. *Thin Solid Films*, 40:L31 – L32, 1977. doi: 10.1016/0040-6090(77)90097-9.

A. Olziersky, A. Vilà, M. Rubio-Roy, E. Bertran, and J. Fontcuberta. Magnetic domain wall pinning by focused ion beam milling of permalloy layers. *Microelectronic Engineering*, 86(4-6):878 – 881, 2009. doi: 10.1016/j.mee.2008.12.028. MNE '08 - The 34th International Conference on Micro- and Nano-Engineering (MNE).

G. Owen. Electron lithography for the fabrication of microelectronic devices. *Reports on Progress in Physics*, 48(6):795–851, 1985. doi: 10.1088/0034-4885/48/6/002.

S.-H. Park, T.-W. Lim, D.-Y. Yang, J.-H. Jeong, K.-D. Kim, K.-S. Lee, and H.-J. Kong. Effective fabrication of three-dimensional nano/microstructures in a single step using multilayered stamp. *Applied Physics Letters*, 88(20):203105, 2006. doi: 10.1063/1.2204448.

S. Park, H. Schift, C. Padeste, B. Schnyder, R. Kötz, and J. Gobrecht. Anti-adhesive layers on nickel stamps for nanoimprint lithography. *Microelectronic Engineering*, 73-74:196–201, 2004. doi: 10.1016/j.mee.2004.02.040.

R. W. B. Pearse and A. G. Gaydon. *The identification of molecular spectra*. Chapman and Hall, 1976.

A. Pépin, P. Youinou, V. Studer, A. Lebib, and Y. Chen. Nanoimprint lithography for the fabrication of dna electrophoresis chips. *Microelectronic Engineering*, 61-62:927 – 932, 2002. doi: 10.1016/S0167-9317(02)00511-7.

M. C. Petty. *Langmuir-Blodgett films: an introduction*. Cambridge University Press, 1996. ISBN 0-521-41396-6.

H. C. Pfeiffer, R. S. Dhaliwal, S. D. Golladay, S. K. Doran, M. S. Gordon, T. R. Groves, R. A. Kendall, J. E. Lieberman, P. F. Petric, D. J. Pinckney, R. J. Quickle, C. F. Robinson, J. D. Rockrohr, J. J. Senesi, W. Stickel, E. V. Tressler, A. Tanimoto, T. Yamaguchi, K. Okamoto, K. Suzuki, T. Okino, S. Kawata, K. Morita, S. C. Suziki, H. Shimizu, S. Kojima, G. Varnell, W. T. Novak, D. P. Stumbo, and M. Sogard. Projection reduction exposure with variable axis immersion lenses: Next generation lithography. volume 17, pages 2840–2846. AVS, 1999. doi: 10.1116/1.591080.

M. C. Polo, J. L. Andújar, A. Hart, J. Robertson, and W. I. Milne. Preparation of tetrahedral amorphous carbon films by filtered cathodic vacuum arc deposition. *Diamond and Related Materials*, 9(3-6):663 – 667, 2000. doi: 10.1016/S0925-9635(99)00339-8.

S. Portal, M. Rubio-Roy, C. Corbella, M. Vallvé, J. Ignes-Mullol, and E. Bertran. Influence of incident ion beam angle on dry etching of silica sub-micron particles deposited on si substrates. *Thin Solid Films*, 518(5):1543 – 1548, 2009. doi: 10.1016/j.tsf.2009.09.077. Proceedings of the 36th International Conference on Metallurgical Coatings and Thin Films.

J. J. Pouch and S. A. Alterovitz. Preparation and properties of high density, hydrogen free hard carbon films with direct ion beam or arc discharge deposition. *Materials Science Forum*, 52-53:197–216, 1990. doi: 10.4028/www.scientific.net/MSF.52-53.197.

W. Press, S. Teukolsky, W. Vetterling, and B. Flannery. *Numerical Recipes: The Art of Scientific Computing*. Springer-Verlag, 2007. ISBN 978-0521880688.

S. R. Quake and A. Scherer. From Micro- to Nanofabrication with Soft Materials. *Science*, 290(5496):1536–1540, 2000. doi: 10.1126/science.290.5496.1536.

P. Rai-Choudhury, editor. *Handbook of Microlithography, Micromachining and Microfabrication; Volume 1: Microlithography*. Number 0954-0695. SPIE, 1997.

R. M. Reano and S. W. Pang. Sealed three-dimensional nanochannels. volume 23, pages 2995–2999. AVS, 2005. doi: 10.1116/1.2121728.

J. Robertson. Deposition of diamond-like carbon. *Philosophical Transactions of the Royal Society of London. Series A: Physical and Engineering Sciences*, 342(1664): 277–286, 1993. doi: 10.1098/rsta.1993.0021.

J. Robertson. Diamond-like carbon. *Pure and Applied Chemistry*, 66(9):1789–1796, 1994a. doi: 10.1351/pac199466091789. 8th International Conference on High Temperature Materials Chemistry (HTMC VIII), Vienna, Austria.

J. Robertson. Diamond-like amorphous carbon. *Materials Science and Engineering: R: Reports*, 37(4-6):129 – 281, 2002. doi: 10.1016/S0927-796X(02)00005-0.

J. Robertson. Requirements of ultrathin carbon coatings for magnetic storage technology. *Tribology International*, 36(4-6):405 – 415, 2003. doi: 10.1016/S0301-679X(02)00216-5. Tribology of Information Storage Devices 2001.

J. Robertson. The deposition mechanism of diamond-like a-c and a-c:h. *Diamond and Related Materials*, 3(4-6):361 – 368, 1994b. doi: 10.1016/0925-9635(94)90186-4. Proceedings of the 4th European Conference on Diamond, Diamond-like and Related Materials.

S. M. Rossnagel. Thin film deposition with physical vapor deposition and related technologies. *Journal of Vacuum Science & Technology A: Vacuum, Surfaces, and Films*, 21(5):S74–S87, 2003. doi: 10.1116/1.1600450.

R. K. Roy, H.-W. Choi, S.-J. Park, and K.-R. Lee. Surface energy of the plasma treated si incorporated diamond-like carbon films. *Diamond and Related Materials*, 16(9):1732 – 1738, 2007. doi: 10.1016/j.diamond.2007.06.002.

M. Rubio-Roy, C. Corbella, J. García-Céspedes, M. C. Polo, E. Pascual, J. L. Andújar, and E. Bertran. Diamond like carbon films deposited from graphite target by

asymmetric bipolar pulsed-dc magnetron sputtering. *Diamond and Related Materials*, 16(4-7):1286–1290, 2007. doi: 10.1016/j.diamond.2006.12.054. Proceedings of Diamond 2006, the 17th European Conference on Diamond, Diamond-Like Materials, Carbon Nanotubes, Nitrides and Silicon Carbide.

M. Rubio-Roy, E. Bertran, E. Pascual, M. C. Polo, and J. L. Andújar. Fluorinated dlc deposited by pulsed-dc plasma for antisticking surface applications. *Diamond and Related Materials*, 17(7-10):1728–1732, 2008a. doi: 10.1016/j.diamond.2007.12.008. Proceedings of Diamond 2007, the 18th European Conference on Diamond, Diamond-Like Materials, Carbon Nanotubes, Nitrides and Silicon Carbide.

M. Rubio-Roy, E. Pascual, M. C. Polo, J. L. Andújar, and E. Bertran. Structural and optical properties of diamond like thin films deposited by asymmetric bipolar pulsed-dc reactive magnetron sputtering. *Surface and Coatings Technology*, 202 (11):2354–2357, 2008b. doi: 10.1016/j.surfcoat.2007.08.044. Protective Coatings and Thin Films 07, E-MRS Spring Meeting.

M. Rubio-Roy, C. Corbella, E. Bertran, S. Portal, M. Polo, E. Pascual, and J. Andújar. Effects of environmental conditions on fluorinated diamond-like carbon tribology. *Diamond and Related Materials*, 18(5-8):923 – 926, 2009. doi: 10.1016/j.diamond.2009.02.006. Proceedings of Diamond 2008, the 19th European Conference on Diamond, Diamond-Like Materials, Carbon Nanotubes, Nitrides and Silicon Carbide.

V. Saikko, T. Ahlroos, O. Calonius, and J. Keränen. Wear simulation of total hip prostheses with polyethylene against cocr, alumina and diamond-like carbon. *Biomaterials*, 22(12):1507 – 1514, 2001. doi: 10.1016/S0142-9612(00)00306-9.

T. Saito, T. Hasebe, S. Yohena, Y. Matsuoka, A. Kamijo, K. Takahashi, and T. Suzuki. Antithrombogenicity of fluorinated diamond-like carbon films. *Diamond and Related Materials*, 14(3-7):1116 – 1119, 2005. doi: 10.1016/j.diamond.2004.09.017. Proceedings of Diamond 2004, the 15th European Conference on Diamond, Diamond-Like Materials, Carbon Nanotubes, Nitrides and Silicon Carbide.

N. Savvides. Deposition parameters and film properties of hydrogenated amorphous silicon prepared by high rate dc planar magnetron reactive sputtering. *Journal of Applied Physics*, 55(12):4232–4238, 1984. doi: 10.1063/1.333024.

H.-J. Scheibe and B. Schultrich. Dlc film deposition by laser-arc and study of properties. *Thin Solid Films*, 246(1-2):92 – 102, 1994. doi: 10.1016/0040-6090(94)90737-4. Special Issue: Frontiers in Thin Film Research.

H. Schift, S. Saxer, S. Park, C. Padeste, U. Pieles, and J. Gobrecht. Controlled co-evaporation of silanes for nanoimprint stamps. *Nanotechnology*, 16(5):S171–S175, 2005. doi: 10.1088/0957-4484/16/5/007.

H. Schulz, F. Osenberg, J. Engemann, and H.-C. Scheer. Mask fabrication by nanoimprint lithography using antisticking layers. volume 3996, pages 244–249. SPIE, 2000. doi: 10.1117/12.377114.

J. Schulze, D. Luggenholscher, and U. Czarnetzki. Instabilities in capacitively coupled radio-frequency discharges. *IEEE Transactions on Plasma Science*, 36(4): 1402–1403, 2008. doi: 10.1109/TPS.2008.923829.

M. Schvartzman and S. J. Wind. Plasma fluorination of diamond-like carbon surfaces: mechanism and application to nanoimprint lithography. *Nanotechnology*, 20(14):145306, 2009. doi: 10.1088/0957-4484/20/14/145306.

T. Schwarz-Selinger, V. Dose, W. Jacob, and A. von Keudell. Quantification of a radical beam source for methyl radicals. *Journal of Vacuum Science & Technology A: Vacuum, Surfaces, and Films*, 19(1):101–107, 2001. doi: 10.1116/1.1326939.

S. R. P. Silva, editor. *Properties of amorphous carbon*. EMIS datareviews. INSPEC, IEE, 2003. ISBN 978-0-86341-777-1.

S. Silva, J. Carey, R. Khan, E. Gerstner, and J. Anguita. Amorphous carbon thin films. In H. S. Nalwa, M.Sc., and Ph.D., editors, *Handbook of Thin Films*, pages 403 – 506. Academic Press, Burlington, 2002. ISBN 978-0-12-512908-4. doi: 10.1016/B978-012512908-4/50059-X.

J. P. Simko, G. S. Oehrlein, and T. M. Mayer. Removal of fluorocarbon residues on cf_4/h_2 reactive-ion-etched silicon surfaces using a hydrogen plasma. *Journal of The Electrochemical Society*, 138(1):277–284, 1991. doi: 10.1149/1.2085555.

D. L. Spears and H. I. Smith. X-ray lithography - new high-resolution replication process. *Solid State Technology*, 15(7):21, 1972.

E. G. Spencer, P. H. Schmidt, D. C. Joy, and F. J. Sansalone. Ion-beam-deposited polycrystalline diamondlike films. *Applied Physics Letters*, 29(2):118–120, 1976. doi: 10.1063/1.88963.

W. Stöber, A. Fink, and E. Bohn. Controlled growth of monodisperse silica spheres in the micron size range. *Journal of Colloid and Interface Science*, 26(1):62 – 69, 1968. doi: 10.1016/0021-9797(68)90272-5.

G. G. Stoney. The tension of metallic films deposited by electrolysis. *Proceedings of the Royal Society of London. Series A*, 82(553):172–175, 1909. doi: 10.1098/rspa.1909.0021.

V. Studer, A. Pépin, Y. Chen, and A. Ajdari. Fabrication of microfluidic devices for ac electrokinetic fluid pumping. *Microelectronic Engineering*, 61-62:915 – 920, 2002. doi: 10.1016/S0167-9317(02)00518-X.

G. Tang, X. Ma, M. Sun, and X. Li. Mechanical characterization of ultra-thin fluorocarbon films deposited by r.f. magnetron sputtering. *Carbon*, 43(2):345 – 350, 2005. doi: 10.1016/j.carbon.2004.09.022.

L. Tao, S. Ramachandran, C. T. Nelson, M. Lin, L. J. Overzet, M. Goeckner, G. Lee, C. G. Willson, W. Wu, and W. Hu. Durable diamond-like carbon templates for uv nanoimprint lithography. *Nanotechnology*, 19(10), 2008. doi: 10.1088/0957-4484/19/10/105302.

S. C. Trippe, R. D. Mansano, F. M. Costa, and R. F. Silva. Mechanical properties evaluation of fluor-doped diamond-like carbon coatings by nanoindentation. *Thin Solid Films*, 446(1):85 – 90, 2004. doi: 10.1016/j.tsf.2003.08.069.

E. A. Truesdale and G. Smolinsky. The effect of added hydrogen on the rf discharge chemistry of cf_4, cf_3h, and c_2f_6. *Journal of Applied Physics*, 50(11):6594–6599, 1979. doi: 10.1063/1.325908.

Y.-Y. Tu, T. J. Chuang, and H. F. Winters. Chemical sputtering of fluorinated silicon. *Phys. Rev. B*, 23(2):823–835, 1981. doi: 10.1103/PhysRevB.23.823.

S. C. Tung and H. Gao. Tribological characteristics and surface interaction between piston ring coatings and a blend of energy-conserving oils and ethanol fuels. *Wear*, 255(7-12):1276 – 1285, 2003. doi: 10.1016/S0043-1648(03)00240-0. 14th International Conference on Wear of Materials.

C. J. van Oss. *Interfacial Forces in Aqueous Media*. Marcel Dekker, Inc., 1994.

C. J. van Oss, R. J. Good, and M. K. Chaudhury. The role of van der waals forces and hydrogen bonds in "hydrophobic interactions" between biopolymers and low energy surfaces. *Journal of Colloid and Interface Science*, 111(2):378–390, 1986. doi: 10.1016/0021-9797(86)90041-X.

C. J. van Oss, M. K. Chaudhury, and R. J. Good. Monopolar surfaces. *Advances in Colloid and Interface Science*, 28:35 – 64, 1987. doi: 10.1016/0001-8686(87)80008-8.

C. J. van Oss, R. F. Giese, and W. Wu. On the predominant electron-donicity of polar solid surfaces. *The Journal of Adhesion*, 63(1):71 – 88, 1997. doi: 10.1080/00218469708015214.

W. Vassell, A. Gangopadhyay, T. Potter, M. Tamor, and M. Rokosz. Characterization of silicon-stabilized amorphous hydrogenated carbon. *Journal of Materials Engineering and Performance*, 6(4):426–432, 1997. doi: 10.1007/s11665-997-0112-2.

A. A. Voevodin and M. S. Donley. Preparation of amorphous diamond-like carbon by pulsed laser deposition: a critical review. *Surface and Coatings Technology*, 82(3):199 – 213, 1996. doi: 10.1016/0257-8972(95)02734-3.

A. von Keudell and W. Jacob. Growth and erosion of hydrocarbon films investigated by in situ ellipsometry. *Journal of Applied Physics*, 79(2):1092–1098, 1996. doi: 10.1063/1.360796.

A. von Keudell, T. Schwarz-Selinger, and W. Jacob. Simultaneous interaction of methyl radicals and atomic hydrogen with amorphous hydrogenated carbon films. *Journal of Applied Physics*, 89(5):2979–2986, 2001. doi: 10.1063/1.1343894.

M. Weiler, S. Sattel, T. Giessen, K. Jung, H. Ehrhardt, V. S. Veerasamy, and J. Robertson. Preparation and properties of highly tetrahedral hydrogenated amorphous carbon. *Phys. Rev. B*, 53(3):1594–1608, 1996. doi: 10.1103/PhysRevB.53.1594.

C. Weissmantel, K. Bewilogua, D. Dietrich, H. J. Erler, H. J. Hinneberg, S. Klose, W. Nowick, and G. Reisse. Structure and properties of quasi-amorphous films prepared by ion beam techniques. *Thin Solid Films*, 72(1):19 – 32, 1980. doi: 10.1016/0040-6090(80)90554-4.

C. Weissmantel. Ion-based growth of special films: Techniques and mechanisms. *Thin Solid Films*, 92(1-2):55 – 63, 1982. doi: 10.1016/0040-6090(82)90187-0.

E. J. Winder and K. K. Gleason. Growth and characterization of fluorocarbon thin films grown from trifluoromethane (chf_3) using pulsed-plasma enhanced cvd. *Journal of Applied Polymer Science*, 78(4):842–849, 2000. doi: 10.1002/1097-4628(20001024)78:4<842::AID-APP180>3.0.CO;2-J.

H. F. Winters, J. W. Coburn, and T. J. Chuang. Surface processes in plasma-assisted etching environments. *Journal of Vacuum Science & Technology B: Microelectronics and Nanometer Structures*, 1(2):469–480, 1983. doi: 10.1116/1.582629.

C.-W. Wu, Y.-K. Shen, S.-Y. Chuang, and C. Wei. Anti-adhesive effects of diverse self-assembled monolayers in nanoimprint lithography. *Sensors and Actuators A: Physical*, 139(1-2):145 – 151, 2007. doi: 10.1016/j.sna.2006.10.017. Selected Papers From the Asia-Pacific Conference of Transducers and Micro-Nano Technology (APCOT 2006), Asia-Pacific Conference of Transducers and Micro-Nano technology.

S. Wu. *Polymer interface and adhesion*. Marcel Dekker, Inc., 1982. ISBN 9780824715335.

Y. Xin, Z. Y. Ning, C. Ye, X. H. Lu, S. L. Xiang, W. Du, S. Huang, J. Chen, and S. H. Cheng. Optical emission study of ch_4+chf_3 ecr plasma and properties of a-c:f:h films. *Surface and Coatings Technology*, 173(2-3):172 – 177, 2003. doi: 10.1016/S0257-8972(03)00624-8.

T. Young. An essay on the cohesion of fluids. *Philosophical Transactions of the Royal Society of London (1776-1886)*, 95(-1):65–87, 1805. doi: 10.1098/rstl.1805.0005.

G. Q. Yu, B. K. Tay, Z. Sun, and L. K. Pan. Properties of fluorinated amorphous diamond like carbon films by pecvd. *Applied Surface Science*, 219(3-4):228 – 237, 2003. doi: 10.1016/S0169-4332(03)00644-5.

F. Zernike. Overview of extreme ultraviolet lithography. volume 2322, pages 430–433. SPIE, 1994. doi: 10.1117/12.195842.

P. Zhang, B. K. Tay, G. Q. Yu, S. P. Lau, and Y. Q. Fu. Surface energy of metal containing amorphous carbon films deposited by filtered cathodic vacuum arc. *Diamond and Related Materials*, 13(3):459 – 464, 2004. doi: 10.1016/j.diamond.2003.11.083.

Y. X. Zhuang and O. Hansen. Correlation of effective dispersive and polar surface energies in heterogeneous self-assembled monolayer coatings. *Langmuir*, 25(10):5437–5441, 2009. doi: 10.1021/la804318p.

W. A. Zisman. *Relation of the Equilibrium Contact Angle to Liquid and Solid Constitution*, pages 1–51. American Chemical Society, Washington, D.C., 1964. ISBN 0-8412-0044-0. doi: 10.1021/ba-1964-0043.ch001.

J. W. Zou, K. Reichelt, K. Schmidt, and B. Dischler. The deposition and study of hard carbon films. *Journal of Applied Physics*, 65(10):3914–3918, 1989. doi: 10.1063/1.343355.

Appendix

A

Solving overdetermined linear equations systems

The problem of solving an overdetermined linear equation system of m equations and n unknowns ($n \leq m$) is represented in matrix terms[1] by the vectors $X \in \mathbb{R}^n$ and $B \in \mathbb{R}^m$ and the matrix $A \in \mathbb{R}^{m \times n}$. The solution is defined as the "best" approximation of AX to B. The common choice of defining "best" is usually the Euclidean norm ($\|\cdot\|$):

$$\rho = \min_X \|AX - B\|_2 = \min_X \sum_{i=0}^{m} s_i^2 \tag{A.1}$$

This problem is called a linear least square problem, X being a solution of the system $AX = B$. $S = B - AX$ is the residual vector.

If we develop (A.1), we get:

$$\frac{\partial \rho}{\partial x_j} = 2 \sum_i s_i \frac{\partial s_i}{\partial x_j}, \qquad (j = 1, 2, \ldots, n)$$

and since $s_i = b_i - \sum_{j=1}^{n} a_{ij} x_j$,

$$\frac{\partial \rho}{\partial x_j} = -2 \sum_{i=1}^{m} a_{ij} \left(b_i - \sum_{k=1}^{n} a_{ik} x_k \right)$$

Minimizing ($\partial / \partial x_j = 0$) yields:

$$\sum_{i=1}^{m} \sum_{k=1}^{n} a_{ij} a_{ik} x_k = \sum_{i=1}^{m} a_{ij} b_i, \qquad (j = 1, 2, \ldots, n)$$

which written in matrix terms is:

$$\left(A^{\mathrm{T}} A\right) X = A^{\mathrm{T}} B \tag{A.2}$$

[1] In this appendix, vectors and matrices are represented by capital letters (e.g.: X) while their elements and other scalars are represented in lower-case (ρ or x_{ij}).

The solution of the above normal equations yields the vector X of optimal parameter values. However, a more numerically stable way of solving the least squares problem (by not computing $A^{\mathrm{T}}A$) is to do an orthogonal decomposition of A. The one chosen in this thesis has been the QR decomposition:

Matrix A is factored as QR where $Q \in \mathbb{R}^{m\times n}$ is orthogonal ($Q^{\mathrm{T}}Q = \mathrm{I}$) and $R \in \mathbb{R}^{n\times n}$ is upper triangular with $r_{ii} > 0$. Then, we can rewrite (A.2) as:

$$\begin{aligned} A^{\mathrm{T}}AX &= A^{\mathrm{T}}B \\ R^{\mathrm{T}}Q^{\mathrm{T}}QRX &= R^{\mathrm{T}}Q^{\mathrm{T}}B \\ R^{\mathrm{T}}RX &= R^{\mathrm{T}}Q^{\mathrm{T}}B \\ RX &= Q^{\mathrm{T}}B \end{aligned}$$

where Q orthogonality and R non-singularity have been used in the third and fourth steps, respectively.

The algorithm consists on:

- QR factorize A
- compute $Q^{\mathrm{T}}B$
- solve $RX = Q^{\mathrm{T}}B$ by backward substitution (R upper triangular matrix)

The QR factorization algorithm can be done using different orthogonalization methods. Here, the Householder reflection (with better stability than Gram-Schmidt) will be described for reference [Gentle, 1998; Press et al., 2007].

The process consists on repeating the Householder transformation $\min(m-1, n)$ times, indexed by j starting at 0. A vector $X_j \in \mathbb{R}^{m-j}$ is chosen to be the first column of A'_j ($A'_0 \equiv A$), and $\alpha_j \in \mathbb{R}$ is defined as $\alpha_j \equiv \|X_j\|$. Then, $U, V \in \mathbb{R}^{m-j}$ and $Q_j \in \mathbb{R}^{(m-j)\times(m-j)}$ are defined as:

$$\begin{aligned} U &= X - \alpha \begin{pmatrix} 1 \\ 0 \\ \vdots \\ 0 \end{pmatrix} \\ V &= \frac{U}{\|U\|} \\ Q_j &= \mathrm{I}^{m-j} - 2VV^{\mathrm{T}} \end{aligned}$$

with $\mathrm{I}^k \in \mathbb{R}^{k\times k}$ being a unitary matrix.

This way, the $j+1$ first columns of $\prod_j Q_j A$ are upper triangular and define the next A'_j. For example, for $j = 0$:

$$Q_0 A = \begin{pmatrix} \alpha_0 & \star & \dots & \star \\ 0 & & & \\ \vdots & & A'_1 & \\ 0 & & & \end{pmatrix}$$

When the transformation is finished, Q and R are:

$$\begin{aligned} R &= Q_{\min(m-1,n)} \cdots Q_1 Q_0 A \\ Q &= Q_0^{\mathrm{T}} Q_1^{\mathrm{T}} \cdots Q_{\min(m-1,n)}^{\mathrm{T}} \end{aligned}$$

B
Sample list

B.1 Films sample list

Pressure has always been kept at 10 Pa for all the processes. For 08E2901 and older, an automatic pressure regulation system was used to that pressure is more stable during the process.

sample	Φ_{CH_4} (sccm)	Φ_{CHF_3} (sccm)	P (W)[1]	ν (kHz)	τ_+ (ns)	t (s)	cleaning[2]	buffer[3]
07A0901	10	1	55	100	2016	300	no	no
07A1101	8	2	56	100	2016	300	yes	no
07A1501	8	2	56	100	2016	300	yes	yes, 60 s
07A1601	6	4	56	100	2016	300	yes, 420 s	yes, 120 s
07A1709	4	6	56	100	2016	300	yes	yes, 60 s
07A1710	2	8	56	100	2016	300	yes	yes, 60 s
07A1801	2	8	15	100	2016	300	yes	yes, 60 s
07A1802	2	8	100-RF	13560	-	300	yes	yes, 60 s
07A1901	1	9	56	100	2016	300	yes	yes, 60 s
07A2201	0.7	9.3	56	100	2016	300	yes	yes, 60 s
07A2301	1	20	56	100	2016	300	yes	yes, 60 s
07A3101	9	1	56	100	2016	300	yes	yes, 60 s
07B0201	5	5	56	100	2016	300	yes	yes, 65 s
07B0501	3.5	6.5	56	100	2016	300	yes	yes, 60 s

[1] pulsed-DC unless otherwise specified
[2] 100W RF plasma with Ar at 6.0 Pa for 300 s
[3] 10 sccm of CH_4, 10 Pa and 56 W of pulsed-DC at 100 kHz with positive pulse width of 2016 ns, unless otherwise specified. If sample name is used, see buffer layer for that sample

sample	Φ_{CH_4} (sccm)	Φ_{CHF_3} (sccm)	P (W)[1]	ν (kHz)	τ_+ (ns)	t (s)	cleaning[2]	buffer[3]
07D1602	14.4	0	56	100	2016	960	yes	no
07D1901	14.4	0	150	150	2016	964	yes	no
07F0801	18	0	150	150	2016	600	no	yes, 60 s[4]
07F0901	0	25	100	150	2016	600	no	no
07F1001	0	25	100	150	2016	600	no	07F0801
07F1201	0	25	100	150	2016	600	no	07F0801
07F1301	0	25	100	100	2016	600	no	07F0801, 5 s
07F1902	0	25	100	125	2016	600	no	07F0801, 5 s
07F2001	0	25	100	150	2016	600	no	07F0801, 5 s
07F2002	0	25	100	200	1936	600	no	07F0801, 5 s
07F2501	9	1	56	100	2016	900	no	yes, 60 s
07F2601	22.4	2.5	56	100	2016	900	no	yes, 60 s[5]
07F2602	15	10	56	100	2016	900	no	07F2601
07F2701	10	15	56	100	2016	900	no	07F2601
07F2801	5	25	56	100	2016	900	no	07F2601
07G1301	1.224	23.75	56	100	2016	900	no	07F2601
07G1701	25	0	56	100	2016	60	no	no
08D0801	0	25	56	100	2016	180	no	07F2601, 30 s
08D0801	5	20	56	100	2016	180	no	07F2601, 30 s
08E2901	25	0	56	100	2016	60	no	no
08G0201	25	0	56	100	2016	960	no	no
08G0901	22.5	2.5	56	100	2016	900	no	07F2601
08G1901	17.5	7.5	56	100	2016	1020	no	07F2601
08G2101	12.5	12.5	56	100	2016	900	no	07F2601
09A1402	12.5	12.5	56	100	2016	900	no	07F2601

[1] pulsed-DC unless otherwise specified
[2] 100W RF plasma with Ar at 6.0 Pa for 300 s
[3] 10 sccm of CH_4, 10 Pa and 56 W of pulsed-DC at 100 kHz with positive pulse width of 2016 ns, unless otherwise specified. If sample name is used, see buffer layer for that sample
[4] using 150 W at 150 kHz with 18 sccm of CH_4
[5] with 25 sccm of CH_4

sample	Φ_{CH_4} (sccm)	Φ_{CHF_3} (sccm)	P (W)[1]	ν (kHz)	τ_+ (ns)	t (s)	cleaning[2]	buffer[3]
09A2201	17.5	12.5	56	100	2016	900	no	07F2601
09B1701	25	0	56	100	2016	960	no	no
09B1702	17.5	7.5	56	100	2016	900	no	07F2601
09K1201	25	0	50	100	2016	960	no	no
09K1202	18.75	6.25	50	100	2016	900	no	07F2601
09K1301	12.5	12.5	50	100	2016	900	no	07F2601
09K1302	6.25	18.75	50	100	2016	900	no	07F2601
09K1303	6.25	18.75	50	100	2016	900	no	07F2601
09K1601	0	25	50	100	2016	900	no	07F2601
09L1501	1.1	25	50	100	2016	900	no	07F2601

B.2 Reactively etched samples list

sample	Φ_{SF_6} (sccm)	Φ_{CHF_3} (sccm)	Φ_{O_2} (sccm)	P (W)	p (Pa)	t (s)	mask
06L0501	24	10	8	20	13	180	Al
06L1302 & 03	24	10	8	20	13	542	Al & PMMA
06L1406 & 07	24	10	8	20	13	540	Al & Shipley 1800
06L1601 & 02	16	10	8	20	13	960	Al
06L1702 & 03	8	10	8	20	13	900	Al
06L1802 & 03	20	8.3	10	20	13	900	Al
06L1804 & 05	10	4.2	10	20	13	900	Al
06L2001 & 02	12	10	4	20	13	900	Al
06L2101 & 02	24	10	4	20	13	900	Al
06L2103 & 04	24	10	0	20	13	900	Al

[1] pulsed-DC unless otherwise specified
[2] 100W RF plasma with Ar at 6.0 Pa for 300 s
[3] 10 sccm of CH_4, 10 Pa and 56 W of pulsed-DC at 100 kHz with positive pulse width of 2016 ns, unless otherwise specified. If sample name is used, see buffer layer for that sample

sample	Φ_{SF_6} (sccm)	Φ_{CHF_3} (sccm)	Φ_{O_2} (sccm)	P (W)	p (Pa)	t (s)	mask
06L2201 & 02	5	2	10	20	13	900	Al
06L2203 & 04	5	4.2	10	20	13	900	Al
06L2205 & 06	6.7	2.8	10	20	13	900	Al
06L2701 & 02	5	0	5	20	13	900	Al
06L2902 & 03	10	0	5	20	13	900	Al
07A0201 & 02	5	3.1	5	20	13	900	Al
07A0203 & 04	7.5	4.7	2.5	20	13	900	Al
07A0301 & 02	15	9.4	2.5	20	13	900	Al
07A0502 & 03 & 04	16	10	8	20	13	900	Al
07J2301	0	3.7	0	10	3	300	700 nm of SiO_2
07J2302	0	3.7	0	100	3	600	700 nm of SiO_2
07K0501	10	0	5	20	13	900	100 nm of SiO_2 + PMMA
07K0601	10	2.1	5	20	13	300	100 nm of SiO_2 + marker
07K1501	10	4.2	5	20	13	300	100 nm of SiO_2 + marker
07K1502	10	4.2	10	20	13	300	100 nm of SiO_2 + marker
07K2102	10	2.1	5	20	13	300	100 nm of SiO_2 + PMMA
07K2303	0	3.7	0	100	13	180	100 nm of SiO_2 + PMMA
07K2701	10	2.1	5	20	13	300	100 nm of SiO_2 + marker
08I2501	10	2.1	5	20	13	90	65 nm of SiO_2 + marker & PMMA
08J0701	10	2	5	20	13	90	65 nm of SiO_2 + ZEP520
08J2001	10	2	5	20	13	100	65 nm of SiO_2 + ZEP520
08J2701	10	2	5	20	13	150	65 nm of SiO_2 + ZEP520

B.3 Ion beam etched samples

sample	material	α (°)	P (W)	V_{scr} (V)	V_{acc} (V)	t (s)
06F2201	Si	0	120	550	-55	900
06I2702	Si	0	100	730	-70	3600
06I2801	Si	0	100	640	-60	3600
06I2802	Si	0	100	550	-50	3900
06I2901	Si	0	100	600	-50	3600
06J0901	Si	0	100	600	-60	3600
06J1101	Si	0	100	600	-60	600
06J1002	Si	0	100	640	-60	900
06J1701	Si	0	100	700	-66	900
06J1801	Si	0	100	700	-66	3600
07D1201	Si	0	100	550	-50	3600
07D1601	glass	0	100	550	-50	3600
07D1701	glass+SP	0	100	550	-50	7200
07D2001	glass+SP	0	100	550	-50	900
07D2301	glass+SP	0	100	550	-50	1800
07E1602	glass+SP	0	100	550	-50	2730
07F0601	glass+SP	45	100	550	-50	2700
07F1801	glass+SP	45	100	550	-50	6080
07F1901	glass+SP	45	100	550	-50	2700
07G1801	glass+SP	45	100	550	-50	2700
07G1901	glass+SP	45	100	550	-50	3220
08C0401	glass	45	100	550	-50	4200
08C1101	Si+Au	45	100	550	-50	300
09B1001	Si+SP	45	100	550	-50	300
09B2201	Si+SP	45	100	550	-50	1800
09B2202	Si+SP	45	100	550	-50	900
09B2301	Si+SP	45	100	550	-50	3600

sample	material	α (°)	P (W)	V_{scr} (V)	V_{acc} (V)	t (s)
09B2302	Si+SP	45	100	550	-50	5400
09B2303	Si+SP	0	100	550	-50	900
09B2401	Si+SP	0	100	550	-50	1800
09B2402	Si+SP	0	100	550	-50	3600
09B2403	Si+SP	0	100	550	-50	2700
09B2501	Si+SP	45	100	550	-50	2700

C

Figures and samples

Figure	Samples
5.1	07A1601, 07A1709, 07A1710, 07A1901, 07A2201, 07A3101, 07B0501, 07F2601, 07F2602, 07F2701, 07F2801, 07G1301, 07G1701
5.2	09A1402, 09A2201, 09B1701
5.3	07F2601, 07F2602, 07F2701, 07F2801, 07G1301, 07G1701
5.4	09K1201, 09K1202, 09K1301, 09K1303, 09K1601, 09L1501
5.5	07A1601, 07A1710, 07A2201, 07A2301, 07A3101, 07B0501, 09K1201, 09K1202, 09K1301, 09K1303, 09K1601, 09L1501
5.6	09K1201, 09K1202, 09K1301, 09K1303, 09K1601, 09L1501
5.10	08G0201
5.11	08G0201, 08G0901, 08G1901, 08G2101, 09K1202, 09K1303, 09K1601, 09L1501
5.12	07F2601, 07F2602, 07F2701, 07F2801, 07G1301, 07G1701, 08G0201, 08G0901, 08G1901, 08G2101, 09K1201, 09K1202, 09K1301, 09K1303, 09K1601, 09L1501
5.13	08G0201, 08G0901, 08G1901, 08G2101, 09K1201, 09K1202, 09K1301, 09K1303, 09K1601, 09L1501
5.14	09K1201, 09K1202, 09K1301, 09K1303, 09K1601, 09L1501
5.15	08G0201
5.16	08G0201, 08G0901, 08G1901, 08G2101
5.17	08G0201, 08G0901, 08G1901, 08G2101
5.18	07F2601, 07F2602, 07F2701, 07F2801, 08G2101, 09K1201, 09K1202, 09K1301, 09K1303

Figure	Samples
6.1	06L0501, 06L1302, 06L1406, 06L1407, 06L1601, 06L1602, 06L1702, 06L1703, 06L1802, 06L1803, 06L1804, 06L1805, 06L2001, 06L2002, 06L2101, 06L2102, 06L2103, 06L2104, 06L2201, 06L2202, 06L2203, 06L2204, 06L2205, 06L2206, 06L2701, 06L2702, 06L2902, 06L2903, 07A0201, 07A0202, 07A0203, 07A0204, 07A0301, 07A0302, 07K0501, 07K0601, 07K1501, 07K1502
6.2	06L1602, 06L1703, 06L1803, 06L1805, 06L2002, 06L2102, 06L2104, 06L2202, 06L2204, 06L2206, 06L2702, 06L2903, 07A0202, 07A0204, 07A0302, 07A0502
6.3	06L1802, 07K1501
6.4	06L1602, 06L1703, 06L1803, 06L1805, 06L2002, 06L2102, 06L2104, 06L2202, 06L2204, 06L2206, 06L2702, 06L2903, 07A0202, 07A0204, 07A0302, 07A0502
6.6	06L1407, 06L1803, 06L1805, 06L2102, 06L2104, 06L2202, 06L2206
6.7	08J2701
6.10	06I2702, 06I2801, 06I2802, 06I2901, 06J0901, 07D1601
6.11	07G1901
6.12	09B2201, 09B2202, 09B2301, 09B2302, 09B2303, 09B2401, 09B2403, 09B2501
6.15	09B2303, 09B2401, 09B2402, 09B2403